Cube-textured metal substrates for reel-to-reel processing of coated conductors

Wulff, Anders Christian

Publication date:
2012

Document Version
Publisher's PDF, also known as Version of record

Ph.D. thesis

Cube-textured metal substrates for reel-to-reel processing of coated conductors

Anders Christian Wulff

Department of Energy Conversion and Storage

Technical University of Denmark

September 2012

Abstract

This thesis presents the results of a study aimed at investigating important fabrication aspects of reel-to-reel processing of metal substrates for coated conductors and identifying a new substrate candidate material with improved magnetic properties.
The effect of mechanical polishing on surface roughness and texture in Ni-5at.%W tapes in the cold-rolled condition was studied as a function of polishing grade. The surface roughness of the tape in the polished and annealed condition, and after subsequent coating with a $Gd_2Zr_2O_7$ buffer layer was investigated taking grain boundaries into account. It was observed that the initial mean surface roughness decreased after annealing except after very fine polishing. Additionally, the roughness of the buffer layers were found to increase slightly for the fine polished substrates. Grain boundary grooving was observed to impose a lower limit for the mean surface roughness. Fractions of cube texture within deviations of 5^o from the ideal cube orientation, in the annealed substrates, were found to be very sensitive to the surface roughness before annealing.

Microstructure, texture and topography were studied in a strongly cube-textured Ni-5at.%W substrate before and after an additional annealing (condition A1 and A2, respectively) simulating a buffer layer crystallisation heat treatment. Condition A1 was characterised by a high fraction of cube texture, a high fraction of low angle grain boundaries and a low fraction of $\Sigma 3$ boundaries. A strong correlation was observed between the grain boundary groove depth and boundary type. Coherent twin boundaries and low angle grain boundaries were characterised by the smallest average groove depth while significantly deeper grooves were observed at other boundary types. A similar correlation was observed between the inclination angle at groove walls and the boundary type. The microstructure was slightly coarser in condition A2 and it was accompanied by a cube texture strengthening and an increase in the fraction of low angle grain boundaries. The average depth of grain boundary grooves increased considerably at boundaries characterised by large misorientation angles, except for coherent twin boundaries. Significant changes were observed between the groove depth at stationary boundaries which generally increased in depth and the grooves at migrating boundaries which typically became shallower compared to condition A1. Furthermore, migrating boundaries were found to abandon grooves and generate grooves at new positions. Despite the observed changes in the extent of grain boundary grooving, the mean surface roughness was almost identical before and after the additional annealing.

Microstructure, texture, hardness and magnetic properties have been studied in a series of new Ni-Cu-W substrates. Adding 5 at.% copper to Ni-5at.%W was observed to substantially decrease the Curie temperature and the saturation mass magnetisation without significantly modifying the microstructure and texture compared with Ni-5at.%W. The hardness of this Ni-5Cu-5W substrate was only slightly less than the hardness of the reference Ni-5at.%W substrate. Further increasing the Cu-content was observed to result in a great decrease in the Curie temperature and saturation mass magnetisation values, but also a significant decrease in the fraction of cube texture and the fraction of low angle grain boundaries. Finally, a Ni-5Cu-5W substrate may be a good candidate material as a substrate in future coated conductors.

Resumé

Afhandlingen præsenterer et forskningsarbejde med det formål at undersøge vigtige problemstillinger i forbindelse med fremstilling af metalbånd med en stærk krystallografisk terningtekstur. Disse bånd anvendes til superledende coated conductors og forsøgene er udført med valsede og varmebehandlede (rekrystalliserede) Ni-5at.%W bånd, der er påført et keramisk $Gd_2Zr_2O_7$ bufferlag. Overfladeruhed og krystallografisk tekstur er karakteriseret for prøver i henholdsvis kolddeformeret og rekrystalliseret tilstand og indflydelsen af poleringsbetingelser er kortlagt. En detaljeret undersøgelse af overfladen har omfattet indflydelsen af korngrænse-fordybninger, der opstår under varmebehandlingen. Det blev endvidere konstateret at graden af terningtekstur, indenfor en 5^o afvigelse fra den ideelle krystallografiske terningorientering, var særdeles afhængig af overfladeruheden efter valsning.

Mikrostruktur, krystallografisk tekstur og topografi blev undersøgt, i et Ni-5at.%W bånd med en stærk terningtekstur, før og efter en varmebehandling (henholdsvis tilstand A1 og A2), der simulerede en varmebehandling af et bufferlag. Mikrostrukturen i tilstand A1 var karakteriseret ved et højt antal lavvinkel korngrænser og følgende begrænset andel af korngrænser med højere misorienteringsvinkler, inklusiv $\Sigma 3$ korngrænser. En klar sammenhæng blev observeret mellem dybden af korngrænse-fordybninger og typen af korngrænse. De mindste fordybninger blev observeret ved kohærente tvillingkorngrænser og lavvinkel korngrænser, mens store korngrænse-fordybninger blev registreret ved højvinkel, inkohærente samt ikke-tvilling $\Sigma 3$ korngrænser. En lignende tendens blev observeret mellem den gennemsnitlige inklinationsvinkel ved korngrænse-væggene i fordybningerne og korngrænse-typen. Tilstand A2 var karakteriseret ved en lidt grovere mikrostruktur samt en skarpere terning tekstur og højere andel af lavvinkel korngrænser. Den gennemsnitlige dybde af fordybninger ved højvinkel korngrænser steg markant, undtagen for kohærente tvilling-korngrænser. Store forskelle blev også observeret mellem (i) fordybninger af korngrænser karakteriseret som stationære, der typisk udviklede dybere grøfter, og (ii) fordybninger ved grænser karakteriseret som migrerende var betydelig reduceret. Migrerende korngrænser efterlod fordybninger i overfladen af materialet når de flyttede til en ny position, hvor de dannede nye korngrænse-fordybninger. Der blev ikke observeret nogen signifikant ændring i den gennemsnitlige overfladeruhed på trods af disse lokale topografiske forskelle. Mikrostruktur, krystallografisk tekstur, hårdhed samt magnetiske egenskaber blev studeret i en ny type Ni-Cu-W metalbånd. En legering med 5 at.% Cu i Ni-5at.%W viste en stærkt reduceret Curie temperatur og mætnings-masse-magnetisering, uden nogen væsentlige ændringer i mikrostruktur og tekstur sammenlignet med Ni-5at.%W. Kun en lille reduktion blev observeret i hårdheden som funktion af kobberindholdet. Et forøget kobberindhold (10-15 at.%) resulterede i en fortsat reduktion af Curie temperaturen og af mætnings-masse-magnetiseringen, men også en stærkt forringet terningtekstur, samt en forøget andel af højvinkel korngrænser. Konklusionen på denne undersøgelse er at stærkt teksturerede Ni-5Cu-5W metalbånd er et muligt kandidatmateriale til brug i fremtidige superledende coated conductors.

Preface

This thesis is submitted in partial fulfillment of the requirements for obtaining the Ph.D. degree at the Technical University of Denmark.

The work described in the thesis was conducted at the Materials Research Division, Risø DTU, from 2009-2011, and at the Department of Energy Conversion and Storage, Risø Campus, from 2011-2012.
The Ph.D. project was supervised by Dr. Jean-Claude Grivel, Professor Niels Hessel Andersen and Dr. Oleg V. Mishin.

The thesis describes general effects related to a reel-to-reel fabrication of cube-textured metal substrates for coated conductors. In particular, the effects of mechanical polishing and additional heat treatments on the substrate surface quality are examined. A new alloy with improved magnetic properties with respect to alternating current losses in coated conductors is also analysed.

This Ph.D. project was financially supported by the Danish Ministry of Science, Innovation and Higher Education under contract number 09-065234.

ISBN: 978-87-92986-02-3

Roskilde, September 2012
Anders Christian Wulff

Publications during the project

Main authored papers

A.C. Wulff, Y. Zhao, O.V. Mishin , J.-C. Grivel,
"Effect of Initial Surface Quality on Final Roughness and Texture of Annealed Ni-5at.%W Tapes Coated with a $Gd_2Zr_2O_7$ Buffer Layer",
J. Supercond. Nov. Magn. 25 (2012) 475-9.

A.C. Wulff, O.V. Mishin, J.-C. Grivel,
"Topographic changes in Ni-5at.%W substrate after annealing under conditions of buffer layer crystallization",
Phys. Proc. 36 (2012) 1423-8.

A.C. Wulff, O.V. Mishin, J.-C. Grivel,
"Evolution of microstructure, texture and topography during additional annealing of cube-textured Ni-5at.%W substrate for coated conductors",
J. Alloy. Comp. 539 (2012) 161-7.

A.C. Wulff, O.V. Mishin, N.H. Andersen, Y. Zhao, J.-C. Grivel,
"Microstructure, texture and magnetic properties of Ni-Cu-W substrates for coated conductors"
Mater. Lett. 92 (2013) 386-388.

Co-authored papers

J.-C. Grivel, A. C. Wulff, Y. Zhao, N. H. Andersen, J. Bednarcik, M. v. Zimmermann,
Supercond. Sci. Technol. 24 (2011) 015007 (4pp).

J.-C. Grivel, A. C. Wulff, Y. Zhao, J. Bednarcik, M. v. Zimmermann,
J. Mater. Sci. 46 (2011) 4540-4.

J.-C. Grivel, Y. Zhao, A. C. Wulff, P.G.A.P. Pallewatta, J. Bednarcik, M. v. Zimmermann,
Phys. Proc. 36 (2012) 600-5.

Patent applications during the project

The author filed three patent applications internally at DTU over the period of 2010-2012.

One patent application regarding minimized AC losses in coated conductors has been registered at the European Patent Office in 2012.

Acknowledgements

I would like to express my gratitude to everyone who has helped during my work at DTU over the last three years.

I would like to dedicate a special acknowledgement to my three supervisors,
Dr. Jean-Claude Grivel, Professor Niels Hessel Andersen and Dr. Oleg V. Mishin.
Thank you for supporting me with your vast scientific knowledge, encouragement, trust and patience.

Dr. Jean-Claude is sincerely acknowledged for all his help and patience during my studies including general discussions on the project, publications, patenting and making this project possible.

I am very grateful for the introduction to magnetic measurements by Professor Niels Hessel Andersen and for the many enlightening discussions on superconductivity and magnetism, and for great help during the preparation of publications.

Dr. Oleg V. Mishin is greatly acknowledged for introducing me to the EBSD technique, for helping me with texture and microstructure analysis and for exceptional help during the preparation of publications.

It is a great pleasure and I am very honored by having Dr. Dorte Juul Jensen,
Professor Bernhard Holzapfel and Professor Bartlomiej Glowacki as referees of the thesis and for helping me improve the thesis.

Professor Petriina Paturi deserves a special thanks for helping me with XRD measurements and discussions concerning superconductivity. I would also like to sincerely acknowledge
Dr. Katerina Rubesova for help with XRF measurements.

Dr. Yue Zhao, and Dr. Xiao-Fen Li are gratefully acknowledged for their great support, discussions and experimental assistance during my project.

Dr. Jørn Bindslev Hansen, Dr. Wolfgang Pantleon and Dr. Asger Abrahamsen have been a great inspiration to me and I am very grateful for all the discussions on superconductivity, material science and patenting, we have had.

Dr. Niels Hansen is sincerely acknowledged for contributions to the Danish resumé.

A sincere acknowledgement goes to Professor Hongli Suo and Dr. Mang Mang Gao for introducing and assisting me in fabrication of long metal bars for production of long strongly textured metal substrates during my stay at the Beijing University of Technology in China.

Mr. Ole Trinhammer is sincerely acknowledged for assistance during AFM measurements and very helpful discussions on topics relevant to the technique.

I would like to thank former and present members of the coated conductor group at DTU, Dr. Dimitrios Pavloupolos, Dr. He Dong, Ms. Hui Tian, Mr. Xiao Tang and Mr. Assanka Pallewatta for great discussions and being an inspiration to me during my studies.

I have furthermore to thank for instruction, guidance and assistance by the talented technicians at DTU.

A special thanks goes to Mr. Lars Lorentzen for help and guiding during cold rolling, annealing and hardness measurements.

Mr. Mike Wichmann, Mr. Finn B. Saxild, Mr. Ove Rasmussen and Mr. Mikkel Nørrevang are greatly acknowledged for assistance during arc-melting, hot forging and help with experimental designs.

I am also very grateful for the help and guiding from Mr. Johannes Steen Bang, Ms. Gitte Christiansen and Mr. Preben Olesen with preparation of samples.

This project would not have been possible without the great help and support from my family and friends during the last three years.
In particular, I would like to express my gratitude to Michael, Lasse, Linne, Linda, Henrik, Katja, Ronald and Finn for all your support and inspiration.

My mother and father, my sister Nanna and my grandfather deserve a special thanks for all their support, endeavours, patience, love and care during the last three years.

This work is dedicated to Sarah and our daughter, Lilli, who are a constant source of energy, encouragement and love to me.

Roskilde, September 2012
Anders Christian Wulff

Contents

Chapter 1

Introduction

1.1 The global energy production perspective

The global energy demand is expected to nearly double by 2050 compared with the present level of about 15 TW [1]. Meanwhile global climate changes render a great need for reductions in emission of green house gases, such as CO_2, caused by heavy utilisation of fossil energy sources for energy production [1,2]. It is apparent that an increasing global energy demand and a reduction of CO_2 emissions require up-scaling of present sustainable solutions and development of new sustainable energy production technologies as suggested by the Intergovernmental Panel on Climate Change (IPCC) [1].

Wind turbines are considered a mature sustainable energy production solution and the global capacity of wind farms was 160 GW by the end of 2009 while the total investments in wind energy amounted to 57 billion USD. IPCC estimate that the global contribution to energy production from wind power is only 1.8 % and that this could be increased to 20 % by 2050 if ambitious efforts are made [1].

A very ambitious Danish long term governmental strategy against climate changes includes an energy system independent of fossil energy sources and a 80-95 % reduction in CO_2 emissions in Denmark by 2050 [3] which may be achieved by increasing the fraction of electric power produced by sustainable power sources such as wind, sun and wave power. The Danish Commission on Climate Changes Policy (DCCCP) proposes [3] that the national wind power capability should amount to at least 10 GW by 2050 which is more than double the current installed capacity (3951 MW) in 2011 [4]. As suggested by both IPCC and DCCCP advances in the size and number of particularly off-shore wind turbines are needed to meet this demand for an increased sustainable energy production.

Wind turbines and superconductor technology

The size of presently installed off-shore wind turbines ranges from 2 to 5 MW. A high fraction of the installed capacity suffers from problematic gearboxes [5] and a design that makes future up-scaling of new wind turbines difficult. The latter is mainly due to the size and weight of copper-based generators when increasing capacity and torque [1,6].

High technology solutions based on superconductors, such as high performance cables and generators, constitute major research areas and are being investigated and developed world wide [7]. For example, 10-20 MW off-shore wind turbines based on direct drives with generators utilising superconductor wires enable a design with no problematic gearbox system and up-scaling with less size and weight difficulties compared with present copper-based generator technology.

Practical superconductor systems, such as generators with coils wound using superconductor wire, include a cooling system where a coolant is circulated in a closed system. Liquid nitrogen

can be used as a coolant for a so-called coated conductor (CC), i.e. the second generation of high temperature superconducting wires, and enables a high critical current density in high magnetic fields. This coolant is considered cost effective compared with standard coolants, e.g. helium used typically for low temperature superconductors [8]. Current prices for commercial available CCs is about 50 USD/kAm [9] which is still too high compared with competing technologies, e.g. permanent magnet systems [6]. The latter technology is however utilising large amounts of rare-earth materials and therefore not considered a long term cost effective alternative due to material costs. Intense research and resulting optimisation of cost/performance for CCs have significantly reduced the price/kAm in recent years [7,9]. Abrahamsen et al. [6] estimated that the price of CCs should be further reduced by one order of magnitude to be a cost competitive alternative to existing technologies in order to obtain a market penetration with superconductor-based wind turbines. One of the major production costs of commercial available CCs are the physical vapor deposition techniques applied for preparation of buffer layers and/or superconducting layers. Production of CCs using more cost efficient techniques, such as chemical solution deposition, are therefore currently being investigated with the aim of lowering the production costs and thus the price/kAm of CCs [9].

1.2 Subject and aims of this thesis

This Ph.D. project is part of a larger research project aiming at developing a new, scalable reel-to-reel production technology in view of continuous manufacturing of superconducting wires with competitive production costs and improved performance based on chemical dip coating. The key point of this technology is a simultaneous coating process of first buffer layers and then superconducting layers on both sides of textured metal substrates.

Strongly textured metal substrates thus form the basis for CCs in this larger research project. The aims of the present thesis are to identify and investigate important aspects of the textured substrate in view of a reel-to-reel fabrication and to develop new a substrate with optimised magnetic properties for CCs used in alternating current applications.

1.3 Structure of the thesis

The thesis is divided into three parts.

Part I - Background, is a review of the different topics relevant to the experimental work presented in the thesis. Chapter 2 includes a brief introduction to historical milestones and relevant concepts of superconductivity. Coated conductors and strongly textured metal substrates are discussed in chapter 3 which also includes aspects relevant to the substrate during CC production. An introduction to ferromagnetism and alternating current losses in CCs are included in chapter 4. The chapter is concluded with the research hypothesis' of the thesis.

Part II - Materials and Experimental techniques, is an introduction to the materials and experimental techniques applied in the thesis. Chapter 5 covers preparation of ingots, cold rolling and annealing treatments. Experimental techniques used for characterisation of the prepared samples are presented in chapter 6.

Part III - Results, Discussion and Conclusions includes the different results obtained in the present work and a discussion of the findings. Chapter 7 is a presentation of the different results and discussions of the findings in relation to work conducted by other groups. Finally, conclusions and an outlook are given in Chapter 8.

Part I

Background

Chapter 2

Superconductivity

This chapter gives a brief introduction to superconductivity and superconductor materials relevant to the topics of this thesis. More comprehensive surveys can be found in textbooks e.g. by Fossheim and Sudbø [10] and Goyal [11].

2.1 Review of superconductor milestones and theory

Onnes [12] discovered in 1911, that the electrical resistivity of mercury dropped abruptly to zero below a critical temperature (T_C) when cooling with liquefied helium (4.2 K). Accordingly, no energy dissipated as heat for an electrical current in the material which contradicted the existing theory for resistivity of pure metals predicting a steady decrease to a finite resistivity at 0 K. This new phenomenon was termed *Superconductivity*. It depends on three restricting parameters; T_C, the critical magnetic field (H_C) and the critical current density (J_C), all three interrelated as shown schematically in Fig. 2.1. Note that J_C is defined as the maximum current per cross-sectional area of a superconducting wire in the zero resistivity state.

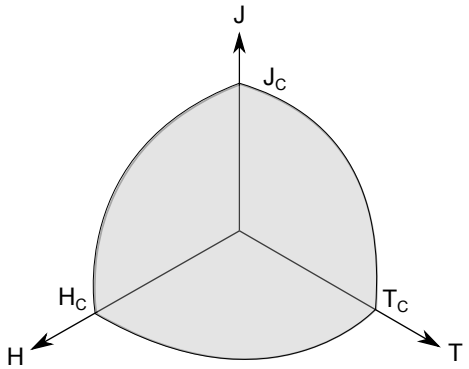

Figure 2.1: Schematic relationship between the three critical parameters, T_C, J_C and H_C. The superconducting state is obtained below the grey surface.

Superconductivity is, according to the famous BCS[1] theory [13], caused by pairing of a fraction of the conduction electrons (n_s) into a bound state (Cooper pairs) mediated by crystal lattice vibrations resulting in a phase, where the pairs experience no effective scattering, (conserved total momentum) resulting in zero electrical resistivity for these electrons.

A superconducting phase has been observed for numerous metals and alloys (for example Pb, Nb, Nb_3Sn, V_3Si and $CeCu_2Si_2$), but generally at very low transition temperatures. Such materials are therefore classified as *Low Temperature Superconductors* (LTS).

[1] Formulated by Bardeen, Cooper and Schrieffer in 1957.

Most industrial production of superconducting wire for magnets used in e.g. magnetic resonance imaging for medical purposes and high energy physics research, is made using LTS materials such as Nb_3Sn and NbTi [10,14]. One of the reasons for the success of these particular materials is their high critical current density in high magnetic field. This means that by cooling with helium and using a relatively small amount of material very strong electromagnets can be constructed compared with magnets made using copper coils and iron cores [15]. The very expensive helium limits the usage of LTS materials. These materials are therefore mainly applied in research and for medical use [8,9].

Another 75 years had passed, after Onnes' discovery, before synthesis of the ceramic La-Ba-Cu-O system with a transition temperature of 35 K was reported by Bednorz and Müller in 1986 [16]. It was a substantially higher T_C compared with the former record of 23 K for the metallic Nb_3Ge and this system was therefore termed *High Temperature Superconductor* (HTS). The year after, in 1987, Chu et al. [17] synthesised the cuprate $YBa_2Cu_3O_{7-\delta}$ (YBCO), an anisotropic ceramic superconductor with an impressive $T_C = 93$ K for $\delta \sim 0.07$.

The ideal atomic crystal structure of crystalline materials is characterised by a finite number of unit cells repeated over the entire material volume. Accordingly, the unit cell is a representation of the crystal structure and there are several different crystal structures. An example of the body-centered-cubic crystal structure of the more symmetric Nb-47wt.%Ti and the orthorhombic structure of anisotropic YBCO are shown Fig. 2.2.

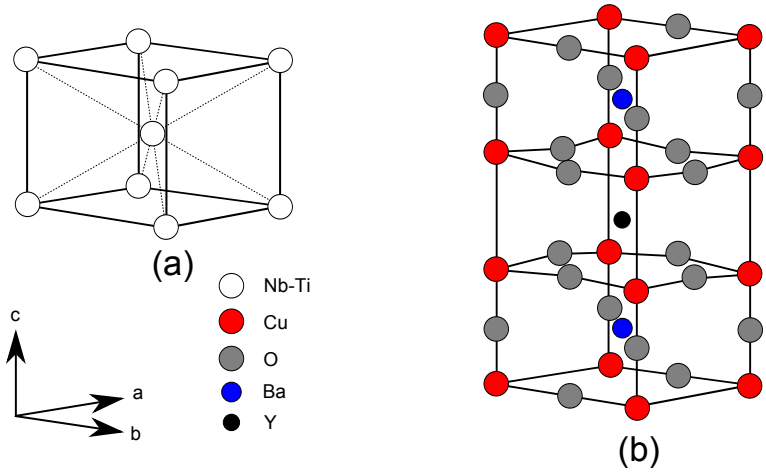

Figure 2.2: Example of a body-centered-cubic (a) and an orthorhombic (b) crystal structure for Nb-47wt.%Ti and YBCO, respectively.

It is important to note that the crystal structure of undoped $YBa_2Cu_3O_6$ is tetragonal and that a subsequent oxygenation at $\sim 450\ ^oC$ increases the oxygen content, to a δ-value below 0.65, resulting in YBCO's superconducting orthorhombic structure.

T_C for some HTSs is above the boiling point (77 K) of cost effective liquid nitrogen which could then be used for cooling the superconductor. Additionally, a very high J_C (> 1 MA/cm^2) in magnetic fields of 1 T were obtained for YBCO compared with other HTS materials [10]. The superconducting properties could therefore be retained even at liquid nitrogen temperatures rendering it very useful for various power applications. This was a major breakthrough for applied superconductivity. The highest T_C ever observed is for $HgBa_2Ca_2Cu_3O_{8+\delta}$ with impressive 134 K at ambient pressure and 164 K at ~ 30 GPa [18]. This material is however difficult to synthesise, toxic and thus unsuitable for most technical applications. $Bi_2Sr_2Ca_2Cu_3O_{10+x}$ (Bi-2223) with $T_C = 110$ K was the first HTS material to reach a commercial stage. Wires made using this material are classified as the first generation (1G) HTS wires. Some of the major differences between these ceramic HTS materials are the atomic structures (e.g. CuO_2 planes and CuO

donor chains/planes) coherence lengths, penetration depths, resulting level of anisotropy and the effect on T_C, J_C and H_C. These aspects will be reviewed and discussed in relation to HTS wires fabricated utilising HTS materials in the following.

Superconducting properties and anisotropy

Two characteristic length scales

By extending Maxwell's equations F. and H. London [10] established in 1935 two very basic relations for a superconductor. The first London equation describes the frictionless acceleration of superconducting electrons due to an electric field near the superconductor surface. The second London equation specifies how a superconductor will screen an external magnetic field within the London penetration depth, λ, from the surface due to the superconducting surface currents. This phenomenon is known as *the Meissner effect*. Estimates of $\lambda \sim 50$ nm for various metals are in good agreement with experiments [10].

Another important length scale, the coherence length, ξ, over which the superconducting order parameter changes was derived in the very successful Ginzburg-Landau theory formulated in 1950 [10]. An alternative definition of the coherence length originates from the BCS theory [13] where ξ_0 is the characteristic size of the Cooper pairs. It should be stressed that the two coherence lengths are interrelated but qualitatively different since ξ is temperature dependent.

Mixed state and vortices

An appropriate magnetic field applied to a superconductor causes a rotational flow of the superconducting electrons either at the surface (Meissner effect) or as an additional flow inside the material screening a quantised magnetic flux, known as the *the mixed state*. In the latter state, it may become energetically favourable (depending on λ and ξ) to include and trap quantised magnetic flux inside the superconductor [19].

Abrikosov [20] proposed in 1957 the existence of two types of superconductors depending on the Ginzburg-Landau parameter $\kappa = \lambda/\xi$.

The ratio between the penetration depth and the coherence length relates to the ability (depends on the surface energy) to form an interface between a normal and a superconducting region in the presence of an appropriate magnetic field. As a consequence, superconductors are divided into two types:

$$\begin{aligned} \text{Type I with} \quad & \kappa < 1/\sqrt{2} \\ \text{Type II with} \quad & \kappa > 1/\sqrt{2}. \end{aligned}$$

For example, $\kappa = 0.03$ and 0.47 for aluminum and lead (type I), respectively, while $\kappa = 34$ and 87 for Nb_3Sn and YBCO (type II), respectively [10]. Type I materials exhibit only the Meissner state and superconductivity is completely suppressed at fields $H \geq H_{C1}$ and the material becomes normal conducting. H_{C1} (both type I and II) is usually in the low mT range and type I materials are therefore unsuitable for power applications [9,10].

The situation is very different for a type II material where the magnetic flux can partially penetrate the interior of the superconductor and thus retains the superconducting state. A schematic of the critical fields as function of temperature for both type I and II superconductors are shown in Fig. 2.3(a).

The magnetic field penetrates in confined flux regions, or vortices, that may form different structures, as for instance a hexagonal flux pattern, see inset in Fig. 2.3(a). Vortices are quantised in units of $\Phi_0 = h/2e$, where h is Plank's constant and e is the electron charge. The so-called Abrikosov vortex (AV) is schematically shown in Fig. 2.3(b). It consists of a normal state core, with a size $\sim 2\xi$ and the applied magnetic field decaying over the distance λ into the

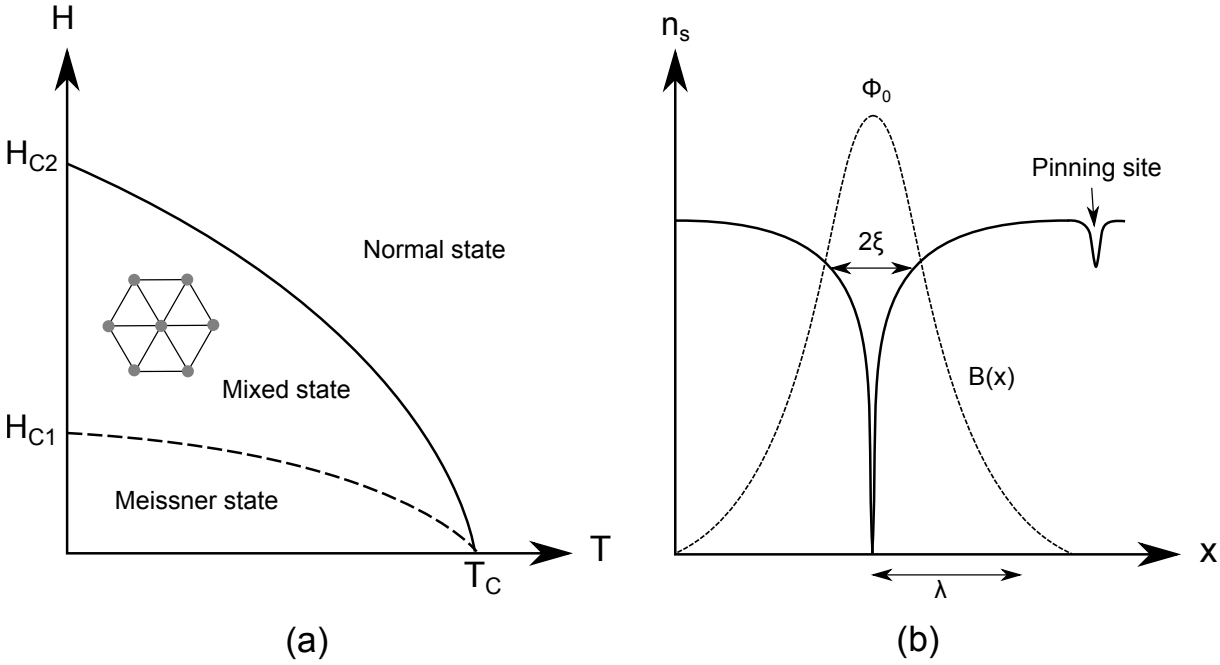

Figure 2.3: Schematic drawings of (a) the critical fields (H_{C1} and H_{C2}) as function of temperature and resulting states, and (b) superconducting pair density (n_S) as function of position (x) representing an Abrikosov vortex. The inset in (a) represents a possible flux pattern. Reproduced after [19].

superconductor. By including the magnetic flux in the form of AVs superconductivity may be retained until the normal cores completely overlap at H_{C2} and the material becomes normal conducting, see Fig. 2.3 (a).

Anisotropy and the magnetic irreversibility field

HTS cuprates are characterised by a strong anisotropy, originating mainly from the complex layered structure of the weakly coupled superconducting CuO_2 planes [21], see Fig.2.2, and a d-wave ($d_{x^2-y^2}$) symmetry of the Cooper pairs [22]. As a result, ξ is different along various directions of the unit cell, e.g. for YBCO, $\xi^{\perp} = 0.5$ nm and $\xi^{\parallel} = 2.5$ nm [15]. Significant differences are therefore observed between $H_{C2}^{\parallel}$ and $H_{C2}^{\perp}$, i.e. parallel and perpendicular to the CuO_2 planes in the cuprates, with a ratio $\sim$ 5-7 and 50-200 for YBCO and Bi-2223 at 4.2 K, respectively [15]. Note that $H_{C2}^{\parallel}$ is exceeding 100 T at 4.2 K for both YBCO and Bi-2223. This implies that in order to obtain the highest field performance, all unit cells must be parallel and well connected, i.e. conduction through parallel CuO_2 planes [15]. Above 77 K both YBCO and Bi-2223 have H_{C2} values similar to those of Nb-Ti and Nb_3Sn below 20 K.

Practically, utilising the material in power applications means that a transport current, I_T, will be applied. This current will generate a magnetic field which is typically perpendicular to the current direction. This will affect the vortex lattice as the transport current interacts with the vortices and the resulting Lorentz force ($F_L = J_T \times \Phi_0$, where J_T is the transport current density) moves the vortices, see Fig. 2.4.

A pinning site is a confined region in the material where superconductivity is slightly or completely suppressed, see Fig. 2.3(b). Producing an AV at this site is favourable and the AV is *pinned* at this position. J_C is defined as the point where vortices start moving. This results in energy dissipation and eventually vortices leave the material at one edge of the wire while new AVs enter at the opposite edge. Vortex pinning is therefore extremely important in practical HTS materials to obtain the highest possible critical current. The force needed to

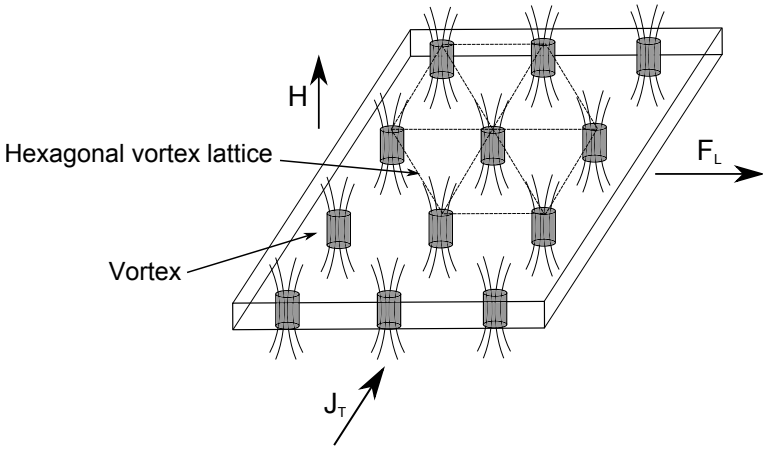

Figure 2.4: Schematic drawing of a hexagonal vortex lattice in an equilibrium state before changes due to the Lorentz force (F_L). Reproduced after [19].

counterbalance the Lorentz force is named *the pinning force*, (F_P), and it depends on the origin and size of the pinning site which can be e.g. grain boundaries, stacking faults, dislocations, voids, atomic inclusions, secondary phases and preferably with an optimum size $\sim\xi$. The Lorentz force becomes greater than the pinning force at sufficiently high applied fields (or transport currents) and AVs start moving [10].

The practical upper limit of magnetic field, at which the zero resistivity state is lost, may be substantially below the ideal upper value of H_{C2}. This new limit is termed *the irreversibility field*, $H_{C1} < H_{irr} < H_{C2}$ and it imposes a practical limit for the critical current density, J_C. Great differences, largely due to anisotropy, are observed between H_{C2} and H_{irr} for the cuprates as shown in Fig. 2.5.

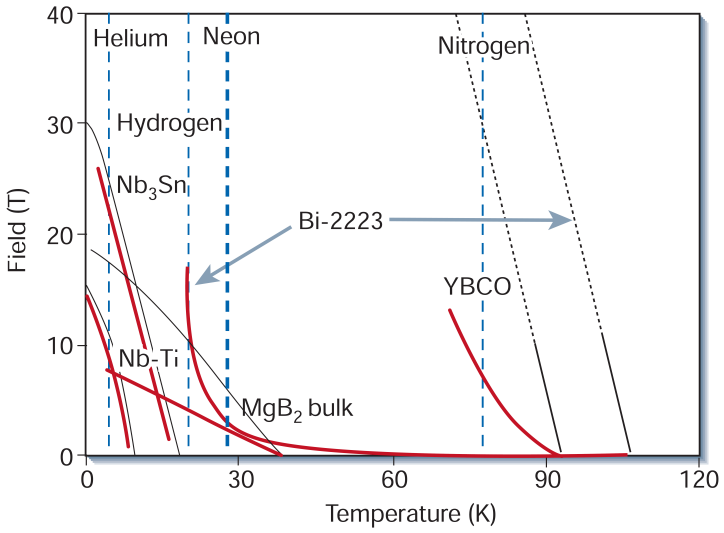

Figure 2.5: Irreversibility fields (red lines) and upper critical fields, H_{C2} (black lines) as a function of temperature for Nb-47wt.%Ti, Nb_3Sn, MgB_2, Bi-2223 and YBCO. Boiling points of helium, hydrogen, neon and nitrogen are presented as vertical blue lines [15].

It is evident from Fig.2.5 that H_{irr} is strongly suppressed for Bi-2223 ($\sim$0.2 T), compared with YBCO ($\sim$7 T). This is mainly due to a weaker coupling between the CuO_2 layers and a three times longer unit cell, compared with YBCO, resulting in a stronger anisotropy. The

Bi2223 vortex system is therefore more 2D pancake-like, in contrast to the more 3D-like YBCO vortex system [10]. The low H_{irr} limits the usage of Bi-2223 to power cables [10], while YBCO is also suitable for high field power applications. In contrast, H_{C2} and H_{irr} nearly coincide (see Fig.2.5) in LTS type II materials such as Nb_3Sn and Nb-Ti due to a negligible anisotropy and a lower operational temperature [15,23].

It is clear that a higher operational temperature will result in enhanced thermal fluctuations leading to dissipation effects, such as thermally assisted flux flow (TAFF), flux creep or even high current flux flow, which are well described by the Kim-Anderson model [24]. Note that the threshold, at which TAFF may occur, depends on the thermal energy (k_BT), the pinning force and extent of collective pinning. Interestingly, even for a low transport current, where $F_L<F_P$, vortices may be thermally activated and jump from one pining site to another pinning site leading to a finite electrical resistivity. To compensate for these effects, lowering the operational temperature is one simple way to significantly improve the flux pinning ability (see Fig.2.5) of the superconductor [10]. Another very successful alternative is the introduction of additional stronger pinning sites which may significantly increase H_{irr}, e.g. doping YBCO with $BaZrO_3$ nanoparticles [25].

Chapter 3

Introduction to coated conductors

A brief description of the first generation HTS wires and the challenges encountered in fabricating wires using HTS cuprates leading to the development of coated conductors (CCs) are discussed in this chapter. Particularly, overcoming the problem of weak-links and large scale wire manufacturing are addressed in relation to the performance of superconducting thin films. The rolling assisted bi-axially textured substrate (RABiTS) technique is discussed and relevant processing aspects are also included. Finally, the chapter is concluded with a discussion of ceramic layer deposition and related metal substrate effects.

3.1 High temperature superconducting wires

The first generation of HTS wires was based on silver tubes filled with metal-oxide powders. This is known as the powder-in-tube (PIT) method [10]. For example, Bi-2212 powders and other reactants are loaded into chemically inactive silver tubes which then act as mechanical support. The filled tubes are then extruded, drawn/rolled and heat treated at elevated temperatures in an atmosphere to form superconducting textured polycrystalline Bi-2223 tapes. J_C is limited to about $5{\cdot}10^4$ A/cm^2 for Bi-2223 tapes at 77 K and in self-field, i.e. with no external magnetic field applied. This implies that these wires are suitable for power cables but not for high magnetic field applications. It is apparent that the silver consumption in combination with a strong magnetic field dependency of J_C limits the potential of Bi-2223 PIT wires.

3.1.1 Grain boundary weak-links

Several attempts have been made to produce PIT wires based on YBCO [26] but J_C has been limited to values $\sim$ 3300 A/cm^2. The poor performance of YBCO-based PIT wires resides in the weak-link behaviour at grain boundaries (GBs) between the YBCO grains [27].

In general, GBs in YBCO may be viewed as superconducting regions separated by a strained lattice due to dislocation cores and their associated strain fields [28]. Additionally, this superconductor is also characterised by a d-wave symmetry of the Cooper pairs and a very short coherence length ($\sim$1nm). The combination of the pair symmetry, coherence length and strain fields result in a significant decoupling between the CuO_2 planes depending on the boundary misorientation. A discussion of texture and GB misorientation is included in appendix 10.

YBCO thin films grown epitaxially on bicrystalline substrates [29] enable a direct analysis of J_C across a boundary as a function of misorientation angle. Such thin films are for example made using pulsed laser deposition (PLD). Their typical thickness is 200-300 nm and they may be grown on single crystalline substrates, such as $SrTiO_3$. It is important to note that the thin film inherits both morphology and texture from the substrate during growth [28]. This fact will be discussed in more detail in the last part of the chapter.

Data obtained by Held et al.[30] for bicrystalline YBCO thin films clearly demonstrate the misorientation effect on J_C for various types of GBs, see Fig.3.1(a). The different types of GBs are presented in Fig. 3.1(b).

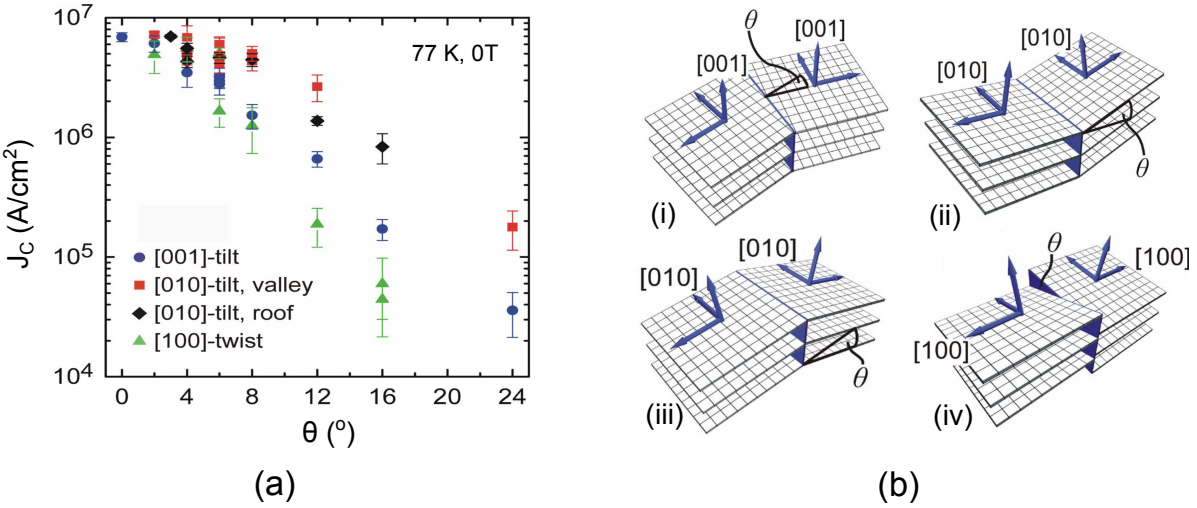

Figure 3.1: (a) Critical current density (J_C) as a function of misorientation angle (θ) across grain boundaries in YBCO bicrystals, and (b) various types of grain boundaries (i) [001] twist, (ii) [010] tilt (valley), (iii) [010] tilt (roof) and (iv) [100] twist [30].

Interestingly, the greatest decrease in J_C as function of misorientation angle θ, at 77 K and zero applied magnetic field, is observed for [100]-twist GBs. J_C is reduced by one order of magnitude at $\theta \sim 10^o$ for this particular type of boundary. In contrast, J_C of the [010]-valley boundaries is less sensitive to an increase in θ and thus only reduced by a factor of 2 to 3 at $\theta \sim 10^o$, see Fig. 3.1(a). Furthermore, this effect has been shown to be relatively independent of the preparation method of the films and thus reflects a more general misorientation dependency of J_C [10,27]. Dimos et al.[29] described the relation between misorientation angle and J_C across a GB as an exponential function:

$$J_C \sim J_C \cdot e^{-\theta/\theta_0}$$

where θ_0 is the misorientation angle above which J_C is significantly reduced. Multiple values of θ_0 have been reported by various authors. Following the work by Heinig et al.[31], $\theta_0 = 10^o$ is chosen in this thesis as the threshold misorientation angle between a strong and a weak coupling at a GB.

It is evident that a HAGB with a very large θ strongly suppresses J_C. Accordingly, such boundary may be characterised as a Josephson junction due to the decoupling. Such junctions only allow for quantum tunnelling currents as shown in Fig. 3.2 [10].

Importantly, a strong texture, both in-plane and out-of-plane (bi-axial texture) is needed in order to produce small misorientations between adjacent grains and a correspondingly low fraction of HAGBs [11]. YBCO films grown on single crystalline substrates such as $SrTiO_3$ typically enables extremely high J_C values $\sim 10^6$ A/cm^2 even at 75 K [32].

Finally, yttrium may be (partially) substituted by rare-earth (RE) elements, such as Gd, Nd, Sm and Eu, while still obtaining similar high J_C values [27, 33]. The superconducting thin films will consequently be referred to as RE-BCO.

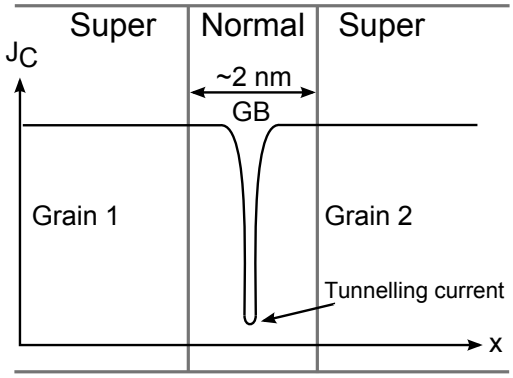

Figure 3.2: Schematic presentation of a Josephson junction-like grain boundary and following quantum tunnelling current.

3.2 Coated conductors - structure and fabrication techniques

It has been established that a RE-BCO polycrystalline film must have a strong bi-axial texture to achieve its full current carrying capacity. However, single crystalline ceramic substrates as the only substrates are obviously not suitable for production of km long CCs. The main requirements for a practical substrate comprise (1) a strong bi-axial texture, (2) a lattice parameter similar to the RE-BCO, (3) a smooth surface and (4) mechanical strength and flexibility.

Ni-based polycrystalline metal substrates with superior handling characteristics were early established as basis for coated conductors since flat metal tapes (thickness < 100 μm) with a sufficiently low surface roughness (S_A<10 nm) could be obtained [9,11]. However, J_C values of YBCO films were significantly lower than what could be obtained on single-crystalline substrates. Metal ions diffusing into the superconducting layer, HAGBs, and surface roughness were identified as major obstacles for this new type of conductor structure. Intensive research over the last two decades [9] has been made on optimising architectures based on metal tape substrates coated with metal-oxide buffer layers, RE-BCO layer(s) and finally metal cap layers. An example of such a layered architecture is shown see Fig. 3.3. This structure is known as a coated conductor - the second generation HTS wire.

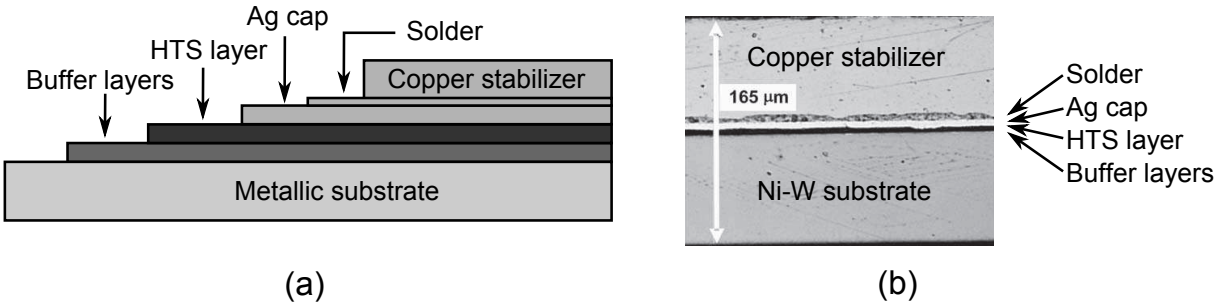

Figure 3.3: (a) Schematic drawing of a CC structure and (b) optical micrograph of a CC cross-section [34].

The buffer layers are multi-functional. They act as a diffusion barrier, decrease lattice misfit and transfer the texture. Silver is typically deposited on top of the RE-BCO layer and provides a chemical protection and a thermal quench protection. The final cap layer can be copper which increases the electrical and mechanical stability that also enables soldering of joints between CC tapes. Additional casing with stainless steel may be used to further increase the mechanical strength and to improve of the handling properties [9,11]. A typical width of CCs is 4 mm and the tape thickness is ∼100-200 μm, including the copper layer. Several different fabrication

techniques and complex metal-oxide layered stack systems have been developed and employed in order to obtain optimum conductor solutions with respect to current carrying capacity, quench protection, performance after coil winding etc. for both cable and power applications. There is therefore a great diversity of different CC structures depending on the final application. Obviously, increasing the thickness of the substrate or the stabilisers will decrease the engineering current density (J_E). In contrast, increasing J_C or the total cross-section area of superconducting layer(s) will beneficially increase the critical current, I_C. Such an increase in cross-section area of RE-BCO can be accomplished by double-side coating of both buffer layers and RE-BCO layers. However, this requires a substrate which enables the formation of strongly textured buffer and superconducting layers on both sides of the substrate metal tape.

Strongly textured substrates

Three of the main techniques for producing a textured template for coated conductors are *ion beam assisted deposition* (IBAD), *inclined substrate deposition* (ISD) and *rolling assisted bi-axially textured substrate* (RABiTS) [11]. Two examples of possible architectures of a CC stack using the IBAD and the RABiTS technique for producing a strong texture are shown in Fig. 3.4 (a) and (b), respectively.

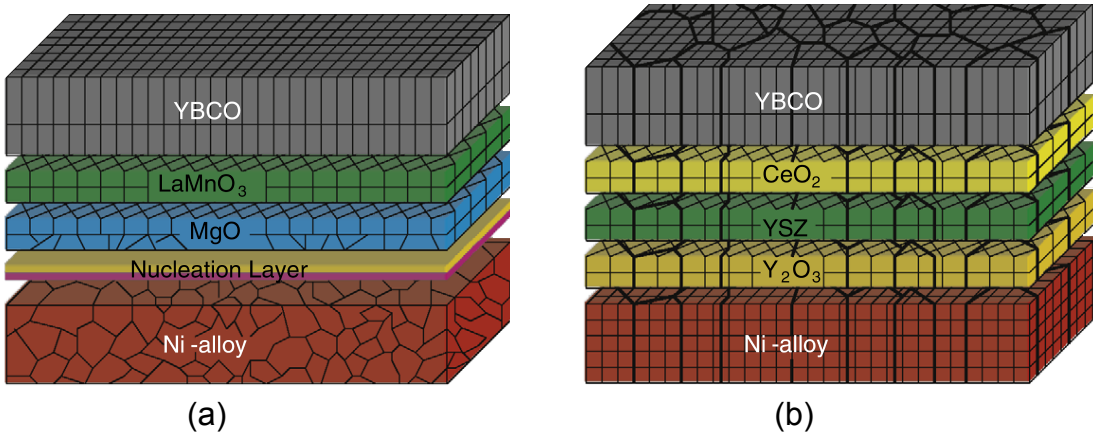

Figure 3.4: Coated conductor structures (a) using the IBAD technique, and (b) using the RABiTS technique [28].

From the bottom; the IBAD-structure consist of a non-textured polycrystalline metal tape, a nucleation layer(s), a bi-axially textured MgO buffer layer, a $LaMnO_3$ buffer layer and finally a superconducting YBCO layer. It is indicated that the grains in the "Ni-alloy" are randomly orientated in contrast to the well aligned grains/unit cells in the three upper layers. The metal tape material could also be stainless steel or Hastelloy [11].

An example RABiTS structure is presented in Fig.3.4(b). It consists of a strongly textured Ni-alloy substrate followed by a Y_2O_3 buffer layer, an yttrium stabilised zirconium (YSZ) buffer layer, a CeO_2 buffer layer and finally a YBCO layer. The square lattice in the metal substrate represents the strong texture. Note that GBs (thick black lines) are transferred through the entire CC stack.

There are two general limiting factors associated with the IBAD and ISD techniques. The first factor is the use of complex and expensive vacuum chambers. For example, buffer layers produced by PVD techniques accounts for more than 20 % of the total coated conductor cost [35]. The second factor is the limitation to single-side coating. Accordingly, these techniques are considered less relevant in respect to reducing production costs while simultaneously improving the performance of CCs, i.e. increasing I_C. A description of the IBAD and ISD techniques is

therefore included in appendix B.

Double-side coating may be performed using chemical solution deposition (CSD) techniques such as dip-coating. CSD is a cost effective wet-chemical approach with a greater potential for scale-up due to simplicity and ex-situ epitaxial growth [36]. The process involves coating of textured metal substrates with a metal-organic precursor solution at room temperature which is then followed by a high-temperature annealing in order to obtain strongly crystalline phases. Note that multiple homogeneous films can be produced by precisely controlling the composition and stoichiometry [37]. Both the buffer layers and the RE-BCO layers should be coated on both sides of a strongly textured metal substrate.

3.3 Rolling assisted bi-axially textured substrates

Strongly cube-textured Ni-5at.%W substrates are commonly applied for the preparation of CCs [11]. This material is used for the following reasons: It can be strongly cube textured, annealed in a protective atmosphere without oxidizing, the yield strength is sufficient at elevated temperatures to be pulled through high temperature furnaces and the lattice misfit with YBCO is suitable.

Thermo-mechanical processing (TMP) techniques, e.g. rolling and annealing, are well established methods for altering shape, characteristics and properties of metal and alloys. RABiTS consist of a strongly textured metal substrate coated with a buffer layer. An example of the process steps is shown in Fig. 3.5.

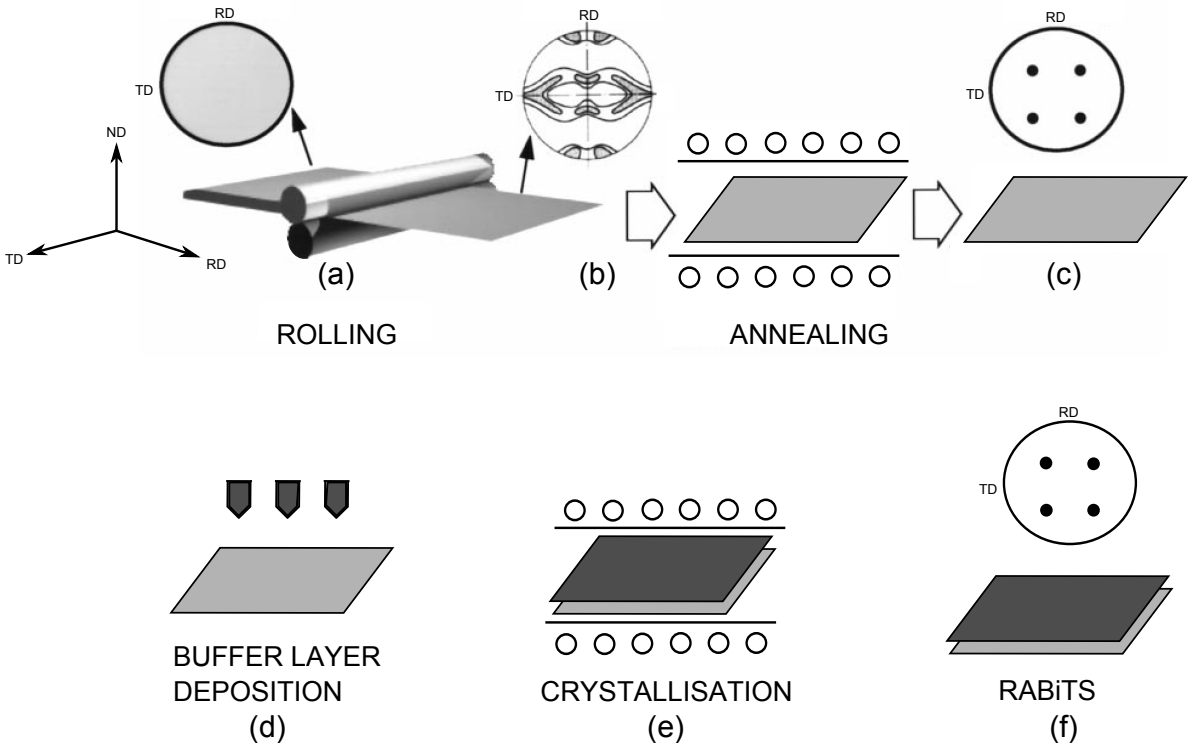

Figure 3.5: Schematic representation of the RABiTS technique and {111} pole figures. (a) rolling, (b) annealing, (c) strongly cube-textured metal substrate, (d) buffer layer deposition, (e) buffer layer crystallisation heat treatment and (f) final RABiTS tape. Reproduced after [38].

A Ni bar is cold-rolled multiple times (see Fig. 3.5(a)) applying a certain per pass reduction (PPR) in order to obtain a homogenous deformation across the material. The final tape thickness is typically 80-100 μm. Very high ($> 90\%$) total thickness reductions (TTR) are generally needed

in order to obtain a strong copper-type rolling texture in pure Ni [38]. Such a rolling texture is apparent in the corresponding (111) pole figure in Fig. 3.5(b) after heavy cold rolling. This texture generally contains the following components; Cu {112}<111>, S {123}<634> and Brass {011}<211>. The heavily deformed nickel is subsequently annealed during a heat treatment at an elevated temperature (e.g. 1000 ^{o}C for 4 hours in vacuum) and a strong cube texture with an ideal {001}<100> orientation develops during recrystallisation. The strong texture is indicated by the four spots in the {111} pole figure in Fig. 3.5(c). Recovery and recrystallisation is driven by this release of stored energy accumulated during deformation and the microstructure is again changed significantly upon annealing of the material as new strain-free grains grow. A buffer layer is deposited and subsequently crystallised in a heat treatment, see Fig.3.5(d) and (e), respectively. Finally, a strongly bi-axially textured and buffered technical substrate is obtained.

The RABiTS technique is particularly interesting from a commercial point of view since well established large scale manufacturing methods such as rolling and annealing can be used in order to obtain substrates with a very strong texture and sufficiently low surface roughness. The out-of-plane and in-plane misorientations are typically characterised by FWHM values $\Delta\omega \sim$ 5-7^o and $\Delta\phi \sim$ 4-6^o. This corresponds to ∼99 % area fraction of cube texture within a deviation angle of 10^o from the ideal {001}<100> orientation [11,40]. High quality RABiTS are currently commercially applied for production of CCs by American Superconductors (AMSC) using the Ni-5at.%W alloy. An $I_C \sim$ 300 A/cm-width[1] have been demonstrated in 500 m long CC tapes prepared using MOD on this Ni-5at.%W substrate with a final width of 10 mm [41], while higher I_C values have been obtained in shorter lengths [42]. Note that these commercial available CCs are characterised by single side coating and fabricated using techniques which are not considered environmentally neutral.

Substrate surface roughness

The substrate surface roughness is significantly affecting the texture and thus J_C of YBCO thin films. For example, Obradors et al.[43] observed that c-axis orientation and J_C of CSD-YBCO films grown on $SrTiO_3$ single crystalline substrates decreased when the root mean square (RMS) surface roughness of the substrate increased as shown in Fig.3.6.

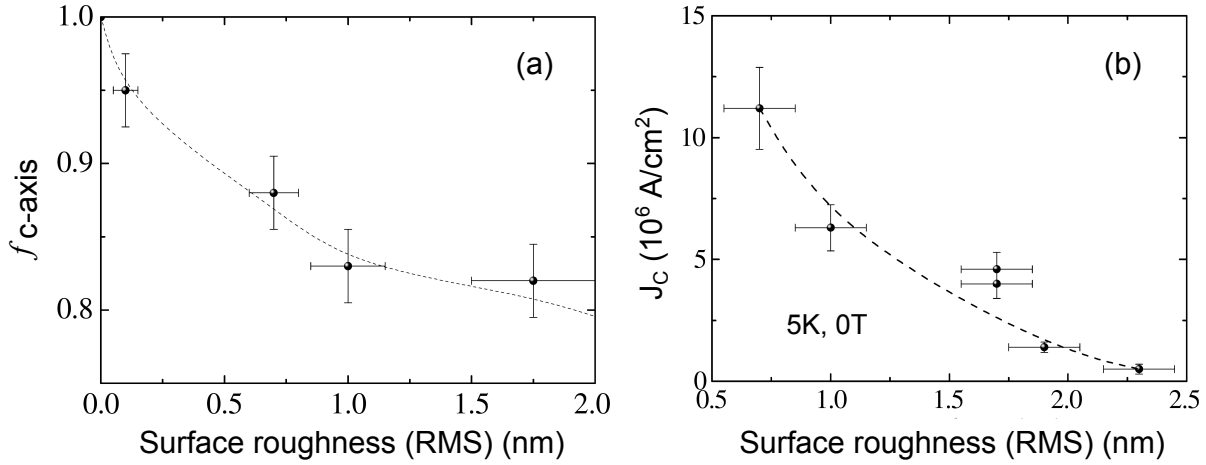

Figure 3.6: (a) fraction of c-axis orientation, and (b) critical current density (J_C), as a function of substrate surface roughness [43].

[1]Note that A/cm-width corresponds to the I_C measured in a 1 cm wide CC.

A smooth substrate surface is necessary in order to obtain a high J_C and the surface roughness of such a single crystalline substrate should represent the surface roughness of a smooth metal substrate.

Grain boundary grooving and grain boundary migration

Significant GB grooving of Ni-5at.%W is however apparent after annealing at elevated temperatures, i.e. a deep profile develops perpendicular into the surface during the annealing. A schematic example of a groove formed at a GB is shown in Fig. 3.7.

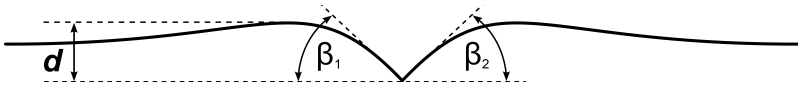

Figure 3.7: Schematic drawing of a GB groove defining the depth and the dihedral angles β_1 and β_2, which differ for an asymmetric groove.

An accumulation of material is indicated by the small peaks on each side of the groove wall and is considered to be a result of surface diffusion [44].

In this thesis, the depth is defined as the vertical height difference between the groove root and top of the highest groove wall, see Fig. 3.7. The thermal grooving mechanism is related to the GB plane area which is reduced in order to reduce the associated free energy of the plane. The grey rectangle in Fig. 3.8 represents the reduced area of the GB plane between two adjacent grains.

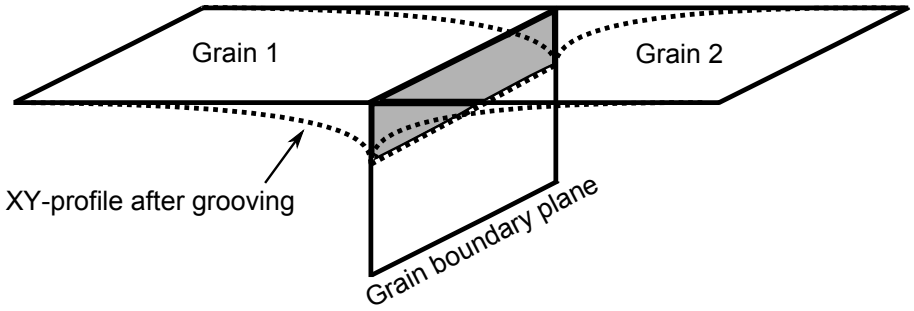

Figure 3.8: Schematic drawing of a grain boundary, before (solid line) and after (dotted line) thermal grooving.

In general, a surface groove will develop at a GB in a metal when the temperature is high enough to allow for appreciable surface diffusion [45,46].

The width and depth of grooves depend on the annealing temperature, annealing time, the GB energy, the surface energy and the diffusion coefficients of the GB [47,48]. For example, using the same annealing time, deeper grooves have been observed for pure nickel annealed at 1000 ^{o}C compared to grooves developed during annealing at 600 ^{o} [49]. Furthermore, the surface roughness increased to a level above that induced by cold rolling of a pure nickel tape when GBs were grooved during annealing.

The GB energy is e.g. related to the misorientation and the material composition [39,50]. Typically deep grooves develops with increasing θ as observed in strongly cube-textured Ni-10at.%Cr substrates annealed in vacuum at 900 ^{o}C for 4 h [48].

These grooves may negatively influence the formation of a homogeneous buffer and RE-BCO layer. For example, Fig. 3.9 shows GB grooves that are transferred from a Ni-5at.%W substrate to a LZO buffer layer. Additionally, substrate surface defects such as pin-holes are also apparent in the buffer layer.

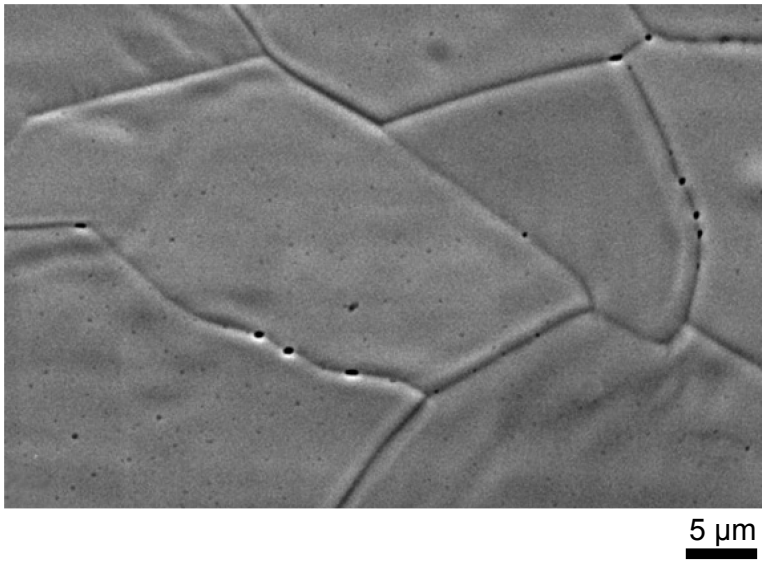

Figure 3.9: Scanning electron microscopy image of a LZO buffer layer on a Ni-5at.%W substrate [51].

Several authors [52, 53] have suggested that the groove associated with the GB is the main problem in relation to growth of a homogenous buffer and superconducting layers.

Substrate boundary migration

A long annealing time promotes grain growth and the GBs therefore move. GB grooves may effectively limit GB migration at the surface. Such an anchoring effect has been observed in pure copper [46]. The boundary is anchored at the groove and the effectiveness of the groove as an anchor depends mainly of the dihedral angle (β). However, thermal grooving progresses with time and the groove profile develops. The initial position of the GB at the surface is changed as β exceeds a certain critical angle (β_C) due to further thermal grooving at the GB. Boundary surface migration may therefore occur in a spasmodic mode since the boundary on the surface moves only when $\beta > \beta_C$. A critical angle $\sim 3^o$ has been reported for pure copper annealed at 980 ^{o}C [46]. Accordingly, GBs are expected to develop grooves while the GB is anchored and it will then move to a new position and develop a new groove.

A very smooth substrate surface with an overall surface roughness $<$ 3-4 nm (including GBs) can be obtained by polishing [54]. However, polishing the substrate after recrystallisation using mechanical polishing will induce a deformation layer and, possibly, undesirable deformation texture. Accordingly, mechanical polishing of the substrate should be performed before the recrystallisation annealing.

Inevitably, substrate temperature and oxygen control at elevated temperatures are central parameters for all deposition techniques. It is very important to notice that while substrate temperatures ranges from about 400 to 900 ^{o}C for thin films grown using PVD techniques [55] even higher temperatures of 1000-1150 ^{o}C are needed for some buffer layers in order to form the correct crystallographic phases using CSD techniques [56, 57, 58]. Meanwhile, recrystallisation heat treatments of Ni-5at.%W are performed at 950-1200 ^{o}C and the crystallisation temperature is thus equal to, or higher, than this temperature [40,59]. The increased annealing temperature is expected to result not only in deeper thermal grooves but also migration of grooves [45].

Substrate oxidation

Obviously, annealing a metal alloy substrate at elevated temperatures in an oxygen atmosphere will produce an oxide layer. Even for a buffered substrate, i.e. substrate with one or more buffer layers, cations or oxygen may diffuse through the layers, during RE-BCO deposition or subsequent oxygenation, resulting in Ni-oxides being formed on the substrate surface. This can affect the texture formation in the subsequent buffer layers, increase surface roughness or even result in delamination of the stack when applied in technical installations, such as a generator. Diffusion of Ni-ions into the RE-BCO layer may have a detrimental effect on the superconducting layer.

For RABiTS materials such as Ni-5at.%W, Ni diffusion by growth of NiO is effectively limited by a YSZ layer [51,60] while W diffusion is limited by a Y_2O_3 layer [11]. Importantly, GBs in the substrate material was reported to constitute a channel for oxygen diffusion due to higher concentration of crystalline defects in the buffer layer at the substrate GB grooves [52]. Consequently, substrate GBs do not only suppress the superconducting properties in the RE-BCO layer due to the weak-link behaviour but may additionally act as oxygen path which may lead to an overall devastation of the superconducting property of the above deposited superconducting layers. It is apparent that a substrate with a strong texture, limited lattice mismatch and sufficient mechanical strength are not the only requirements. Control of the substrate surface quality is also of great importance.

Percolation path and GBs

A possible effect of the GB grooving and oxidation is related to the general performance of the CC. An example SEM micrograph of a YBCO-YSZ-CeO_2 film architecture deposited on a Ni-based RABiTS with PLD is shown in Fig. 3.10.

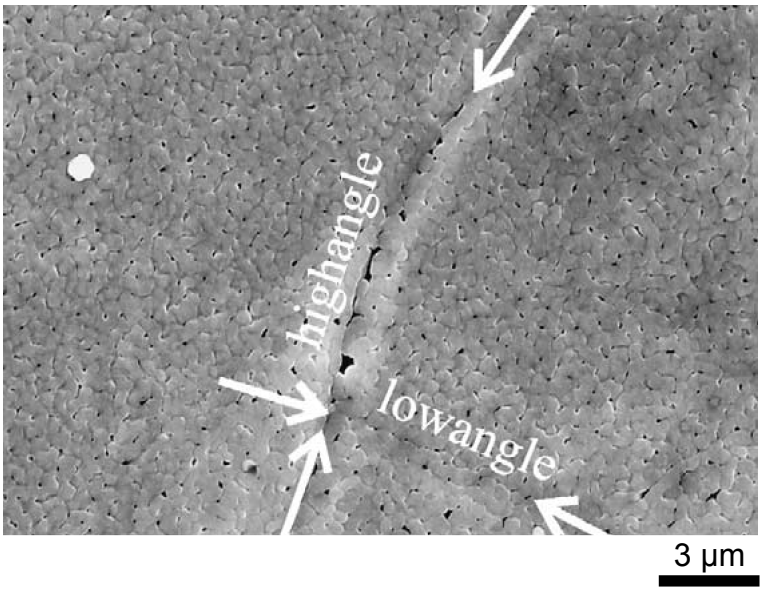

Figure 3.10: Scanning electron microscopy image showing a LZO buffer layer on a Ni-5at.%W substrate. Arrows indicate positions of a HAGB and LAGB in the metal substrate [47].

The crucial effect of the HAGB and associated groove in the substrate (see Fig. 3.9) results in discontinuous regions in the YBCO layer as shown in Fig. 3.10. J_C is therefore reduced at these boundaries in the RE-BCO layer. The GBs may therefore constitute a network with limited J_C which can result in a so-called percolation path in the CC. An example magneto optical picture of a RABiTS based CC is shown in Fig. 3.11(a).

Figure 3.11: (a) Magneto optical measurement of a RABiTS-based coated conductor tape with an applied transport current equal to I_C at 77 K and self-field [15] and (b) drawing of the grain boundary network in the strongly textured substrate of the RABiTS-based coated conductor in (a). The red line indicates a percolation path along the grain boundaries in the substrate.

A lower J_C enables a moving vortices that forms along these boundaries and this part of the GB network therefore constitutes the "weakest link" in the CC and a percolation path is clearly observed from one side of the CC to the other. The path corresponds directly to the boundaries in the metal substrate which is schematically drawn in Fig. 3.11(b).

Chapter 4

Magnetism and alternating current losses

A ferromagnetic (FM) metal substrate will cause energy losses in the superconducting RE-BCO layer when a CC is operated in alternating current (AC) applications. Ni-5at.%W is a ferromagnetic material with a Curie temperature, $T_{cu} \sim 335$ K. It is therefore also ferromagnetic at typical operation temperatures of coated conductors (< 77K) [61]. Alloying of Ni with non-ferromagnetic elements is a well known technique for reducing T_{cu} of Ni-based metal tapes and thereby reducing energy losses caused by the FM substrate [47].

This chapter will introduce definitions of magnetic properties relevant to the results obtained in this thesis. Additionally, the concept of ferromagnetism and energy losses in superconducting wires when alternating currents are applied is also included. More elaborate introductions to magnetism are found in Blundell [62] and Bozorth [63] while an introduction to energy losses in superconductors can be found in Fossheim and Sudbø [10].

4.1 Magnetic moment

Magnetisation is the sum of individual atomic magnetic moments, μ, i.e. M = μ·N, where N is the number of atoms. The magnetisation of a material is related to the magnetic induction (**B**) and the magnetic strength (**H**) as follows:

$$\mathbf{B} = \mu_0(\mathbf{H} + \mathbf{M}) \tag{4.1}$$

where μ_0=4π·10^{-7} Hm^{-1} is the permeability of free space. The atomic magnetic moment, μ, from a single electron orbiting the nucleus of a hydrogen atom is defined as the *Bohr magneton*, $\mu_B = \frac{e\hbar}{2m_e} = 9.274{\cdot}10^{-24}$ Am^2 and is typically used as a reference value when measuring magnetic moment of different materials.

In general, the magnetic moment of an isolated ion with many electrons depends on how the electronic orbitals (or shells) and sub-shells are filled and therefore on the total angular momentum (**J**=**L**+**S**), where **L** and **S** are the orbital and spin angular momentum, respectively. The latter depends on the electron spin state and is associated with a quantum number (m_s) which for an electron takes on a half integer value ($\pm\frac{1}{2}$) and is usually described as either spin up (↑) or down (↓). The effective magnetic moment of an ion can be written as

$$\mu_{eff} = g_L \cdot \mu_B \sqrt{J(J+1)} \tag{4.2}$$

where g_L is the Landé g-factor[1] and J is the total angular momentum quantum number that can take on integer or half-integer numbers (0, $\frac{1}{2}$, 1, $\frac{3}{2}$,...) [62].

[1]The g_L-factor is related to specific values of L and S and is generally equal to 2 when considering only spin in a ferromagnet [63].

Hund's rules

The orbital filling in the isolated ion is dominated by electron-electron Coulomb interactions followed by interaction between the resulting electron spin and its orbital angular momentum (spin-orbit coupling). Hund's three rules describe how, in a decreasing order of importance, one should first maximise **S**, then **L** and finally combine them to the total angular momentum **J**, when "filling" electrons into the individual sub-shells of the ion [64].

Orbital quenching

Significant differences (Δ) between μ_{eff} and μ_{exp} are observed for most of the 3d ions. For example, $\Delta\sim44\%$ for Ni^{2+} ions. The great discrepancy for this class of ions is related to electrostatic interactions (crystal fields) between the specific surrounding ions in a lattice which is neglected in the isolated ion approximation. In contrast to e.g. the 4f ions, the electronic configuration in 3d ions is dominated by electron-electron interaction followed by the crystal field interactions, i.e. static electric fields that strongly depend on crystal symmetry and originate from the charge distributions of the neighbouring atoms. An *orbital quenching* effect results (**L**=0) and spin-orbit coupling may consequently be ignored for the ground state to a first approximation. Interestingly, estimates of the ground state using only **S** gives much better estimates for most of the 3d ions (including Fe^{2+} and Co^{2+}) and deviates with less than 10% from experimental values of μ for Ni^{2+} ions [62]. It is evident that the electron spins play a dominating role for the magnetisation of these particular materials. In contrast to the orbital energy levels in isolated ions or atoms, electronic states in a crystalline metal are generally described by energy bands [64]. Fig. 4.1 shows how the 3d and 4s energy bands of Fe, Ni and Cu metals are filled.

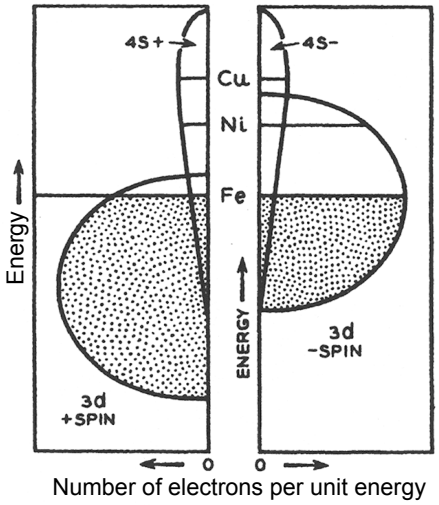

Figure 4.1: Schematic drawing of the electron filling of the energy bands in iron, nickel and copper [63].

As can be seen in Fig. 4.1 both Fe and Ni have uncompensated electrons in the partially filled 3d band while the 4s band is also partially filled. Note that the energy level of the highest occupied state is known as the Fermi level [64]. The 3d band is the most important energy band for the ferromagnetic materials Fe, Co and Ni due to a relatively large peak in the density of states at the Fermi level compared with e.g. the 4s band [63].

4.2 Ferromagnetism

Ferromagnetism refers to a spontaneous magnetisation in the absence of applied magnetic field. The magnetisation tends to lie along a so-called easy axis and may depend on e.g. crystal structure and magneto-crystalline anisotropy [62]. The spontaneous magnetisation vanishes above a critical temperature known as the Curie temperature (T_{cu}).
The Heisenberg 3D model is commonly applied when evaluating T_{cu} of ferromagnetic substrates for CCs [65]. The magnetisation just below T_{cu} is in this model is well described by a power law:

$$M \sim (T_{cu} - T)^{\alpha} \tag{4.3}$$

where $\alpha \sim 0.33$ [64].

An ideal ferromagnet is characterised by a quantum mechanical ground state where all magnetic moments are parallel, i.e. a long range order is apparent at low temperatures. This is due to a so-called exchange energy which tends to align all spins parallel. The FM order is progressively destroyed as the temperature increases and vanishes at T_{cu} as shown in Fig. 4.2.

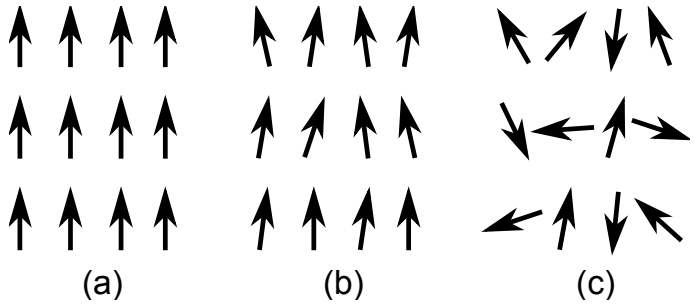

Figure 4.2: (a) Long range parallel electron spin order, $T<<T_{cu}$, (b) thermal fluctuations result in lower order $T<T_{cu}$ and (c) no long range order at $T \geq T_{cu}$.

Obviously, this is an oversimplified description of the FM state and real materials, such as nickel, have magnetic domains that divide the material into smaller volumes each with an uniform saturated magnetic moment.

Magnetic hysteresis and domains

A FM domain is a small region in the material where the local magnetisation is saturated. Domains are separated by so-called domain walls and the spin direction is changed only inside the wall. Formation of domains wall is a balance between the formation energy related to the rotation of spins and the energy associated with the so-called demagnetisation energy. These walls move when a magnetic field is applied since domains with a favourable aligned magnetic moment are growing on expense of domains with moments aligned different from the applied field. Additionally, at large applied fields rotation of domains may also occur. Domain walls can be pinned by e.g. strain fields, surfaces, and impurities and therefore, in general, depend on the metallurgical properties of the material. The coercivity field (H_{co}) is defined as the applied field necessary to completely demagnetise a FM material after saturation has been obtained. H_{co} increases as domain walls are pinned with increasing strain and a heavily strained Ni-tape is therefore a so-called "harder" ferromagnet than an annealed Ni-tape [62]. The recrystallisation annealing is therefore an extra beneficial factor for Ni-5at.%W since the strain state is the lowest possible and the ferromagnet is thus magnetically "softer". This in turn has a small positive effect on the energy losses encountered when utilising such FM substrate in CCs for AC applications [65].

Application of an external field below the Curie temperature aligns a fraction of the domains along the axis of the field direction. Fig. 4.3(a) shows a typical magnetisation curve for a FM material below the Curie temperature.

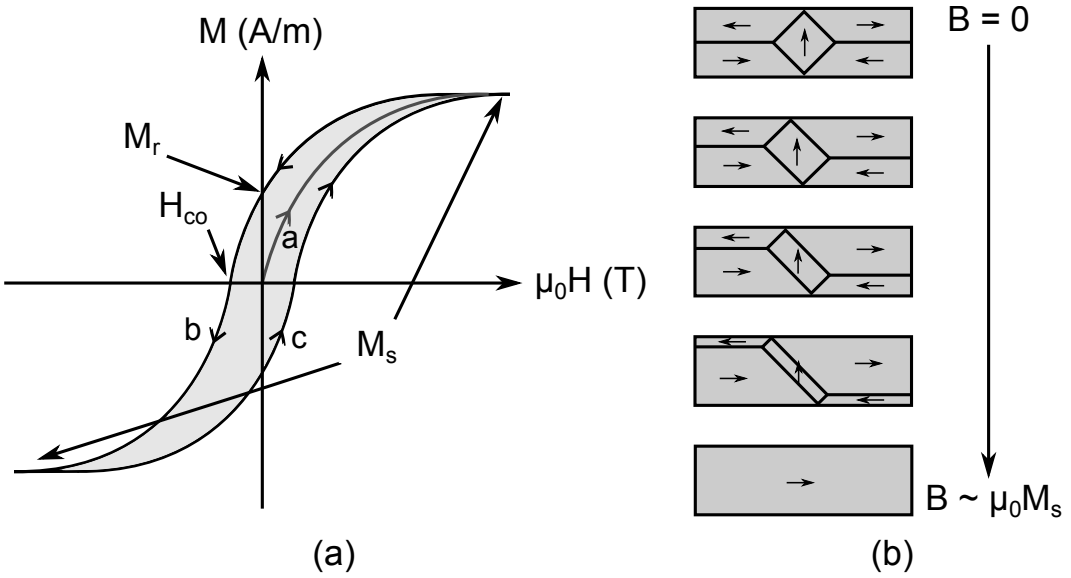

Figure 4.3: (a) schematic presentation of the magnetisation as function of applied magnetic field (M-H loop) of a ferromagnetic material. Arrows on the loop indicate the ramping direction of the applied magnetic field, and (b) changes in a schematic domain structure with increasing applied field. Reproduced after [66].

The magnetisation first follows line (a), then (b) and finally (c) in Fig. 4.3(a). A schematic of the domain structure as function of applied field typical for line (a) is shown in Fig. 4.3(b). All the magnetic moments may initially sum to zero net moment and after saturation this situation is changed, i.e. the magnetisation does not vanish at zero applied field but a remanent magnetisation (M_r) is present. Furthermore, the magnetisation saturates at M_s as the applied field increases thus aligning all available spin. However, no further increase is observed with increasing applied field which is in contrast to e.g. a paramagnet. Hysteresis is observed as the area enclosed by the M-H loop and is caused by the domains which tend to oppose the applied field. A FM hysteresis loss is therefore causally related to the irreversible motion of domain walls [66].

Saturation mass magnetisation

The modified Weiss theory of FM describes a linear relation between T_{cu} and M_s as

$$T_{cu} = K \cdot M_s \tag{4.4}$$

where K is a constant that depends on **J**, g_L and a molecular field constant [63]. Accordingly, a decrease in T_{cu} will also result in a decrease in M_s, which is directly related to the effective magnetic moment of the material.
μ_{eff} can be calculated from the saturation mass magnetisation, M_{sat} (Am^2g^{-1}):

$$\mu_{eff} = \frac{\Omega \cdot M_{sat}}{N_A} \tag{4.5}$$

where Ω (g/mol) is the atomic weight and N_A=6.022·10^{23} mol^{-1} is Avogadros number. For example, Ni is characterised by M_{sm}^{Ni}=5.75·10^{-2} Am^2g^{-1} and Ω_{Ni} = 58.69 g/mol. Accordingly,

$\mu_{eff}^{Ni} = 0.6\mu_B$ which is directly related to the total band electron vacancy in nickel, i.e. the uncompensated 3d-spins, that results in a net magnetic moment. Note that $\Omega = \frac{m \cdot N_A}{N}$, where m (g) is the sample mass and N is the number of Ni ions, was used for calculating μ_{eff} in this work.

The magnetic susceptibility, $\chi_m \simeq \frac{\mathbf{M}}{\mathbf{H}}$ is typically very large for FM materials. Accordingly, $\mathbf{M} >> \mathbf{H}$ and the saturation flux density $\mathbf{B}_S \sim \mu_0 \mathbf{M}_s$. It is therefore, in general, not necessary to apply magnetic fields much higher than ∼0.6 T in order to measure the saturation mass magnetisation of a Ni-based metal tape. Note that both **B** and **H** is changed due to the so-called demagnetisation field (H_d) of a FM material in an applied field depending on the sample geometry. However, the saturation mass magnetisation value is not affected by H_d. A discussion of H_d for a tape geometry is included in appendix B.

4.3 Alternating current losses

There are several types of energy loss in a CC. The loss (Q_{AC}) encountered in AC applications include hysteresis losses in the superconducting RE-BCO layer itself (Q_s) and losses due to a FM substrate (Q_{FM}):

$$Q_{AC} \sim Q_s + Q_{FM}. \tag{4.6}$$

Importantly, the direction of an applied magnetic field has a great effect on which type of loss is the dominating loss in a CC. In general, the AC losses are dominated by losses originating from the superconductor itself for fields perpendicular to the CC plane while the losses of a FM substrate is dominating for fields parallel to the plane of the CC [67]. It should be noted that there are also general cryogenic losses and eddy current losses due to magnetic coupling to metallic parts (such as the metal substrate and copper layers).

Superconductor hysteresis losses

The superconducting hysteresis loss (Q_s) in the RE-BCO layer itself depends in general on the frequency of the alternating current, the width (w) of the superconducting layer, J_C and the amplitude of the magnetic field. The loss per field cycle can be estimated as

$$Q_s \sim B \cdot J_C \cdot w \cdot n. \tag{4.7}$$

where n is a demagnetisation factor [10]. Alternatively, the theory by Norris [68] provides a direct estimate of the superconducting loss (Q_N) for a long isolated conductor with J_C independent of field and is commonly used for estimating AC losses of the CCs [69]. The loss per cycle per meter in this theory is given by $Q_N = \frac{\mu_0 I_0^2}{2\pi}$, where I_0 is the AC peak current.

An interesting method for decreasing hysteresis losses in the RE-BCO layer itself is narrowing the width of the CC. Simply viewed, vortices travel a shorter path between entering and exit of the CC from the side in a narrow CC compared to a broader CC. Stripping and narrowing techniques are therefore commonly developed with the aim of producing CCs with closely packed RE-BCO strands with a suitable width.

An important outcome of this Ph.D.-project is a patent application related to "AC application optimised CCs" which has been registered at the European Patent Office in May 2012 with the author as inventor.

Hysteresis losses and ferromagnetic substrates

The FM substrate generates an energy loss in the superconducting layer when the CC is applied in AC applications. A simple example is an alternating transport current which generates an

alternating magnetic field in a CC. This field will then interact with the FM substrate material and thus the domains and the domain walls [70]. Obviously, handling such as bending and cutting of the CC will introduce strain to the material and thus increase H_{co} slightly. It is however assumed that H_{co} is at a minimum due to the recrystallisation annealing of the substrate and therefore not considered further here.

The classical ferromagnetic hysteresis loss per cycle scales as

$$Q_{FM} \sim B^2 \tag{4.8}$$

and is in good agreement with experiments and for a wide range of frequencies [71]. Additionally, Q_{FM} have been observed to be nearly proportional to the frequency in CC. The loss can be completely avoided by decreasing T_{cu} of the Ni-based substrate below the operation temperature of the CC which is typically < 77 K [9,10]. Alternatively, decreasing M_s to a level so that $Q_{FM} \leq Q_s$ would also be beneficial since further decreasing Q_{FM} would not affect the total loss [65,73].

The maximum loss encountered due to the FM substrate scales with the maximum flux density equal to $\mathbf{B}_s{}^2$. Accordingly, reducing M_s and thus B_s by a factor of 10 reduces the loss by a factor of 100 [73]. An estimation of this energy loss can thus be made by either measuring M_{sat} or calculating the area enclosed by the M-H loop [69].

Studies of YBCO deposited on RABiTS based on pure Ni substrates showed an increase in total AC loss by a factor ∼100 compared to YBCO films deposited on $SrTiO_3$. This was measured within a frequency range of 22-256 Hz and current densities up to J_C of the respective YBCO thin films at 77 K [74]. Consequently, this additional loss must be attributed to the FM Ni substrate. M_s of a suitable metal substrate should therefore be reduced with a factor of 10 compared to pure Ni (M_{sat} = 57.5 Am^2/kg) [69]. It is therefore beneficial to reduce M_{sat} to ∼5 Am^2/kg, since the FM substrate will not impose any additional loss to the CC compared to the loss of the superconducting layer itself [65, 73].

FM loss example

An example of the AC loss due to the superconductor and the FM substrate was made by Thompson et al. [69]. They estimated the loss of a RABiTS-based coated conductor operated at 60 Hz assuming the width was 8 mm, the YBCO layer thickness was 2.5 μm with a J_C = $1{\cdot}10^6$ A/cm^2 at 77 K and the substrate was 50 μm thick. Consequently, Q_N = 0.46 mJ/m in the case of $I_0 = I_C/2$ = 100 A for the AC loss of the superconducting layer. The commonly applied figure-of-merit (FOM) is the power loss per kA-m. It is obtained by multiplying with the frequency and the current ratio ($1kA/I_0$) and consequently FOM = 0.27 W/kA-m for $I_0 = I_C/2$ at 60 Hz. However, it should be mentioned that the loss calculated for the superconductor according to the Norris model is very sensitive to e.g. the tape geometry and I_0.

The corresponding loss due to the FM substrate was estimated to be 0.43 W/kA-m for pure Ni and 0.043 W/kA-m for Ni-7at.%Cr [69]. Accordingly, the FM substrate added a significant loss to the total loss in the case of a pure Ni substrate which is in good agreement with that observed by Kerchner et al. [74]. Adding 7 at.% Cr to the Ni significantly decreased the FM loss. The increase in the total loss due to the substrate for this alloy is therefore ∼ 16 % for these particular conditions [69]. Note that M_{sat} = 23.1 Am^2/kg for Ni-7at.%Cr and that the loss based on equation 4.8 compared to pure nickel is also about 16 %.
Accordingly, in this thesis, the FM loss is estimated by comparison with the reference value of the saturation mass magnetisation of pure Ni.

Ni-based alloys with low Curie temperature

Solid solution alloying of Ni with non-FM elements is a well known technique to decrease T_{cu} and M_{sat} of Ni-alloys. Comprehensive studies were conducted by de Boer et al.[47] on macro-alloyed Ni-based strongly textured substrates. They demonstrated a significant decrease in T_{cu} of these binary alloy tapes by adding non-FM elements such as Mo, V and Cr to Ni, as shown in Fig. 4.4.

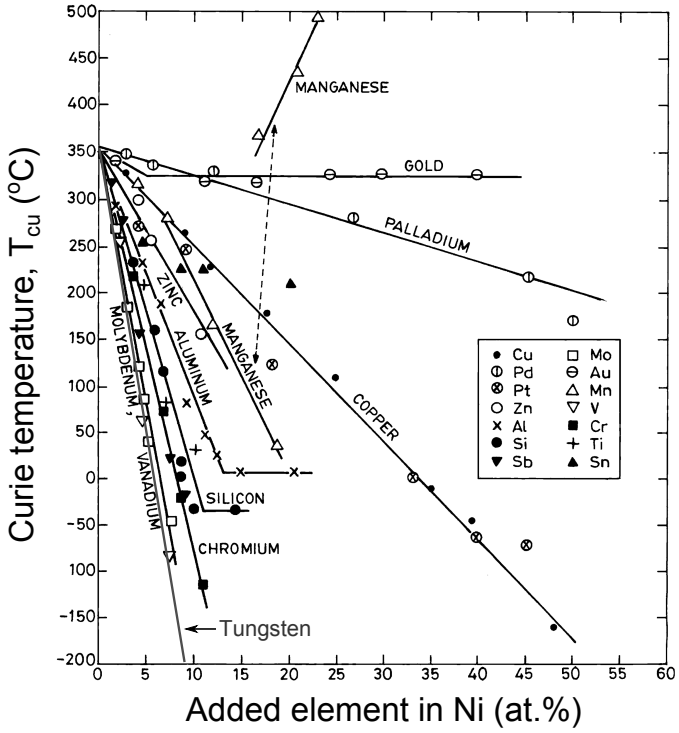

Figure 4.4: Curie temperature as function of added element in nickel [47]. The "tungsten"-line is extracted from Sarma et al. [61].

Clearly, additions of W, Mo, V and Cr are a very effective way for decreasing T_{cu} and thus M_{sat}. Note, that the tungsten data presented in Fig. 4.4 is not the original data by de Boer et al. [47] but extracted from [61] and presented here in order to compare the effect of W on T_{cu} with the other elements. Adding W to Ni is clearly the best candidate for decreasing T_{cu} followed by Mo, V and Cr. Unfortunately, extensive alloying with e.g. W results in a lower fraction of recrystallisation cube texture. This may be explained by a rolling texture that is different from the copper-type and accordingly related to a typically lower SFE of the alloy [75]. Ni-9at.%W is one example of extensive alloying with W. The resulting substrate has superior properties with respect mechanical strength, T_{cu} = 25 K and $M_{sat} \sim 4$ Am^2/kg and is thus below 5 Am^2/kg. However, the fraction of cube texture within 10^o from the ideal cube orientation is generally decreased compared with Ni-5at.%W substrates [76].

Alternatively, solid solution ternary alloys with combinations such as Ni-W-Cr, Ni-Cu-W, Ni-Cu-Co have also been investigated [72,73, 77, 78]. However, most of these ternary systems suffered in general from a low mechanical strength and/or undesired oxides on the substrate surface. Note that composite substrates have also been developed with the aim of reducing AC losses due to the ferromagnetic substrate [71,79].

4.4 Research hypothesis' of the thesis

Clearly, control of the substrate surface characteristics such as texture and surface roughness are a basic necessity in production of CCs.

Based on the topics discussed in chapters 3 and 4, I have identified the following research hypothesis', which are important aspects that should be investigated to further improve RABiTS-based substrates for CCs with respect to reel-to-reel fabrication and AC loss reduction.

1 - Effect of initial surface quality on texture and surface roughness after mechanical polishing and annealing of Ni-5at.%W

Extensive cold-rolling of a hard Ni-5at.%W tape will eventually result in a poor surface quality of the rolls characterised by a high surface roughness. The quality of the subsequently deposited buffer and superconducting layers are very sensitive to the substrate surface quality. Preparation of long CCs in a reel-to-reel system may therefore involve polishing of the metal substrate. Mechanical polishing is a possible technique by which a smooth surface with a low tape surface roughness can be obtained. However, this technique must be applied before the recrystallisation annealing. It is therefore important to consider how the surface changes in the metal substrate after the annealing and if there is an effect on a buffer layer deposited on such polished and annealed metal substrates.

2 - Texture and topographic changes after an additional heat treatment of Ni-5at.%W

Surface grooves on the substrate surface may have a significant influence on the epitaxial growth of the subsequent ceramic layers. The delivery condition of annealed and recrystallised Ni-5at.%W tape is typically characterised by a strong texture and low surface roughness. However, changes may occur during further heat treatments, i.e. buffer layer and RE-BCO crystallisation. Additionally, the ceramic crystallisation temperature is typically higher compared to the temperature used for substrate recrystallisation. It is therefore important to investigate changes in the topography and the texture in the metal substrate material after an additional heat treatment simulating conditions of e.g. buffer layer crystallisation.

3 - Strongly textured Ni-based substrate with optimized properties for CC applied under AC conditions

Energy loss in CCs which is caused by a ferromagnetic substrate may be significant compared to the total AC loss of the CC. The FM loss can be lowered by decreasing T_{cu} and M_{sat} of the substrate material. Alloying Ni with non-ferromagnetic elements is a known method for obtaining such improved magnetic properties of the substrate. However, significant alloying of Ni typically results in a decreased fraction of cube texture. Therefore, alloying with a non-FM metal, which can also be strongly textured using the RABiTS technique, could improve the magnetic properties while still enabling a strong recrystallisation cube texture. Accordingly, starting with the Ni-5at.%W alloy (keeping the Ni-W ratio constant) additional alloying with Cu should be investigated as a route for making a potential new candidate material for strongly textured metal substrates applicable for CC under AC conditions.

Part II

Materials and Experimental techniques

Chapter 5

Materials and fabrication techniques

5.1 Materials

High purity and large volume metal ingots can be obtained by induction melting or powder metallurgy while the size of ingots produced using laboratory arc melting systems is limited to smaller volumes (<100 g nickel). The latter ingots may however be of very high purity, representable for ingots produced by large scale methods and cost effective with respect to material usage for research purposes. A series of Ni-5at.%W ingots were produced, hot forged and cold rolled into tapes and subsequently annealed by the author. The main criteria of the substrate quality were a >98% fraction of cube texture within a deviation angle of 10^o from the ideal {001}<100> orientation evaluated by EBSD and a smooth homogenous surface evaluated by atomic force microscopy for a tape thickness of 80-100 μm. After establishing a preparation technique that would ensure a high substrate quality in Ni-5at.%W substrates a series of new ternary substrates were prepared.

Three different solid solutions alloys of Ni-Cu-W were prepared, starting from the Ni-5at.%W which can form a strong recrystallisation cube texture. The compositions were chosen according to the solid solution region (grey rectangle) in the Ni-Cu-W phase diagram shown in Fig. 5.1.

Clearly, the solid solution region is relatively limited at 20 ^{o}C and it should be noted W is generally considered insoluble in Cu [80].

5.1.1 Material impurity level

Importantly, very low concentrations (∼10 atomic part per million) of particularly sulphur is known to negatively influence the formation of cube texture in Ni-based substrates [81]. In contrast, micro-alloying with Mo, W or Ag has been demonstrated to significantly reduce the effect from sulphur [82]. It has also been reported that the formation of a strong recrystallisation cube texture in Ni is hindered if the purity is below 99.98 % [83] .

Thus, all starting materials used were of very high purity (99.99%) in order to limit uncontrolled changes in the microstructure and texture during recrystallisation.

5.2 Fabrication techniques

The following section includes the procedure developed by the author for producing metal tapes and some important technical findings.

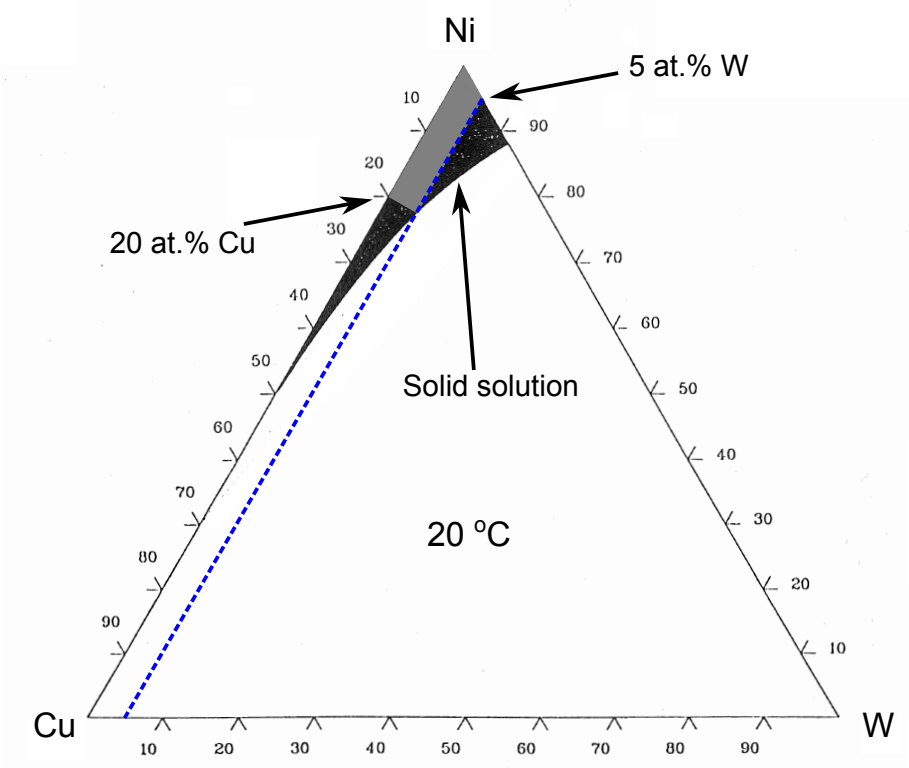

Figure 5.1: Isothermal phase diagram for Ni-Cu-W at 20 ^{o}C [84]. The blue stippled line indicates the 5 at.% W level and the grey rectangle represent the region of solid solution for Ni-Cu-W with 5 at.% W.

5.2.1 Arc melting

A laboratory Edmund Bühler 2414 Arc melter system was used for producing small (∼70 g) Ni-alloy ingots. The vacuum chamber was flushed (with Ar gas) and pumped at least 3 times until a pumping pressure of 10^{-4} mbar was obtained. An argon pressure of 0.5 bar was applied during melting. A schematic of the system is shown in Fig 5.2.

A tungsten tip (1) was placed above the very pure starting materials (2) and an arc was created in the Ar gas between the material and the W-tip. The applied current was between 80 and 100 A. Small pellets were typically melted six times and positioned vertical using the pliers as indicated at (3) in Fig 5.2. These many re-melts and vertical turnings were performed to ensure a high chemical homogeneity in the small pellets. Finally, three re-melts were conducted melting all the small pellets into one larger ingot. Note that by controlling the current very precisely it was possible to melt the material while avoiding significant vaporisation of material and the mass loss was therefore below 1 %.

5.2.2 Homogenisation heat treatment

The final ingot was homogenised in a quarts tube placed in tube furnace with flowing nitrogen (350 ml/min). It was heat treated at 1000 ^{o}C for at least 24 h.

5.2.3 Hot forging

A dendrite microstructure was obtained after melting and such microstructure is typical for cast melted ingots. Hot forging on all facets of the ingot, was applied to decrease the grain size of the material, remove the dendrite structure and shape the ingot into a bar suitable for rolling.

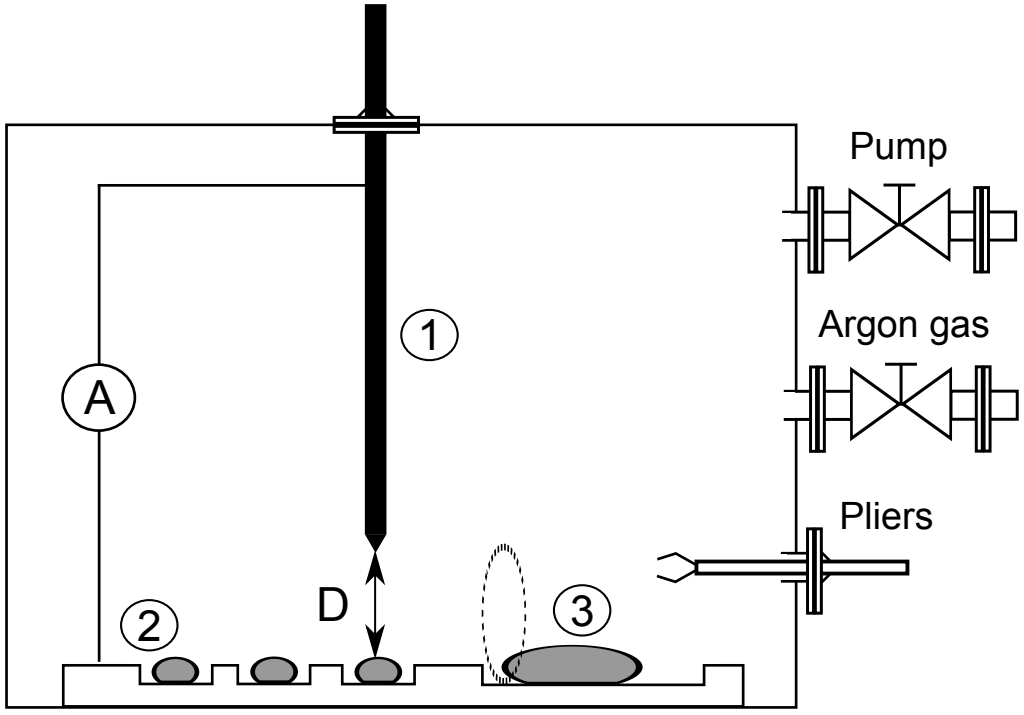

Figure 5.2: Schematic diagram of the arc melting system. (1) tungsten tip, (2) small material pellets, (3) large ingot, (A) current and (D) distance between the tip and sample.

The Ni-5at.%W ingots (section 7.1 and 7.2) were hot forged manually using a large hammer, an anvil and heating with an acetylene burner. The ingot was heated until the ingot colour became "white-yellow" and without melting the surface of the ingot. The Ni-Cu-W ingots (7.3) were prepared by heating to 1200 ^{o}C and hot forged using a pneumatic hammer machine. The metal bars were water-quenched after the final forging pass and a few surface cracks typically developed during the quench. The resulting oxide and cracks were removed mechanically by cutting and grinding. Note that the removed surface layer was $>$ 1 mm thick and the final bars were typically 7-10 mm thick, 12-15 mm wide and 50-100 mm long.

Note that the microstructure was similar on all facets of the bar and that the average grain size for all bars varied between 20 and 40 μm.

5.2.4 Cold rolling and annealing

The bars were cold-rolled applying a 5 % per pass reduction which should result in a homogenous deformation across the material [85]. Two rolling mills with different radii (R_1 = 37.5 mm and R_2 = 10 mm) were used for cold rolling and the rolls had a smooth mirror-finished surface. No lubrication was applied during rolling and the thickness reduction was monitored between each successive rolling pass. The tapes presented in section 7.1 and 7.2 were rolled on mill 1 to thickness of 120-140 μm. The tapes in section 7.3 was initially rolled on mill 1 to a thickness $\sim$1 mm and then rolled to the final thickness (80 μm) on mill 2. Note that a slightly larger per pass reduction (PPR) was applied for the first pass when switching to mill 2 to compensate for the smaller roll radius while still achieving a homogenous deformation.

Furnaces and reel-to-reel simulation

All substrates were cleaned in an ultrasonic bath before annealing. First with acetone for 5 min and then in ethanol for 5 min in order to remove any residues. The samples were dried using

flowing nitrogen.

Two different furnace setups were applied in this thesis work. Furnace setup F1 was developed in order to simulate an annealing condition similar to that in a reel-to-reel system with respect to gas flow, heating and cooling ramps for the samples prepared in section 7.1 and 7.2. The samples prepared in 7.3 were annealed using a standard furnace setup (F2) that could heat up to 1300 ^{o}C and therefore to higher temperatures than the former furnace, but consequently also slower heating and cooling ramps. Notice, that no quartz tube is applied in F2 and that the sample temperature has been calibrated using a thermocouple placed next to the sample.

The samples in section 7.1 and 7.2 were placed inside a quartz tube on the sample holder in close proximity to a thermocouple as shown in Fig. 5.3.

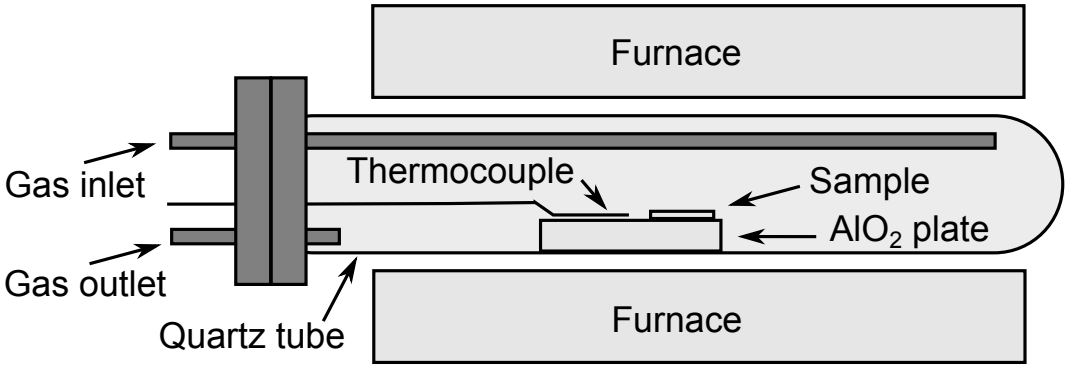

Figure 5.3: Drawing of the F1 annealing setup.

The general procedure for annealing ingots and cold-rolled tapes was to preheat the furnace, pump and flush three times with the cleaned sample in position, keep a constant flow of 350 mL and then insert the quartz tube into the hot furnace. The tube was removed from the furnace without altering the furnace temperature and rapidly cooled. It is clear that the heat ramp (heating/cooling) is not instant and that certain duration of time, 18 and 21 min, respectively, at lower temperatures are unavoidable and similar to the heat profile of a reel-to-reel annealing system.

A mixture of 5 % H_2 in N_2 protective gas was applied to prevent oxidation of the Ni-based tapes. Interestingly, an annealing treatment using this gas will also remove any native oxide formed on a Ni-5at.%W substrate. Notice, that the gas inlet in Fig. 5.3 (a) is positioned so that the gas is flowing over the sample and out at the gas out-let. It is pertinent to mention that the difference, between the furnace temperature and the temperature measured with the thermocouple next to the sample, is significant as seen in Fig. 5.4.

Accordingly, measurement of sample temperature using the furnace thermocouple is not appropriate. It is expected that the great difference (80-100 ^{o}C) is due to the continuous gas flow which will act as a heat sink in combination with the heat capacity of the quartz tube. Such differences should be compensated for by increasing the furnace temperature or altering the furnace setup and clearly shows that monitoring the sample temperature close to the tape at multiple positions in the reel-to-reel is a necessity.

An intermediate annealing is generally performed at a tape thickness ∼3 mm while the necessary total thickness reduction of 97 % is practically achievable, i.e. final tape thickness ∼80 μm. In view of large scale manufacturing and reel-to-reel processing of >100 m long RABiTS, intermediate annealing were avoided due handling of the bar at this intermediate stage. It was considered a great practical challenge to handle such a long inflexible thick tape and excluding an annealing step would shorten the fabrication process.

The samples presented in section 7.1 were annealed at 1020 ^{o}C for 75 min, the sample in section 7.2 at 1000 ^{o}C for 2 hours. The samples in section 7.3 were annealed at 700 ^{o}C for 30

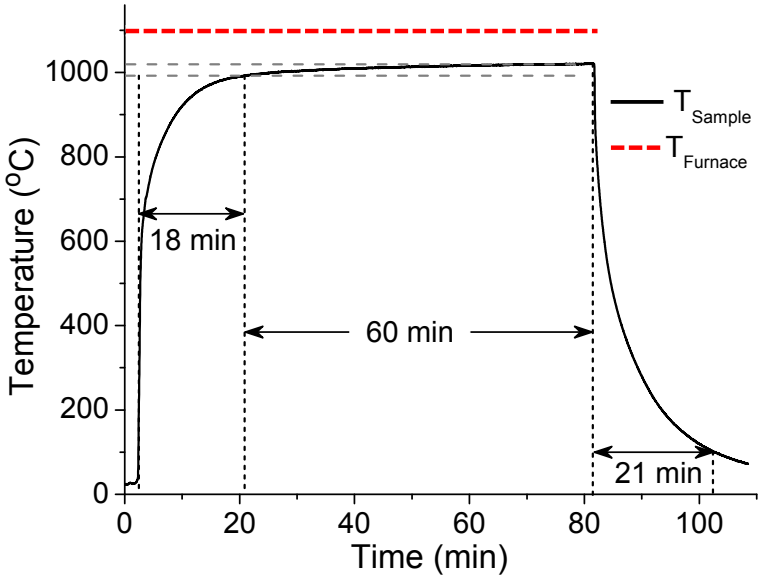

Figure 5.4: Example of an annealing curve for recrystallisation of a Ni-5at.%W tape.

min and the ramped to 1050 °C and annealed for 2 hours at this temperature. The beneficial two step annealing is described in appendix B. The samples in section 7.1 were mechanically polished and coated with buffer layer as described below.

Mechanical polishing of Ni-5at.%W tapes

10×30 mm^2 samples were cut from the longer tape after cold rolling. These samples were glued onto a thick metal disk and all samples were polished simultaneous to ensure a similar polishing of all tapes. Different Struers diamond polishing suspensions with a diamond grain size (DGS) = 0.25, 3, 9 and 15 μm were applied for mechanical polishing of the Ni-5at.%W tapes. The diamond suspension and a lubricant were sprayed onto a rotating polishing cloth. Polishing started with a DSG = 15 μm, then 9, 3 and finally 0.25 μm. The polishing cloth was replaced by a new cloth for each new DGS grade.

$Gd_2Zr_2O_7$ buffer layer

The buffer layer was produced and deposited using dip coating by Dr. Zhao on Ni-5at.%W metal substrates produced by the author.

A solution based on Gd (III) and Zr (IV) 2,4 pentadionate dissolved in propionic acid was stirred for more than two hours at 60 °C until a fully reacted solution with a light yellow colour was obtained. Gd and Zr were added in stoichiometric proportions and the total cationic concentration was 0.6 mol/L. Strongly textured Ni-5at.%W metal substrates were then coated using the dip coating technique applying a withdrawal speed of 20 mm/min. The coated buffer layer was crystallised in a protective atmosphere (Ar/H_2 : 95/5) at 1050 °C applying a heat rate of 8 °C/min. The typical buffer layer thickness ranged between 30 to 50 nm as confirmed by ellipsometry.

Chapter 6

Characterisation techniques

The following chapter gives a short introduction to the various characterisation techniques applied in the present study.

6.1 X-ray diffraction

X-ray diffraction (XRD) was used for characterising the lattice parameter, a, and global texture full width at half maximum (FWHM) values in the recrystallised substrate materials.

Lattice parameter determination

When a monochromatic beam of X-rays (with a wavelength λ) is focused onto a sample with an incident angle θ constructive interference occurs and the X-rays are scattered elastically when Bragg's law is satisfied

$$n\lambda = 2 \cdot d \cdot sin(\theta). \tag{6.1}$$

Note that n is an integer and d is the lattice plane spacing. A schematic example of the diffraction geometry is shown in Fig. 6.1.

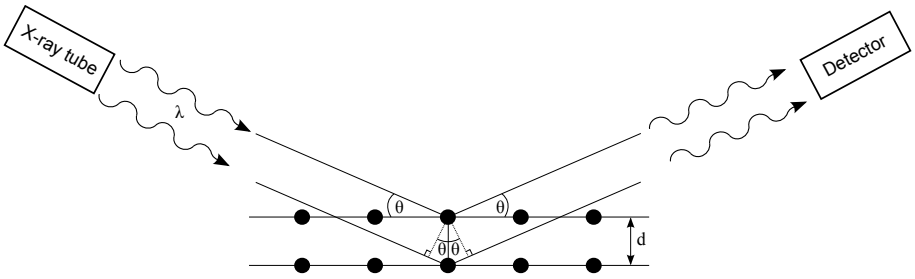

Figure 6.1: Schematic presentation of Bragg diffraction of X-rays by planes of atoms. Reproduced after [86].

$\theta - 2\theta$ scans were conducted on the substrate materials. The XRD system used in this work was equipped with a monochromator and Cu anode which produced $K_{\alpha 1}$ and $K_{\alpha 2}$ radiation, corresponding to X-rays with wavelengths $\lambda_1 = 1.5406$ Å and $\lambda_2 = 1.5444$ Å, respectively. The time per step was 2 seconds and the scan step size was 0.04^o.

The position of the $K_{\alpha 1}$ peak was used for determination of the (200) plane reflection in the Ni-based substrate materials. The lattice parameter was calculated from the relationship between d and a for a cubic system:

$$d = \frac{a}{\sqrt{h^2 + k^+ l^2}} \tag{6.2}$$

where (hkl) corresponds to the Miller indices of the lattice planes.

Texture analysis by X-ray diffraction

Texture can be divided into *in-plane texture* (ϕ) and *out-of-plane texture* (ω) and is discussed further in appendix A. These values are included in section 7.3 in order to compare the new alloys with standard substrates. The in-plane and out-of-plane texture can be evaluated by the FWHM value. Gaussian curves were fitted to the diffraction data in this work and the FWHM values ($\Delta\phi$ and $\Delta\omega$) were calculated from these curves.

A goniometer enabled diffraction conditions of the metal substrates at various rotations and tilts of the sample. ω-scans were performed by rocking the samples around the <200> pole of the Ni-based substrates with a total angular range of about 13^o. Additionally, rocking curves were measured both along the RD and TD directions in the RD-TD plane of the substrates. An in-plane ϕ-scan was performed around the <111> pole of the substrates and the FWHM value is a mean value of the four diffraction peaks.

6.2 Atomic force microscopy

Surface topography was characterised by contact mode atomic force microscopy (AFM). This technique utilises a probe, which is brought into contact with the sample material and then scanned across the sample surface. The probe consists of a cantilever mounted with a silicon tip. The repulsion forces between the tip and the sample surface result in a cantilever deflection of several nm's which is recorded by the laser deflection system. The surface height (z) is thus recorded for each position (x,y) on the surface. An example of the AFM setup is shown in Fig 6.2.

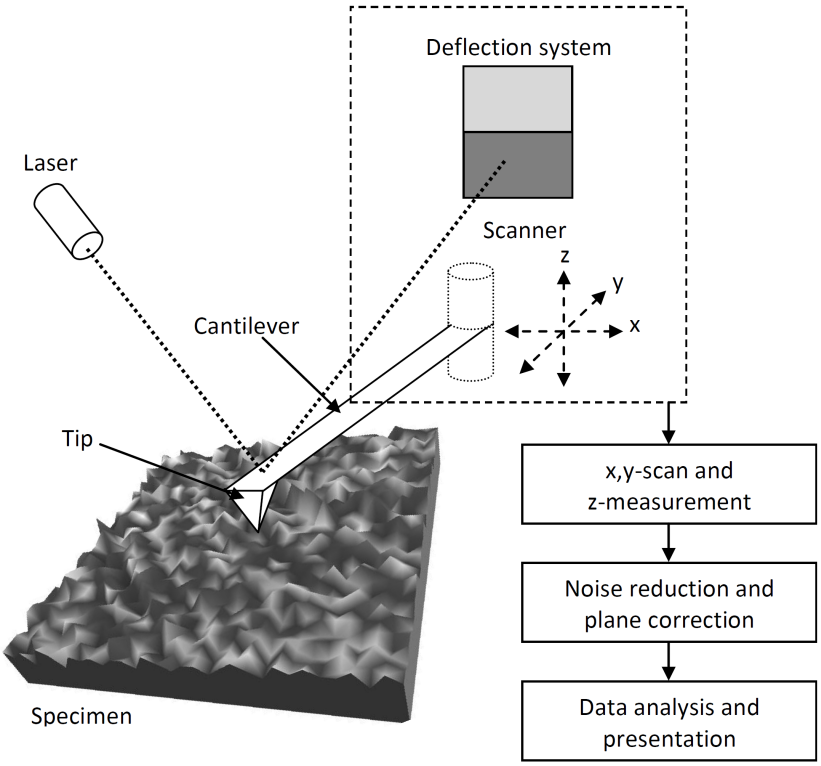

Figure 6.2: Schematic diagram of the AFM setup.

An AFM operated in contact mode utilises the short range repulsive interactions which are important for interatomic distances below 1 nm. The contact is defined as the repulsion forces (typically 10^{-6} to 10^{-8} N) being strong enough to induce deformation on the surface or tip [87]. The material surface must therefore be relatively hard and great care was taken to prevent tip wear and surface damaging during scanning.

The AFM setup used in this work was a Nanosurf Easyscan E-AFM 2 system which had a 16 bit data resolution. The system was equipped with a silicon point-probe-plus tip which had a tip radius of curvature = 10 nm and a spring constant = 0.02-0.07 N/m. A so-called constant deflection mode was applied in the present study since large areas ($\sim$ 50x50 μm^2) could be scanned while minimising surface damage and tip wear.

Note that the spatial resolution was 0.2 nm and the height resolution was 1-2 nm [88]. A step size of 200 nm was applied for all the AFM scans and a specially designed XY-stage enabled a localisation of specific areas of interest on the substrate described in section 7.2.

Image resolution of the current technique is generally limited due to vibrational and thermal noise, tip quality, sample preparation and scan rate. Artefacts and features not representing the topography of the specimen surface were treated and corrected using standard correction tools in the Image Metrology SPIP 6.0.2 software.

The arithmetic surface roughness (S_A) was used to characterise the surface roughness in this work. It is defined as

$$S_A = \frac{1}{MN} \sum_{k=0}^{M-1} \sum_{l=0}^{N-1} |z(x_k, y_l)| \tag{6.3}$$

where M and N are the total number of data points in the x-y grid, and k and l are index numbers.

Grain boundary grooves were characterised by a groove depth and mean dihedral angle, see section 3.3. Each reported groove depth corresponds to an average value of at least three line scans performed perpendicular to the boundary.

6.3 Scanning electron microscopy

A Zeiss Supra 35 field emission gun scanning electron microscope (FEGSEM) was used for microstructural investigations. The SEM technique utilises a focused electron beam which is scanned in order to generate an image of the sample surface. The spatial resolution of this technique is material, beam current and acceleration voltage dependent, and limited to $\sim$ 10 nm in Ni-based materials [89]. Two of the commonly used signals that are generated when an electron beam interacts with a material are the secondary electrons (SE) and the backscattered electrons (BSE). The contrast of SE imaging depends mainly on the sample topography while the contrast in BSE imaging is highly dependent on the atomic number and the crystallographic orientation of the sample. An acceleration voltage of 15 kV was applied for all SEM imaging.

6.4 Electron backscatter diffraction

The Zeiss Supra 35 FEGSEM was equipped with a HKL Technology Channel 5 electron backscatter diffraction (EBSD) detector. The EBSD system was used to obtain statistical texture and microstructural information from the annealed substrates. The principle of the EBSD technique is illustrated in Fig. 6.3.

BSEs are diffracted from a specific area on the surface of the tilted sample. The tilt was 70^o since it increases the fraction of BSEs diffracted towards the detector. The diffracted BSEs generate a so-called Kikuchi diffraction pattern which is automatically analysed in the system

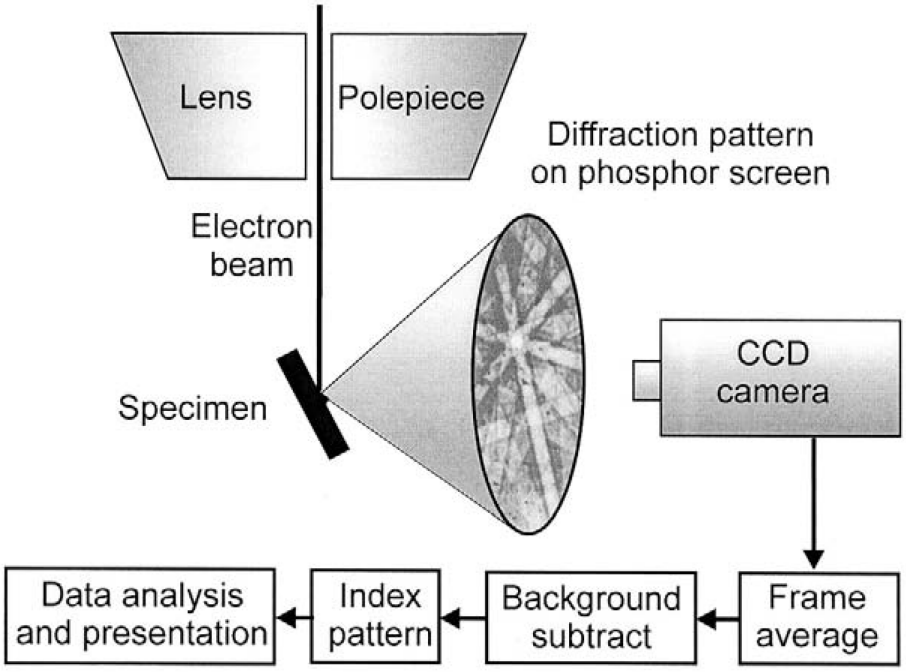

Figure 6.3: Schematic diagram of the EBSD setup [39].

and the crystallographic orientation is determined. Beam scanning was used in this work since this allowed for a more rapid data acquisition compared to stage scanning. The spatial and angular resolution are about 10 nm and 1.5^o, respectively, in this setup when utilising the dynamical focus facility [89,90]. Orientation data is collected in a square grid applying a specific step size and an acceleration voltage of 15 kV was applied for all EBSD mapping. All the EBSD maps reported in this thesis were collected from the substrate surface parallel to the RD-TD plane.

Statistical texture information

Large scans were applied in order to obtain statistical crystallographic texture information of the annealed metal substrates. The scans were typically performed in different regions of the substrate but not closer than 0.5 mm from the substrate edge. A typical map size was 1 mm^2 and generally a total area of more than 5 mm^2 was scanned using a step size of 10 μm. The area fraction of cube texture was generally evaluated considering orientations deviating 5, 10, and 15 ^{o} from the ideal {001}<100> orientation.

Local microtexture and microstructural analysis

Several smaller maps with a typical size of $\sim$0.2 mm^2 was scanned applying a step size of 1-2 μm. Such maps were used for characterising GB distributions, the GB network and grain sizes. The latter was measured using line intersections and calculating the mean value from intersections parallel and perpendicular to the RD direction in the maps.

The index rate in the EBSD maps was generally higher than 90% and the EBSD data was post-processed using the HKL Channel 5 software to remove non-indexed data points. Due to limited angular resolution of the EBSD technique some orientation noise was present in the maps and consequently misorientations below 1.5^o were ignored in the maps.

Stereological parameter length per unit area

Changes in the GB network due to grain growth, and changes in GB distribution, was analysed considering the stereological parameter length per unit area, L_A [91]. This parameter was monitored considering only misorientations above 10^o. L_A is calculated by multiplying the number of misorientations pixels (i.e. pixels constituting a GB) above 10^o with the step size divided by the scan area. A correction is introduced due to the stepped nature of the reconstructed boundaries the EBSD map. Assuming an equal likelihood of all boundary inclinations the corrected value $L_A = \pi L_A^{map}/4$ [91].

6.5 Vibrating sample measurements

The magnetic moment of the substrates was measured in a vibrating sample magnetometer (VSM) in a cryogenic free measurement system. A sketch of the system is shown in Fig 6.4.

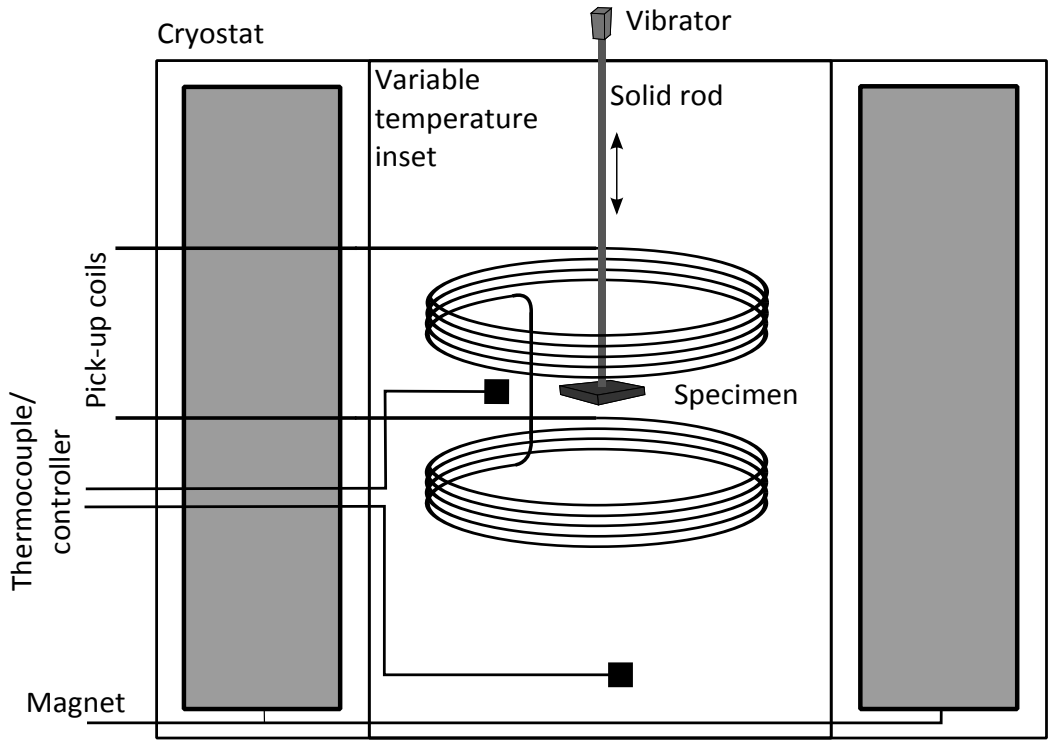

Figure 6.4: Schematic presentation of the VSM setup.

The sample is placed on a solid rod and positioned inside the cryostat. The sample is then mechanically vibrated in a constant magnetic field. This constant field aligns a fraction of the domains in the ferromagnetic sample and a macroscopic magnetic field is generated in the sample when the temperature is below the Curie temperature. This magnetic field, which corresponds to the magnetic moment of the sample, is measured by the pick-up coils. The applied magnetic field was perpendicular to the RD-TD plane of the substrate and the vibration frequency was 20.4 Hz.

The temperature dependence of the magnetic moment was measured by applying a constant magnetic field $\mu_0 H = 50$ mT and by ramping the temperature from 5 to 325 K and down to 5 K again with a rate of 2 K/min.

Magnetic hysteresis was recorded at 75 K by ramping the field from zero to 1 T, then to -1 T and back to 1 T. The field was ramped with 0.5 T/min.

6.6 Vickers hardness measurements

Vickers microhardness tests were applied in the present study for characterising the hardness of the recrystallised substrate materials. The hardness generally scales linearly with the tensile strength of metals [92] and is used in this study to estimate changes in the mechanical properties of the substrates. The Vickers microhardness is measured by pressing a diamond tip, shaped as a pyramid, into the material surface. A schematic example of the test is shown in Fig. 6.5(a) and the resulting indentation is drawn in Fig. 6.5(b).

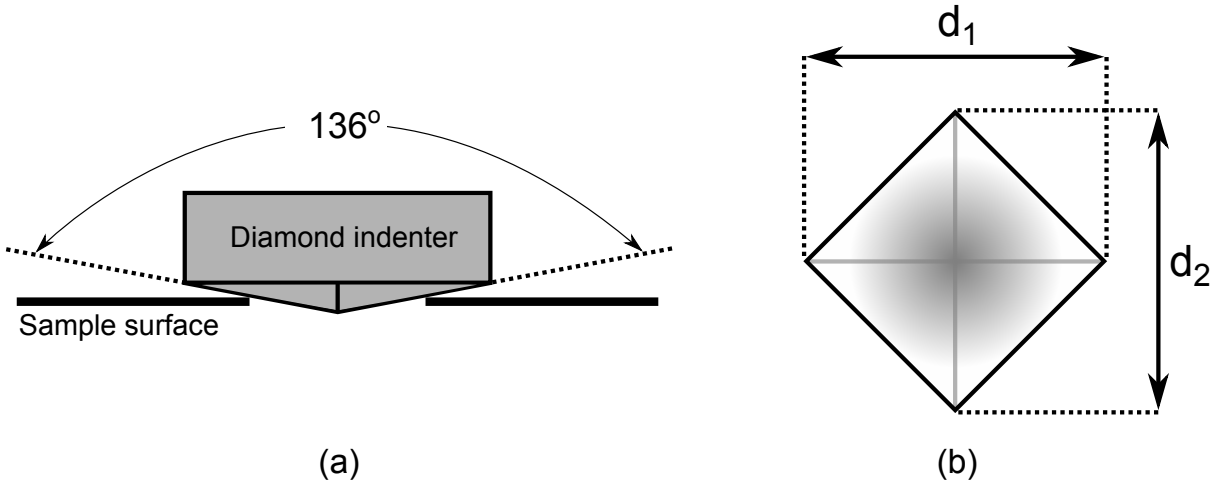

Figure 6.5: (a) sketch of the Vickers hardness test and (b) a schematic example of an indentation mark (b).

The Vickers microhardness can be calculated from the mean value (d) of the two diagonals of the indentation as $HV = 1.854 \cdot L/d^2$, where L (kg) is the load. A Struers Durascan Hardness tester was used applying a load L = 200 g for 15 seconds on the RD-TD plane of the annealed substrates. A multiple number of indentations were performed in random places on the substrate with a distance of at least three times d between the indentations. The hardness values presented in the thesis are mean values and the standard error was ∼0.33 HV.

6.7 X-ray fluorescence spectroscopy

Chemical compositions were analysed using X-ray fluorescence (XRF) spectroscopy. The technique utilises X-rays that are focused onto the sample surface. This irradiation generates so-called secondary X-rays which are emitted from the irradiated material volume. The corresponding wavelengths of these emitted X-rays are characteristic for the elements in the material.

An ARL 9400 XP sequential WD-XRF spectrometer was used in this work. The obtained data was post-processed using the Uniquant 4 software and the experimental errors for this technique were 0.5, 0.1 and 0.2 at% for Ni, Cu and W, respectively.

Part III

Results, Discussion and Conclusions

Chapter 7

Results and discussion

This chapter presents the experimental results of the thesis which include results from Ref. A1-4 and additional results not published elsewhere. Section 7.1 and 7.2 describe results relevant to production of long RABiTS-based coated conductors in general while the results presented in section 7.3 are mainly related to optimisation of substrates for CCs utilised in AC applications.

7.1 Effect of initial Ni-5at.%W substrate surface quality

This work was motivated by research hypothesis 1 described in section 4.4. The experimental details of the Ni-5at.%W substrates and buffer layer are described in chapter 5 while the applied characterisation techniques are described in chapter 6.

7.1.1 Surface roughness analysis

A series of Ni-5at.%W tapes were mechanically polished after cold-rolling but before the re-crystallisation annealing heat treatment. The mean surface roughness was analysed before the annealing, and both roughness values and statistical texture information were obtained after annealing using AFM and the EBSD technique. The recrystallised substrates were dip coated with a $Gd_2Zr_2O_7$ buffer layer and crystallised to investigate the effect of substrate roughness on the buffer layer. Fig. 7.1 shows the surface roughness as a function of polishing diamond grain size (DGS).

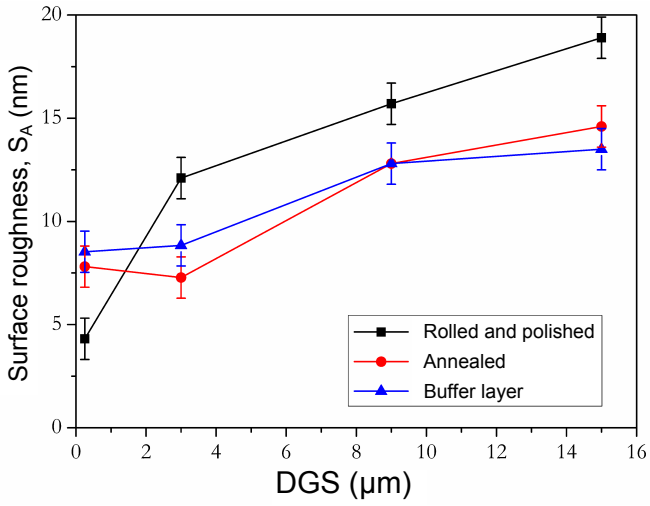

Figure 7.1: Mean surface roughness (S_A) as function of polishing grade for the different tape conditions.

The error bars in Fig. 7.1 correspond to the measurement height uncertainty of the AFM technique. Note that the mean surface roughness value (S_A) reported in this work includes GBs and that samples are referred to according to the DGS grade.

Interestingly, the surface roughness seems to be a linear function of the polishing grade for DGS = 3 to 15 μm, see Fig. 7.1, except for a significant decrease to $\sim$ 4 nm for the sample polished with DGS = 0.25 μm. The high mean surface roughness value of the samples polished with high DGS grades is mainly due to scratches produced during mechanical polishing. Such scratches are clearly apparent in the corresponding SEM micrographs of the sample polished with DGS = 15 μm, see (1) in Fig. 7.2(a). Additionally, GB grooving is also apparent at (2) in Fig. 7.2(a). The general decrease in surface roughness of the samples with DGS = 3 to 15 μm after annealing is caused by a flattening effect which is effectively reducing the roughness by surface diffusion of the scratches [93].

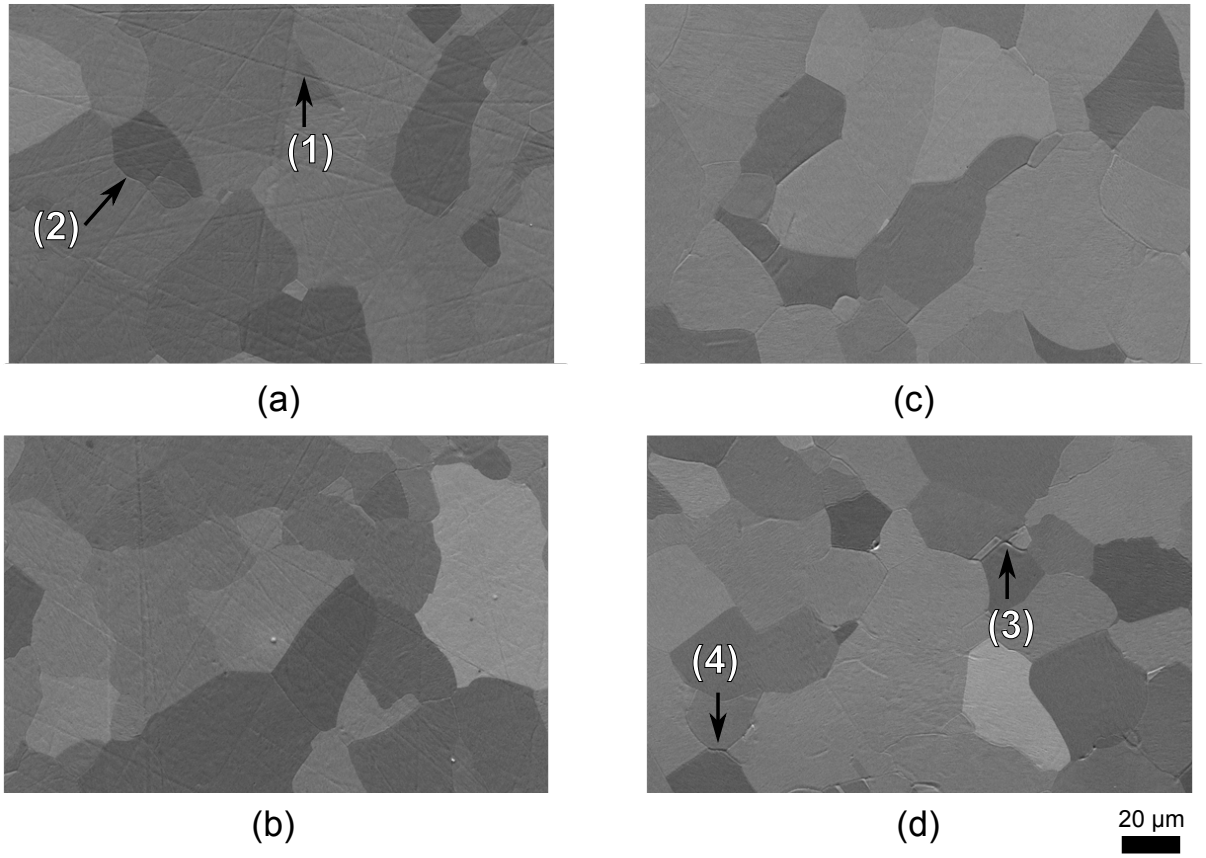

Figure 7.2: SEM micrographs of the polished and annealed Ni-5at.%W substrates. (a) DGS = 15 μm, (b) DGS = 9 μm, (c) DGS = 3 μm and (d) DGS = 0.25 μm.

In contrast, the surface roughness increases to $\sim$ 8 nm after annealing of the very fine polished sample with DGS = 0.25 μm as shown in Fig. 7.1. Trunchan et al. [49] observed a similar increase of the surface roughness after annealing compared to the cold-rolled condition. They explained the roughness increase as a result of considerable GB grooving. Such grooves are clearly the dominating surface defect when evaluating the SEM micrographs in Fig. 7.2(c) and (d). Furthermore, some boundaries seems to develop deeper grooves, see (3) and (4) in Fig. 7.2(d), compared to other GBs. Such groove depth differences between different boundary types have been observed previously in strongly textured Ni-Cr substrates [48]. A study of such correlations in Ni-5at.%W substrates is included in section 7.2.

It is evident that smoothing of scratches is effectively reducing the surface roughness of the

samples polished with high DGS grades. However, this effect is no longer counterbalancing the surface roughening due to GB grooving in the sample polished with the finer DGS grade. Note that the intra-grain surface roughness, i.e. not including GBs, of the annealed Ni-5at.%W substrates was below 5 nm for both the DGS = 0.25 and the 3 μm samples. Furthermore, the surface roughness including GBs was similar for these two samples after annealing. It is therefore apparent that the very finest polishing is not further improving the surface quality since GB grooving will increase the S_A value to the same level as for the sample polished with DGS = 3 μm. An example AFM image of the sample polished with DGS = 0.25 μm after annealing is shown in Fig. 7.3(a).

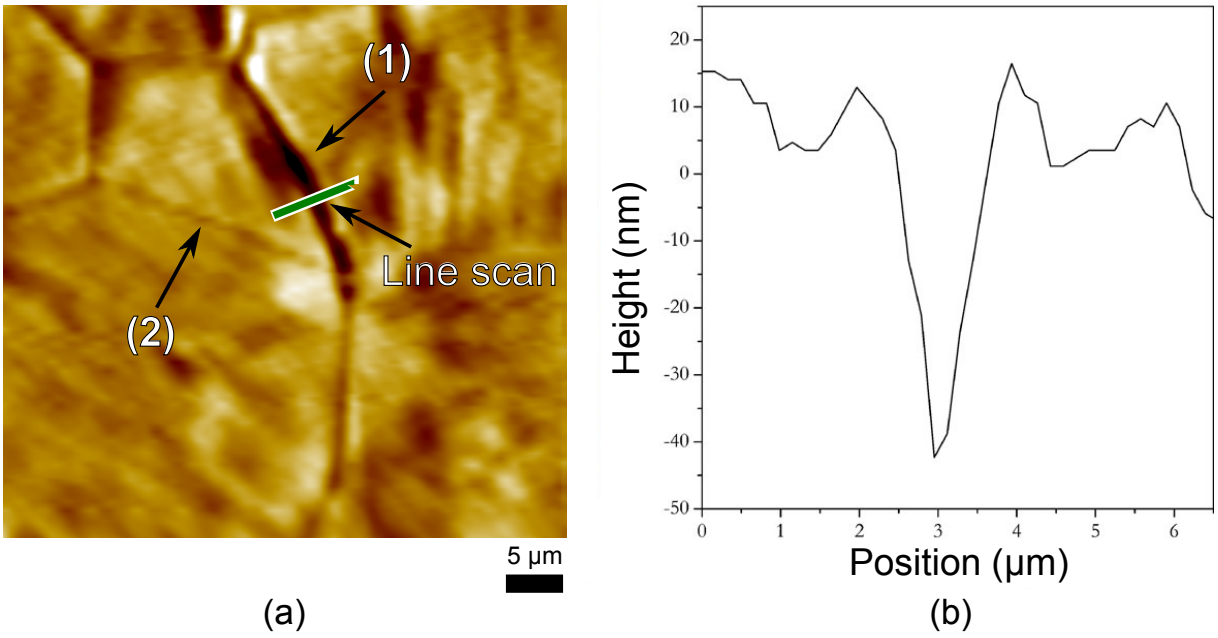

Figure 7.3: (a) AFM image of the annealed DGS = 0.25 μm substrate and (b) line scan profile of the position indicated in (a).

The dark areas in Fig. 7.3(a) correspond to small height values and the GB groove is clearly deeper at (1) compared to the groove at (2). These grooves are observed to impose a lower limit for the mean surface roughness $\sim$ 8 nm for the Ni-5at.%W substrates annealed at 1020 ^{o}C for 75 min. Multiple boundary grooves were identified and analysed in the AFM images. Note that no distinction was made between different types of boundaries and more than three line scans were performed perpendicular to each GB. An example line scan profile from Fig. 7.3(a) is shown in Fig. 7.3(b). The groove depth ranged between 15 nm and 59 nm and is comparable to the values obtained on commercial Ni-5at.%W substrates [53].

The buffer layer surface roughness generally increased slightly for low DGS grades and a small decrease was apparent for the sample with DGS = 15 μm. An increase may be explained by the further grooving of the GBs in the Ni-5at.%W substrate due to the additional annealing at an increased temperature (1050 ^{o}C). The small decrease of the sample with DGS = 15 μm may be explained by an effective filling of buffer layer material into the scratches on the tape surface. Interestingly, scratches in the DGS = 15 μm sample were typically characterised by a broader line scan profile (2-6 μm) compared to the GB grooves investigated in the finest polished sample which was generally characterised by a width $\sim$ 1-3 μm. Accordingly, the extent of buffer material filling may therefore be related to the width of a surface defect.

7.1.2 Texture analysis

All the Ni-5at.%W substrates were characterised by a strong cube texture after the recrystallisation annealing. Fig. 7.4 shows part of a larger EBSD map and the {111} pole figure of the sample polished with DGS = 0.25 μm.

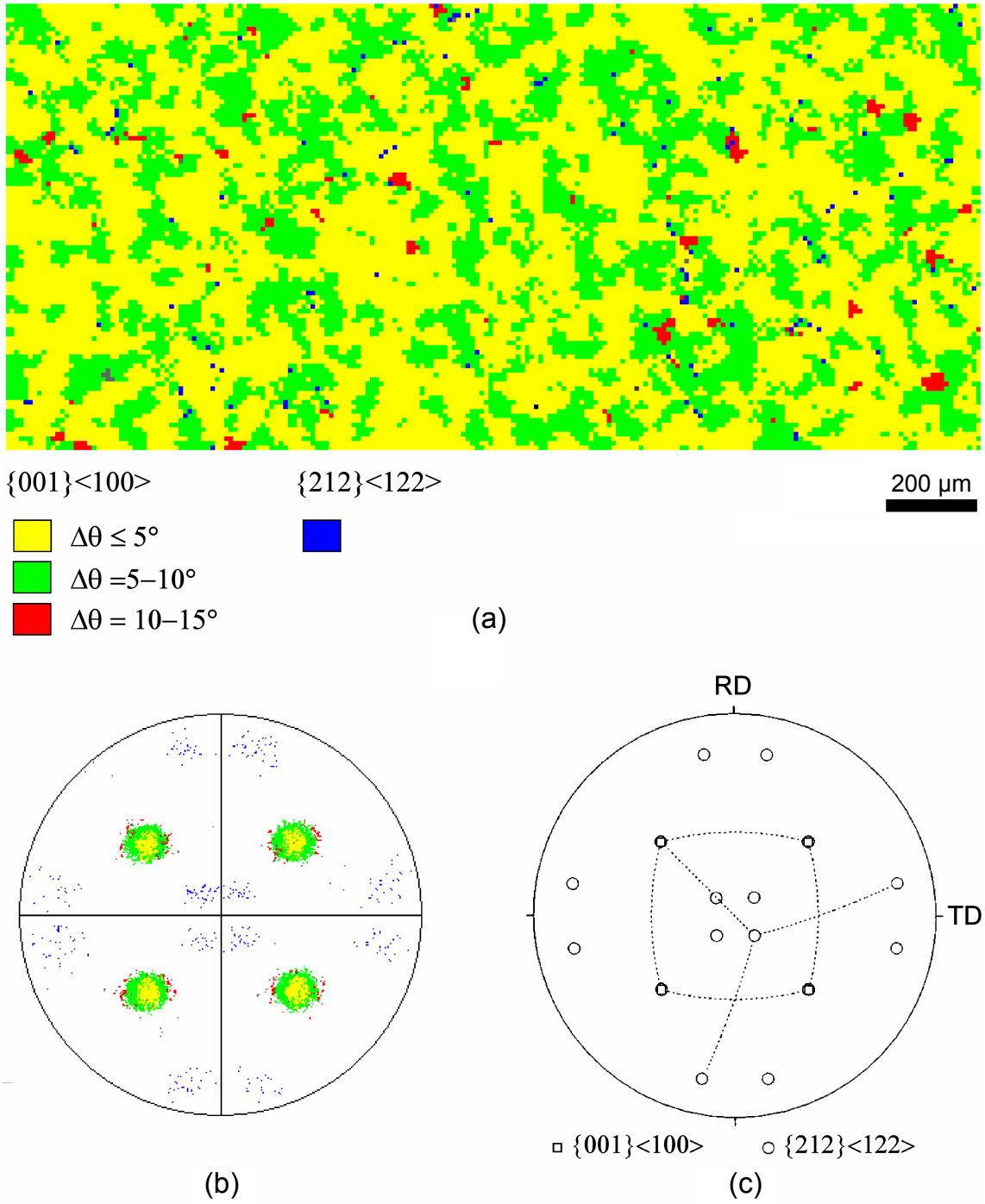

Figure 7.4: Statistical texture information for the sample polished with DGS = 0.25 μm. (a) part of a larger EBSD map where $\Delta\phi$ is the deviation from the ideal {001}<100> orientation, (b) {111} pole figure from the same region displayed in (a) and (c) the positions of the ideal orientation component of the cube and twin-to-cube orientation in the pole figure in (b).

Colors in the map represent the deviation angles ($\Delta\theta$) from ideal cube {001}<100> orientation. It is evident that a major part of the area ($\sim$ 60%) is characterised by grains with $\Delta\theta \leq 5^o$ from the ideal cube orientation. However, some twin-to-cube {212}<122> orientated grains (blue pixels) are also observed in the EBSD map and the pole figure in Fig. 7.4(a) and (b), respectively. The ideal positions of the {001}<100> and {212}<122> orientations are shown in Fig. 7.4(c). It is significant that the total area fraction of cube texture amounts to more than 96 % for $\Delta\theta \leq 10^o$ and that the area fraction of twins is lower than 1 %. Accordingly, this results in a fraction (f) of more than 99% of cube texture within a deviation angle of 15^o.

Fractions of cube texture within deviations of 5, 10 and 15^o are shown as function of the DGS grade in Fig. 7.5.

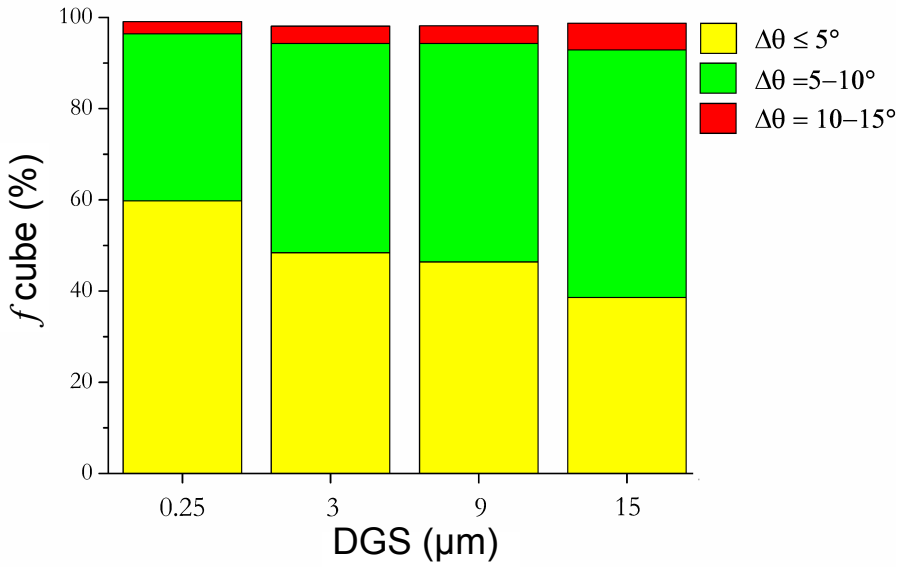

Figure 7.5: Area fraction of cube texture for the annealed Ni-5at.%W tapes as a function of DGS grade.

The fraction of cube texture within 10 and 15^o is clearly not as sensitive to the DGS grade as the fractions below 5^o. For example, the change in f is less than 4 % between the samples with DGS = 0.25 and 15 μm for $\Delta\theta \leq 10$ and 15^o. In contrast, a much greater difference is observed within a deviation of 5^o where the fraction of cube texture decreases by 21 % for the same two samples. This clearly demonstrates an effect of the surface roughness in the cold-rolled condition of the metal substrate on the strength of the cube texture after the recrystallisation annealing. Furthermore, f is particularly sensitive to the DGS grade for low deviation angles. Note that the fraction of twin related orientations increases only slightly from 0.9 to 1.3 %. The fraction of cube texture within a deviation of 15^o is however still above 98 % for all the samples with different DGS grades.

Local deformations such as scratches are known to affect the recrystallisation process in close vicinity of the scratch [94]. It may therefore be suggested that the successful range of recrystallisation nuclei resulting in cube orientated grains is affected by an increase in the DGS grade.

7.1.3 Summary

Ni-5at.%W tapes where polished, annealed and finally coated with a $Gd_2Zr_2O_7$ buffer layer. It was observed that the recrystallisation annealing heat treatment generally decreased the surface roughness compared to polished condition after cold-rolling. However, GB grooves formed during

the annealing in the Ni-5at.%W substrate was found to impose a lower limit ∼8 nm for the mean surface roughness. The surface roughness of the buffer layer generally increased slightly for the fine polished substrates while a small decrease in roughness was observed for the coarser polished samples.

Furthermore, it was demonstrated that the fraction of cube texture within a deviation angle of 5^o from the ideal {001}<100> orientation was very sensitive to the DGS grade of the mechanical polishing after cold-rolling. In contrast, it was observed the fraction of cube texture for deviation angles $\leq$ 10 and 15^o were not appreciably affected by the different DGS grades applied.

7.2 Substrate changes during additional annealing

This work was motivated by research hypothesis 2 described in section 4.4. The preparation details of the initial Ni-5at.%W substrate are described in chapter 5 and the applied characterisation techniques are described in chapter 6.

7.2.1 Recrystallised condition A1

Four marks was made on the Ni-5at.%W substrate using a Vickers hardness indenter, after the recrystallisation annealing at 1000 ^{o}c for 2 hours (condition A1). A SEM micrograph of the enclosed area and the indent marks is shown in Fig. 7.6.

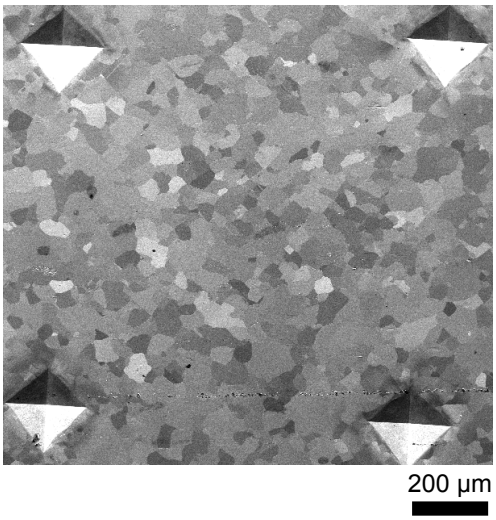

Figure 7.6: SEM micrograph of the recrystallised Ni-5at.%W substrate with indent marks.

Several small areas, which contained different boundary types, were chosen on basis of an EBSD map of the large area. These areas were analysed in detail using high quality SEM micrographs, fine step size EBSD maps and AFM topographic scans. The reference marks enabled a repeated localisation of the same areas. The substrate was accordingly investigated both in condition A1 and after an additional heat treatment at 1025 ^{o}C for one hour (condition A2) which was a higher temperature compared to the initial recrystallisation annealing temperature.

Texture and microstructural analysis

A very strong cube texture was apparent in condition A1 and the area fraction of cube texture was 96 % within a deviation angle of 10^o from the ideal {001}<100> orientation. The remaining fraction of the microstructure was occupied by grains with a twin-to-cube {212}<122> orientation (see Fig. 7.7(a)) and grains with slightly larger deviations than 10^o from the ideal cube orientation. For clarity, ideal positions of the {001}<100> and {212}<122> orientations are again shown in Fig. 7.7(b). The obtained fraction of cube texture for $\Delta\theta \leq 10^o$ is slightly lower than the values for Ni-5at.%W substrates reported by Eickemeyer et al. [40, 98] but similar to the fraction obtained by Chen et al. [95]. However, the very high fractions of cube texture described in Ref. [40, 98] was either obtained after applying extremely high total thickness reductions or using an intermediate annealing treatment. In contrast, the substrates produced in this work was prepared using a smaller total thickness reduction (TTR) value and without an intermediate annealing treatment.

The fraction of LAGBs in the EBSD maps was 68 % while the remaining part of the GB network was occupied by HAGBs and Σ3 boundaries. Interestingly, even though the fraction of

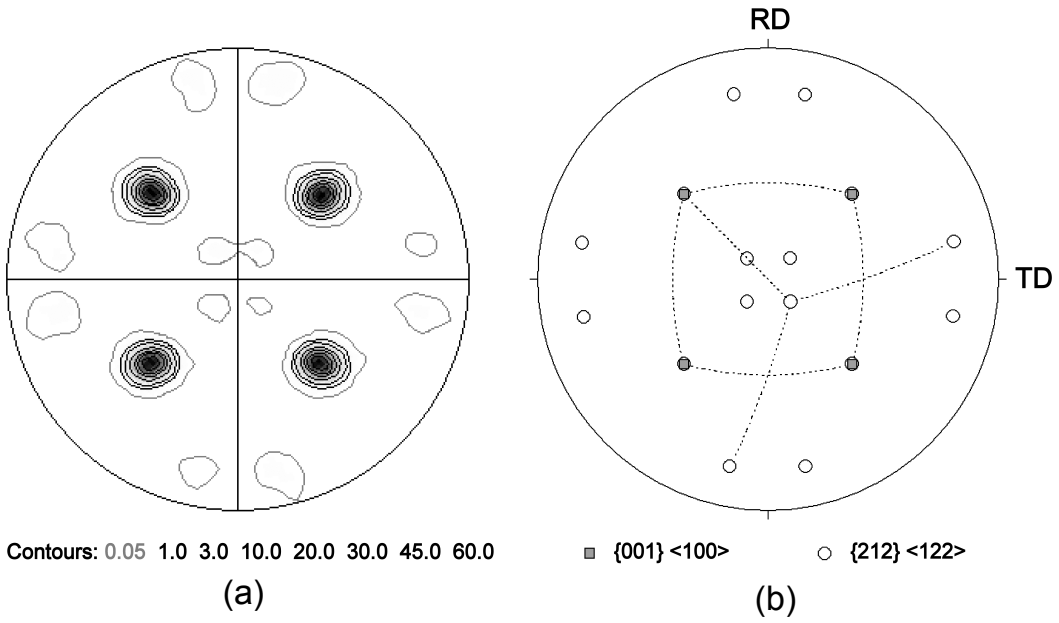

Figure 7.7: (a) {111} pole figure of the Ni-5at.%W substrate in condition A1 and (b) schematic pole figure showing the exact positions of the ideal {001}<100> and {212}<122> orientations.

{212}<122> orientations was very low, Σ3 boundaries still constituted 14 % of the fraction of GBs. This may be explained by the GB morphology of the twin boundaries which comprised 10 % of the GB network. Note that a distinction was made between different types of Σ3 boundaries (see appendix A) according to Ref. 96 and 97. An example SEM micrograph and corresponding EBSD map of an area including both LAGBs, general HAGBs, true twins and non-twin Σ3 (NTΣ3) boundaries are shown in Fig. 7.8.

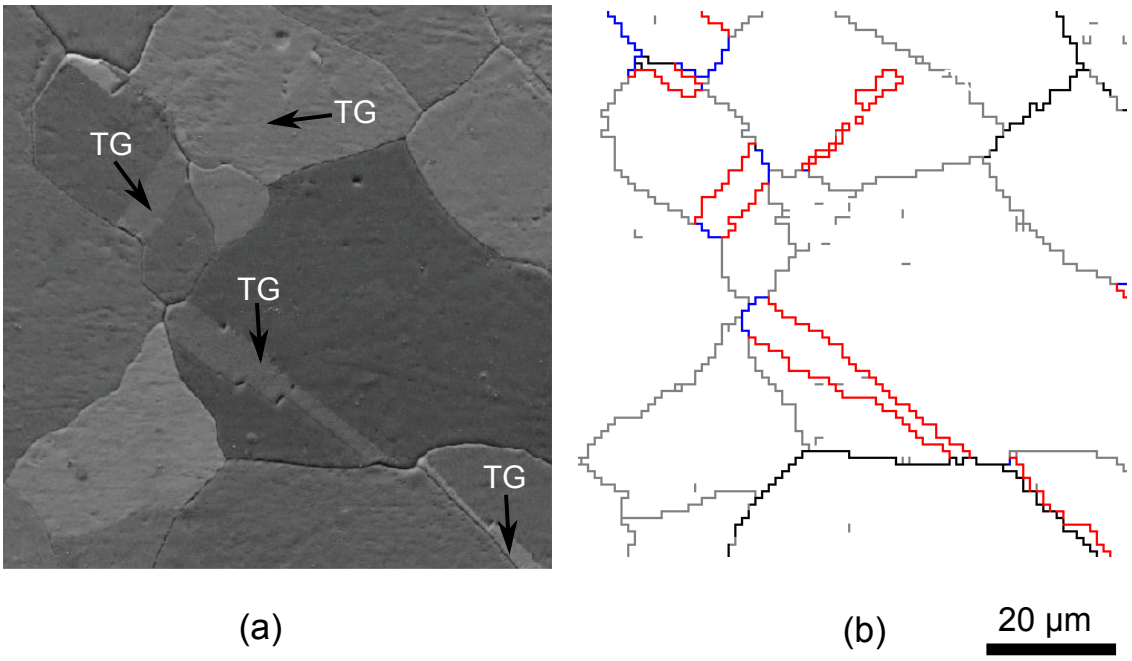

Figure 7.8: Different boundary types in the microstructure in condition A1. (a) SEM image and (b) EBSD map from the same region. LAGBS, HAGBs, TBs and NTΣ3 boundaries are drawn with grey, black, red and blue lines, respectively.

Fig. 7.8(a) demonstrates that twin grains (TG) are usually very narrow, but extended and contains multiple facets along the twin boundaries which results in the significant total fraction of Σ3 boundaries in the corresponding EBSD map as shown in Fig. 7.8(b). Note that the grain size in condition A1 was 25 μm including twins. The microhardness was measured to be 142 HV, which is similar to values reported by other groups [99,100].

Topographic analysis

The topography was analysed by AFM scanning of areas corresponding to more than 17000 μm^2 and the mean surface roughness was 10.7 nm in condition A1.
An example AFM scan of the centre area shown in Fig. 7.8 is presented in Fig. 7.9(a).

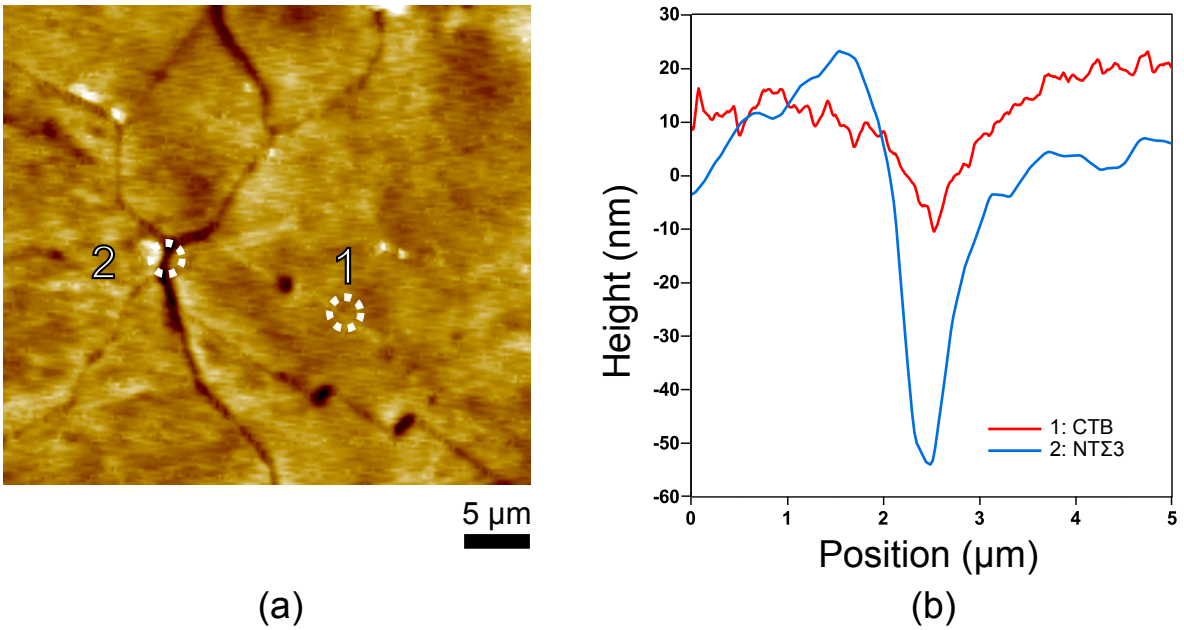

Figure 7.9: (a) AFM scan of the centre of the area shown in Fig. 7.8 and (b) line scan profiles across the boundaries marked with 1 and 2 in (a).

Line scans across the boundaries marked with 1 (CTB) and 2 (NTΣ3) in Fig. 7.9(a) are shown in Fig. 7.9(b). The groove at the NTΣ3 boundary is much deeper than the groove at the CTB, which reflects their different energies [50].

In total 72 boundaries were categorised according to their misorientation angle in the EBSD maps while the groove depth and inclination angles were recorded using AFM scans. It was generally observed that the average groove depths for HAGBs, NTΣ3 boundaries and incoherent twin boundaries (ITBs) were larger than depths recorded for LAGBs and CTBs, see Fig. 7.10.

This is in contrast to the results reported by Gladstone et al.[48] on Ni-Cr substrates observed a very broad range of groove depths for Σ3 boundaries. Importantly, no distinction was made between different Σ3 boundary types in [48] and the broad range of grooves at Σ3 GBs in their work could therefore attributed to a mixing of different types of Σ3 boundaries. Categorising Σ3 boundaries according to Brandon's criteria[1][101] is particularly misleading in this material when considering the extent of GB grooving of the different Σ3 boundary types. Both NTΣ3 boundaries and ITBs developed significantly deeper grooves while CTBs were characterised by the most shallow grooves. It is therefore important to distinguish between the different types of

[1]See appendix A.

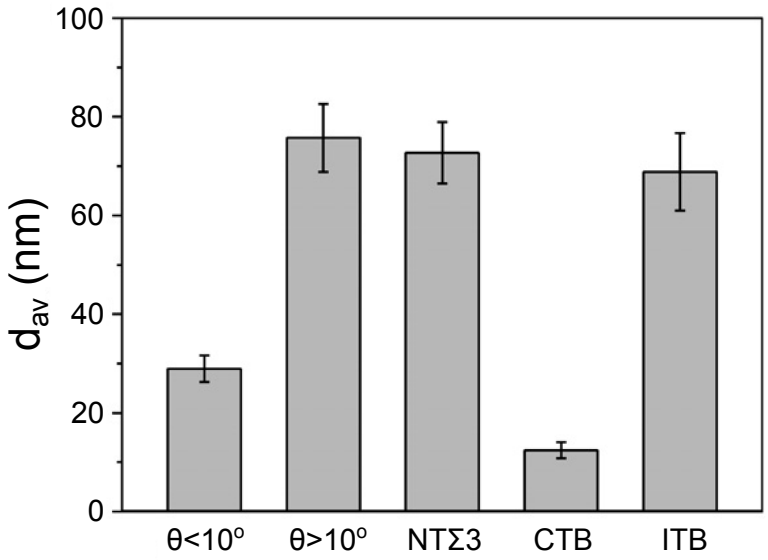

Figure 7.10: Average groove depths. Note that the HAGBs does not include Σ3 boundaries.

boundaries, and in particular the Σ3 boundaries, in order to give an appropriate description of the GB grooving as function of the misorientation angle.

Average inclination angles (β_{av}) of the GB grooves were also considered for the 72 boundaries in condition A1. A trend similar to that for the average groove depths is apparent as shown in Fig. 7.11.

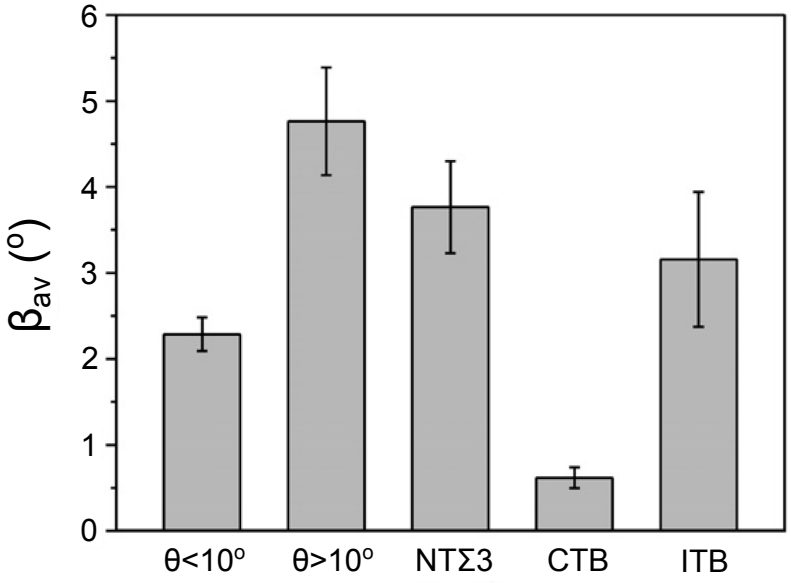

Figure 7.11: Average groove inclination angles. Note that the HAGBs does not include Σ3 boundaries.

It was found that the LAGBs and CTBs developed a more narrow groove compared with the grooves at HAGBs and NTΣ3 boundaries. The average groove width for all boundary types was between 1 to 2 μm in condition A1.

7.2.2 Additionally annealed condition A2

Texture and microstructural changes

The additional annealing simulating a buffer layer crystallisation heat treatment resulted in an increase in the average grain size (GS) from 25 to 28 μm including twins. Migration of boundaries with small misorientation angles and CTBs are generally restricted, while GBs characterised by large misorientation angles may migrate over significant distances resulting in grain growth. Note that the increased grain size did not affect the hardness as shown in Table 7.1.

Condition	$f_{cube(\Delta\theta\leq 10^o)}$	f_{LAGB}	f_{HAGB}	f_{TB}	$f_{NT\Sigma 3}$	$L_{A(\theta>10^o)}(\mu m^{-1})$	GS (μm)	Hardness (HV)	S_A (nm)
A1	96	68	18	10	4	2.0×10^{-2}	25	142	10.7
A2	97	72	17	7	4	1.5×10^{-2}	28	142	10.3

Table 7.1: Parameters describing the texture, microstructure, topography and hardness in condition A1 and A2.

Grain growth in the presence of a strong cube texture effectively reduces to area of grains with orientations significantly different from the ideal {001}<100> orientation. Accordingly, both the fraction of cube texture for $\Delta\theta \leq 10^o$ (see Table 7.1) and the fraction of LAGBs increased slightly after the additional annealing as shown in Fig. 7.12.

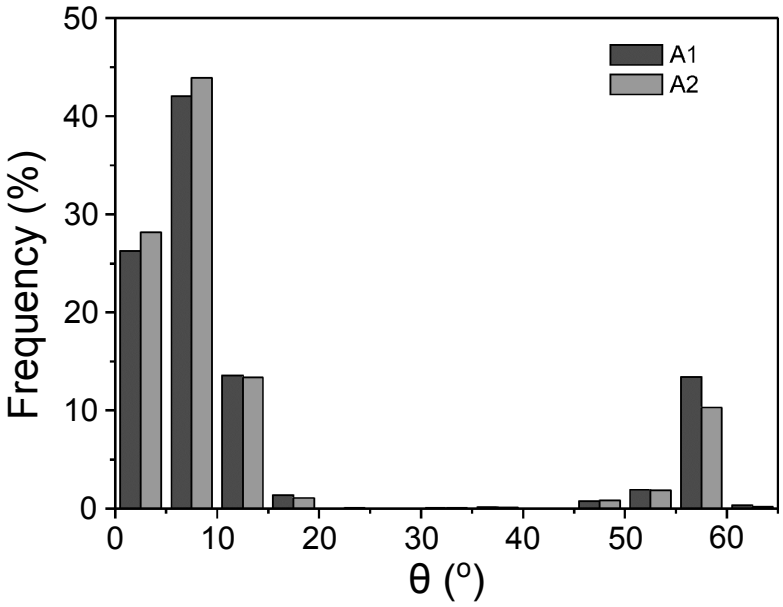

Figure 7.12: Distribution of misorientation angles in condition A1 and A2.

Note that the fraction of general HAGBs decreased only slightly while the fraction of TBs, represented by misorientation angles very close to 60^o in Fig. 7.12, decreased by 3 % in condition A2. Changes due to grain growth and changes in the overall GB network were also analysed considering the boundary trace per unit area, L_A for misorientations with $\theta \geq 10^o$. It was observed that L_A decreased from 2.0×10^{-2} in condition A1 to 1.5×10^{-2} in condition A2 which can be attributed to the grain growth in the presence of a strong cube texture. It is therefore suggested that the additional heat treatment at 1025 ^{o}C would not have a detrimental effect on the substrate texture and GB network. On the contrary, the fraction of LAGBs increases in condition A2 and the boundary area able to reduce J_C is therefore reduced compared to condition A1.

Boundary migration and topographic changes

EBSD boundary maps with a step size of 1 μm and high quality SEM micrographs were used for boundary migration analyses. 24 out of 72 boundaries were classified as migrating boundaries after the additional annealing. An example of a EBSD boundary map is shown in Fig. 7.13.

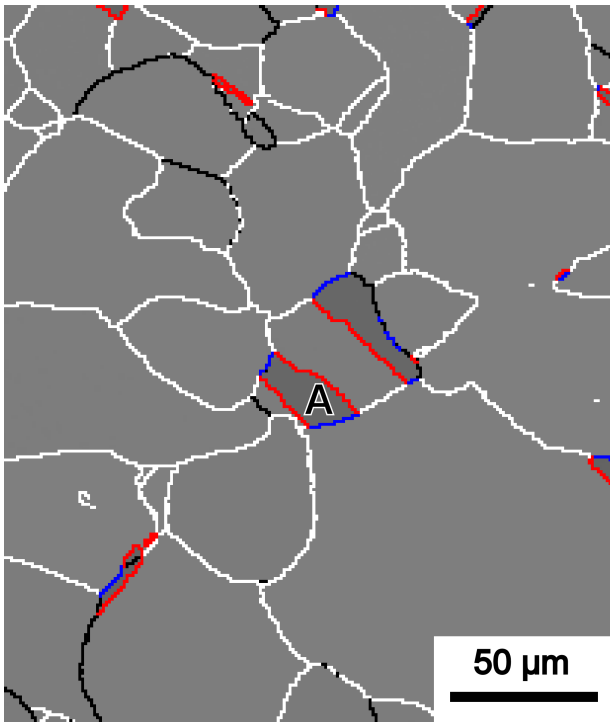

Figure 7.13: EBSD boundary map. LAGBs and general HAGBs are drawn with white and black lines, respectively. Red lines correspond to TBs and blue lines show NTΣ3 boundaries. The letter A is a reference label (see Fig. 7.14(a)).

It was further observed that migrating boundaries left a groove behind after migrating to a new position. Example SEM micrographs which demonstrates such migration are shown in Fig. 7.14.

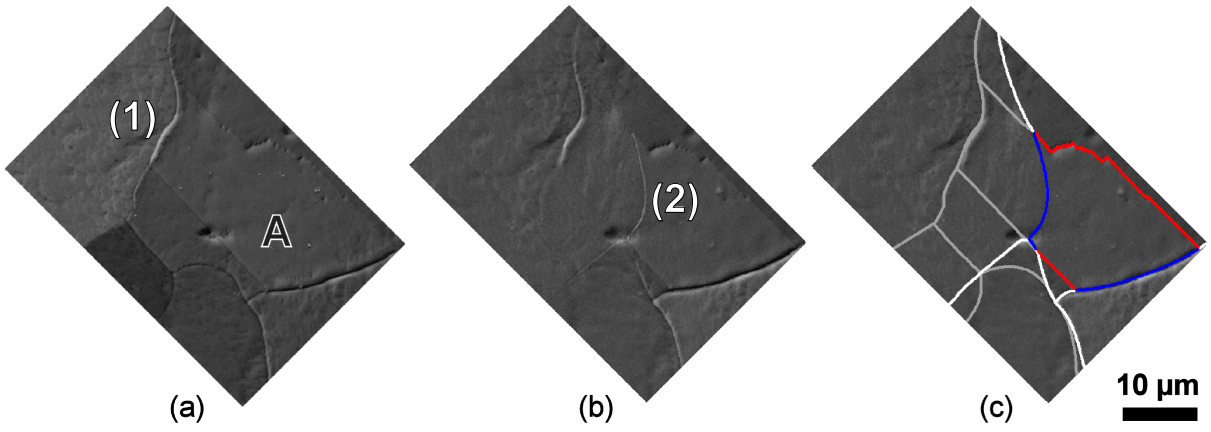

Figure 7.14: SEM micrographs of the area shown in Fig. 7.13. The microstructure in condition A1 (a) and in condition A2 (b). The letter A is a reference label, see Fig. 7.13. (c) shows the microstructure from (b) with GBs drawn for clarity. LAGBs, TBs and NTΣ3 boundaries are drawn with white, red and blue lines, respectively. Grey lines are boundary positions in condition A1.

The NTΣ3 boundary at (1) migrates from its original position in condition A1, see Fig. 7.14(a), to position (2) as shown in Fig. 7.14(b). The boundaries are drawn with different colours according to the boundary type, see caption in Fig. 7.13. The grey lines indicate the boundary positions in condition A1.

Depths of the all the analysed GB grooves as a function of misorientation angle in condition A1 and A2 are shown in Fig. 7.15 and Fig. 7.15, respectively.

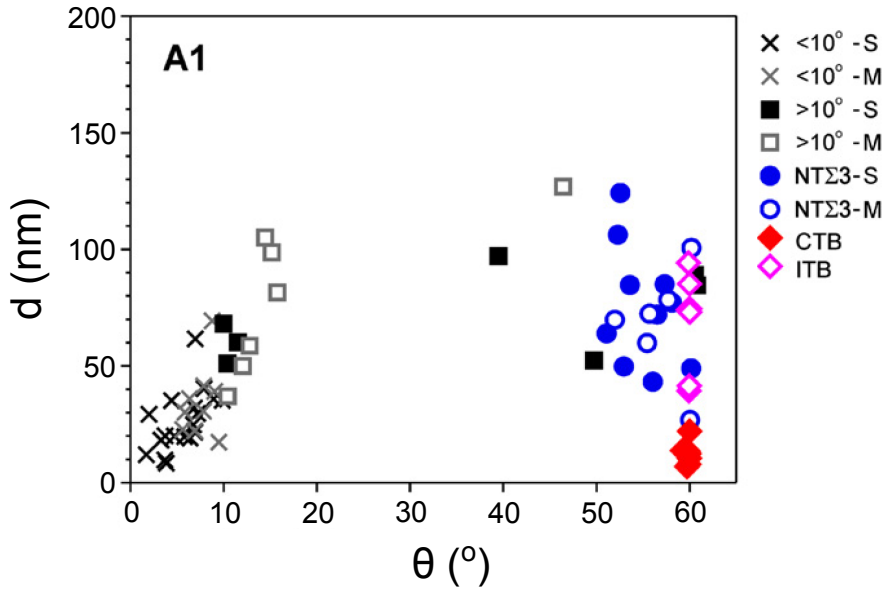

Figure 7.15: Groove depths of the boundary grooves in condition A1. The letters S and M in the legend refer to stationary and migrating boundaries, respectively. No distinction is made between stationary and migrating ITBs.

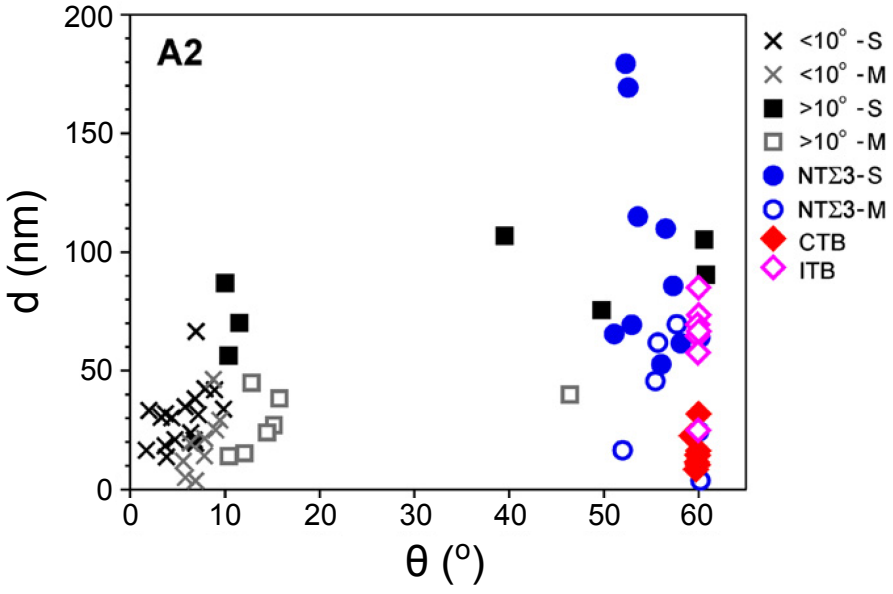

Figure 7.16: Groove depths of the boundary grooves in condition A2. The letters S and M in the legend refer to stationary and migrating boundaries, respectively. No distinction is made between stationary and migrating ITBs.

Differences are clearly apparent between the depths of the grooves in condition A1 and A2.

The depth of stationary grooves is increased in condition A2 compared to the depth in condition A1. In contrast, the depth of the groove decreases for the mobile boundaries as seen in Fig. 7.15 and Fig. 7.16.

These changes are more evident when considering the groove depth differences ($\Delta d = d_{A2}$-d_{A1}) for the individual grooves. Fig. 7.17 shows (Δd) as a function of misorientation angles for the stationary boundaries.

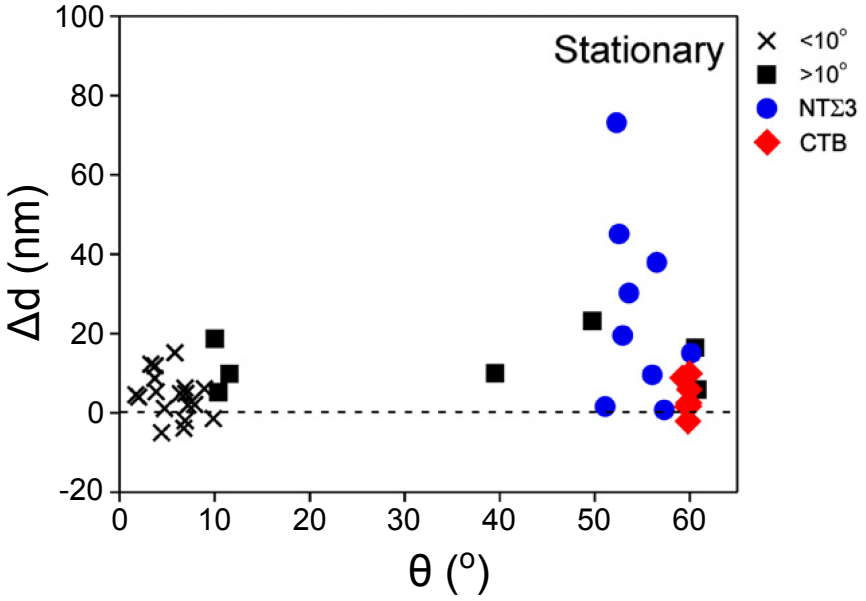

Figure 7.17: Groove depth differences ($\Delta d = d_{A2}$-d_{A1}) between condition A1 and A2 at stationary boundaries.

Groove depth differences for the migrating boundaries are shown in Fig. 7.18.

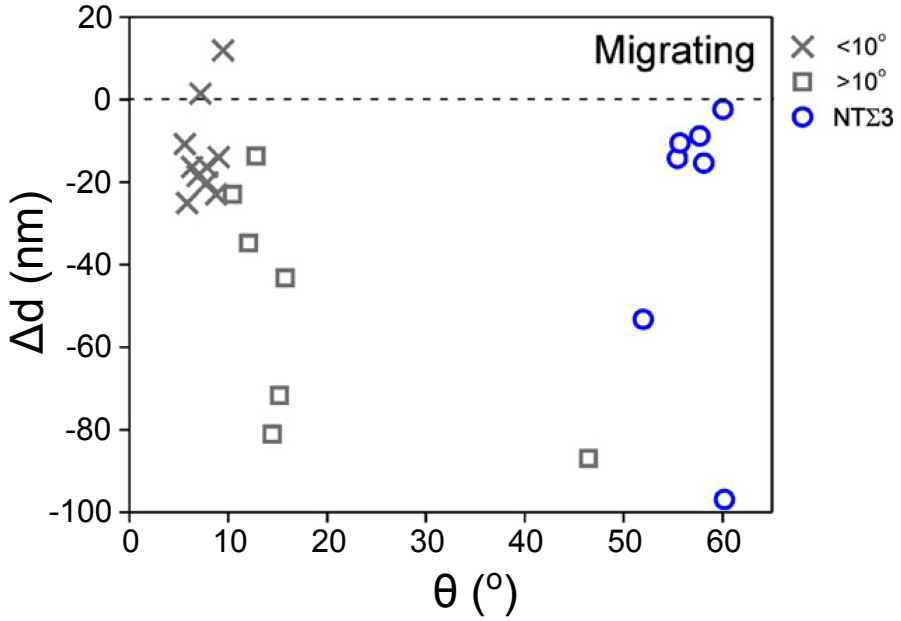

Figure 7.18: Groove depth differences ($\Delta d = d_{A2}$-d_{A1}) between condition A1 and A2 at migrating boundaries.

Grooves at stationary boundaries were further developed and the depth of these grooves increased. The greatest increase in groove depth was observed for boundaries with large misorientations angles, except for CTBs. Grooves at low misorientation angles were less developed. The groove depth for a small number of boundaries classified as stationary was unexpectedly observed to decrease after the additional annealing by 1-5 nm, see Fig. 7.17. This may be due to the positions where grooves were analysed before and after the additional annealing were not identical.

A general decrease was observed in the depth of the migrating boundaries and it was apparently independent of the misorientation angle. The decrease in depth is related to the shorter time for developing a deep groove and the grooves therefore became shallower after the additional annealing. Note that grooves at two migrating LAGBs were unexpectedly observed to increase (see Fig. 7.18) though these boundaries were clearly migrating. A possible explanation for this is that these boundaries have migrated in the start of the additional annealing and they therefore have had longer time to develop a deeper grove.

Average groove depth values for the stationary and migrating boundaries are shown in Fig. 7.19 and Fig. 7.20, respectively.

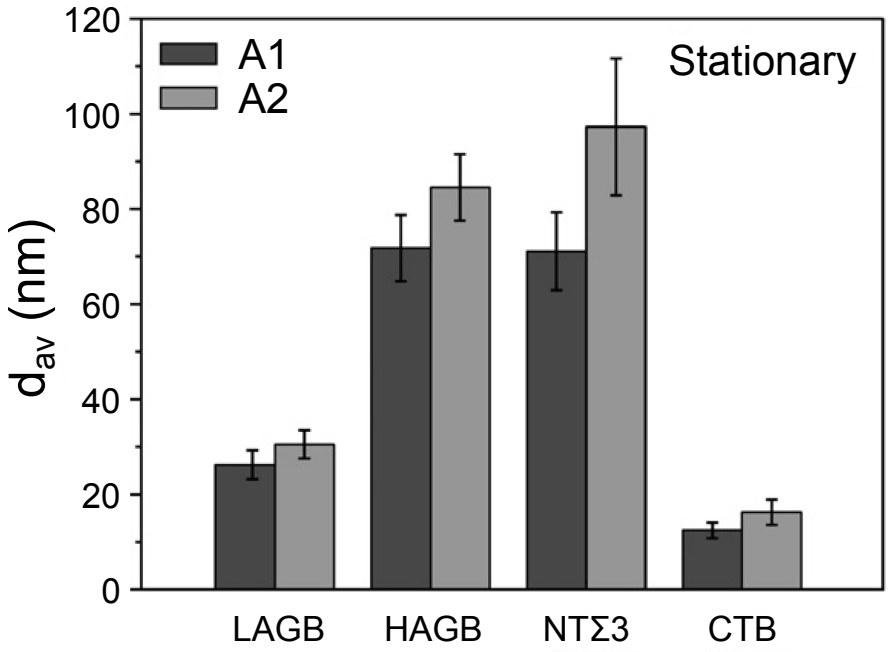

Figure 7.19: Average groove depth values of stationary GBs. Note that the HAGBs does not include Σ3 boundaries.

A significant increase is observed for the stationary NTΣ3 boundaries while the increases in the average groove depth for the other types of boundaries are within the standard error.

Significant differences are however observed for all migrating boundaries. The greatest difference is recorded for general HAGBs while the smallest difference is observed for LAGBs. TBs are not included as migrating GBs since these boundaries are generally classified as stationary boundaries. Note that ITBs are not included since these boundaries consisted of very narrow segments that were typically too short to unambiguously determine whether or not the boundary had migrated.

Importantly, migrating boundaries are observed to leave a surface groove behind (see Fig. 7.14) while forming a new groove at a new position. The groove depth of these abandoned grooves that are no longer associated with a misorientation angle was on average found to be

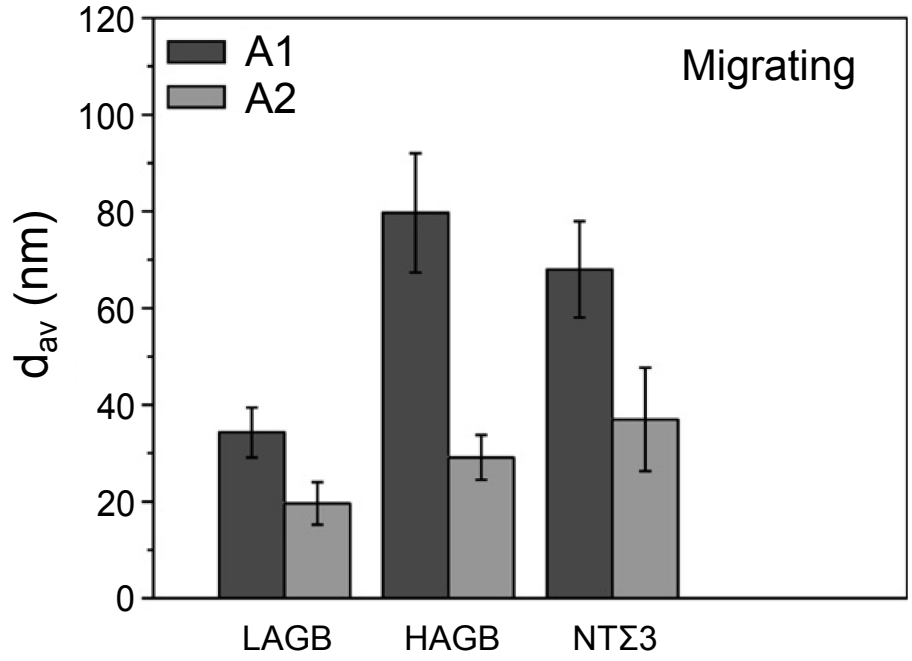

Figure 7.20: Average groove depth values of migrating GBs. Note that the HAGBs does not include Σ3 boundaries.

reduced with 25 % compared to the depth of the groove in condition A1. This decrease in depth is caused by an effective flattening of the surface [93] which is no longer counteracted by the grooving effect at such positions.

The mean surface roughness value was, despite of the topographic changes, observed to be almost insensitive to additional annealing and found to decrease slightly to 10.3 nm. The topography of the examined substrate was characterised by a further development of grooves at stationary GBs while migrating boundaries left grooves behind and formed new GB grooves at new positions. The combined roughening effect, from further GB grooving and additional grooves left behind, must be effectively counterbalanced by the flattening effect and the mean surface roughness is therefore unaffected.

7.2.3 Summary

Ni-5at.%W substrates have been examined in the initial recrystallised condition and after an additional heat treatment at 1025 ^{o}C for 1 hour.

A very strong correlation was observed between the GB groove depth and the boundary type. CTBs and LAGBs were characterised by the smallest depths while HAGBs developed the greatest depths followed by NTΣ3 boundaries and ITBs. Furthermore, a similar trend was also observed for the groove inclination angle as a function of boundary type. It was demonstrated that it is necessary to distinguish between CTBs, ITBs and NTΣ3 boundaries in order to give an appropriate description of the correlation between GB groove depth and boundary type.

A slight increase in the grain size after the additional annealing was accompanied by a strengthening of the cube texture and increase in the fraction of LAGBs. The fractions of TBs and HAGBs decreased accordingly. It was also observed that the total length of boundary trace for misorientations greater than 10^{o} in the EBSD maps decreased by 25 %.

A distinction was made between boundaries that did not change their position after the additional annealing and boundaries that migrated to new positions. Most stationary boundaries developed deeper grooves compared to before the additional annealing. In contrast, migrating

boundaries were observed to leave a surface groove behind and develop shallower grooves at their new positions. The depth of grooves left behind was on average reduced by 25 % compared to the depth of the groove in the initial condition. The mean surface roughness was almost unaffected despite of the topographic changes.

7.3 New strongly textured Ni-Cu-W substrates

This work was motivated by research hypothesis 3 described in section 4.4. The experimental details of the Ni-Cu-W substrates are described in chapter 5 while the applied characterisation techniques are described in chapter 6.

7.3.1 The materials

The Ni-Cu-W substrates are referred to as sample C0, C5, C10 and C15 corresponding to 0, 5, 10 and 15 at.% Cu additions to the Ni-5at.%W alloy, i.e. the Ni-W ratio was kept constant. The lattice parameter and chemical composition of the annealed Ni-Cu-W substrates were characterised by XRD and XRF. It was observed that the lattice parameter increased linearly and only slightly from about 3.54 Å for Ni-5at.%W to 3.55 Å when 15 at.% was added to the Ni-5at.%W alloy.

The XRF analysis showed that the largest differences between the nominal compositions and the measured compositions were 1.51, 1.27 and 0.3 at.% for Ni, Cu and W, respectively. Note that a two-step annealing procedure, see chapter 5, was performed on these substrates to evaluate the potential of these substrates.

7.3.2 Microstructure and topography

Example SEM images of the cold-rolled and annealed sample C0 and C15 are shown in Fig. 7.21(a) and (b), respectively. GB grooves are observed in both samples and marked as (1) in Fig. 7.21(a) and (b).

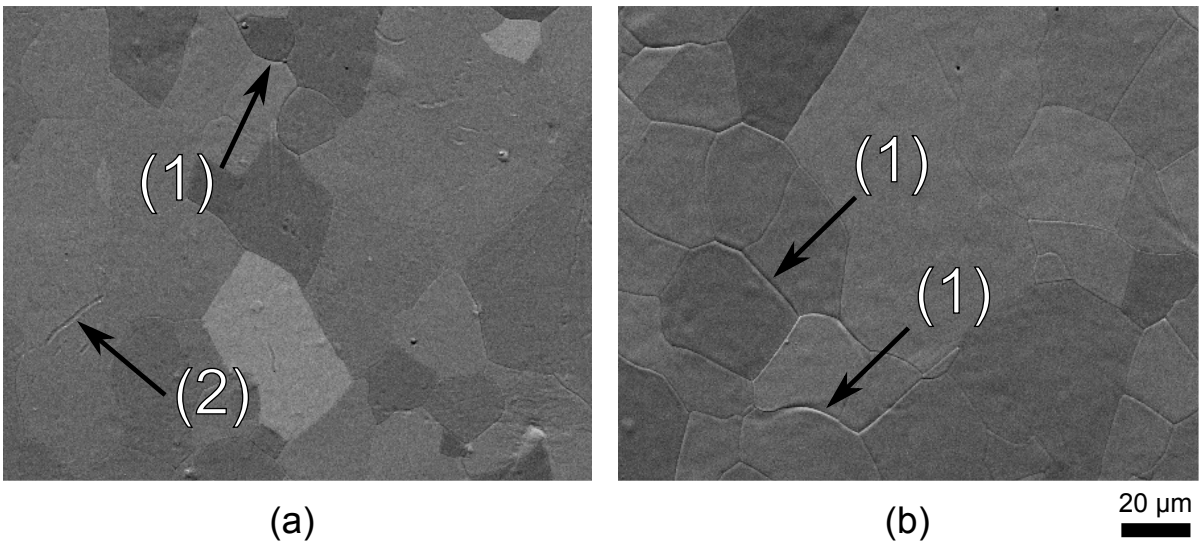

Figure 7.21: SEM micrographs of sample C0 and C15. The numbers indicate positions of GB grooves (1) and a groove left behind at (2).

The GB grooves are more pronounced in the samples with higher Cu-content but more abandoned grooves (see (2) in Fig. 7.21(a)) were observed in sample C0 compared with sample C15.

The microstructure of the annealed samples was characterised by an average grain size between 23 to 26 μm including twin boundaries. The slightly coarser microstructure is apparent for samples with Cu-additions as shown in Fig. 7.22.

The grain size excluding twin boundaries increased from 23 to 27 μm between sample C0 and C15, respectively.

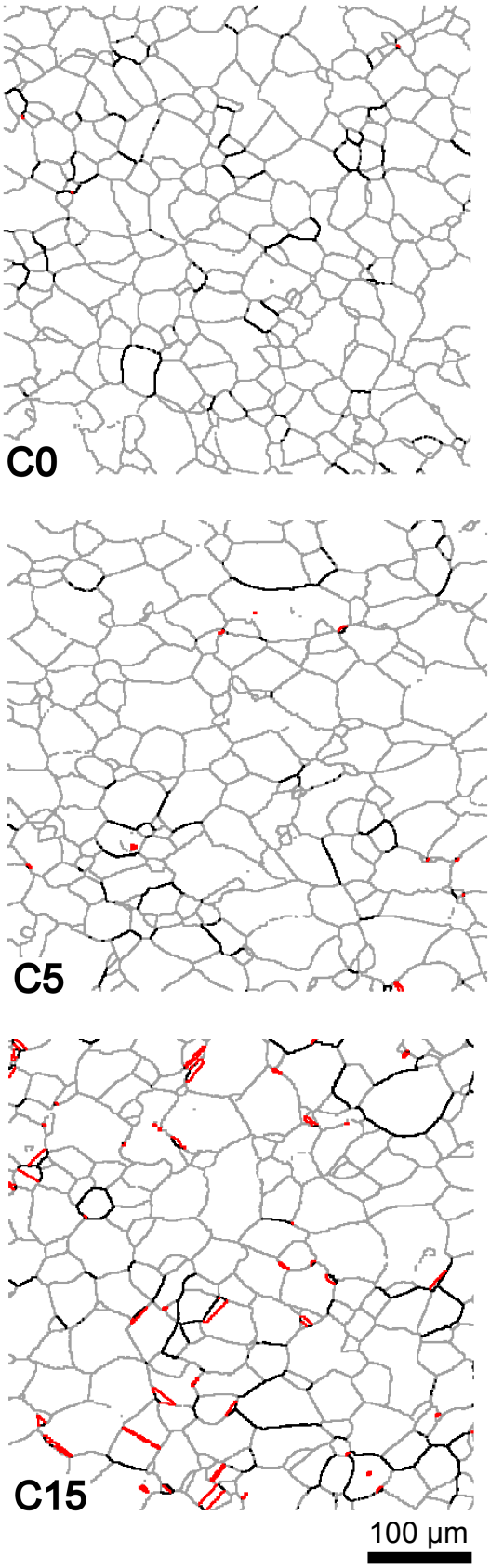

Figure 7.22: EBSD maps collected with a step size of 1 μm of the microstructure of the annealed samples C0, C5 and C15. LAGBs, HAGBs (incl. NTΣ3 GBs) and TBs are drawn by grey, black and red lines, respectively.

Fig. 7.22 clearly demonstrates that the fraction of twins increases with increasing additions of copper. The increase in twin boundaries is also apparent in the fraction of misorientations angles with $\theta \sim 60$ as shown in Fig. 7.23.

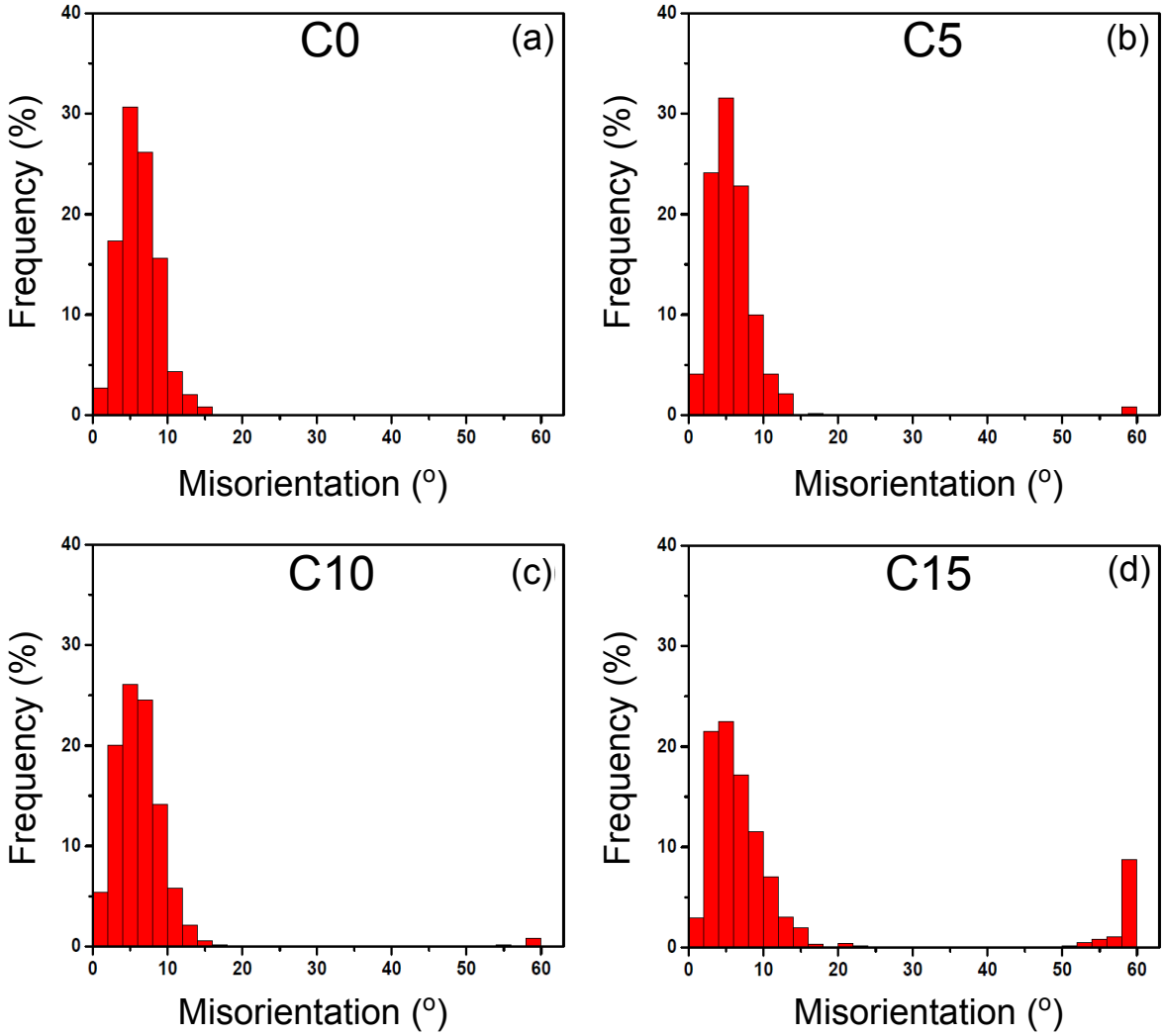

Figure 7.23: Distributions of misorientation angles in the annealed samples C0 to C15 in (a) to (d), respectively.

7.3.3 Texture analysis

Sample C0 and C5 were characterised by a very high area fraction (99 %) of cube texture within a deviation angle of 10^o from the ideal {001}<100> orientation and the fraction of LAGBs was 93 % as shown in Fig. 7.24.

Note that for sample C10, the fraction of cube texture for $\Delta\theta < 10^o$ was still about 98 % and the fraction of LAGBs is only decreased from 93 to 89 % compared with sample C0 and C5. In contrast, sample C15 was characterised by an increased fraction of HAGBs (incl. NTΣ3 boundaries) and annealing twins (see Fig. 7.24). Accordingly, a significantly lower fraction of cube texture was also apparent in this sample.

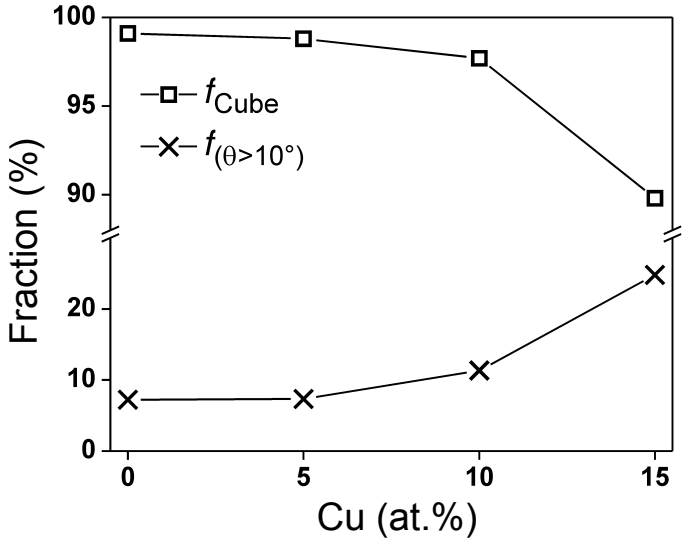

Figure 7.24: Fraction of cube texture (f_{cube}) and fraction of boundaries with misorientations greater than 10^o ($f_{\theta>10^o}$) as a function of Cu-content.

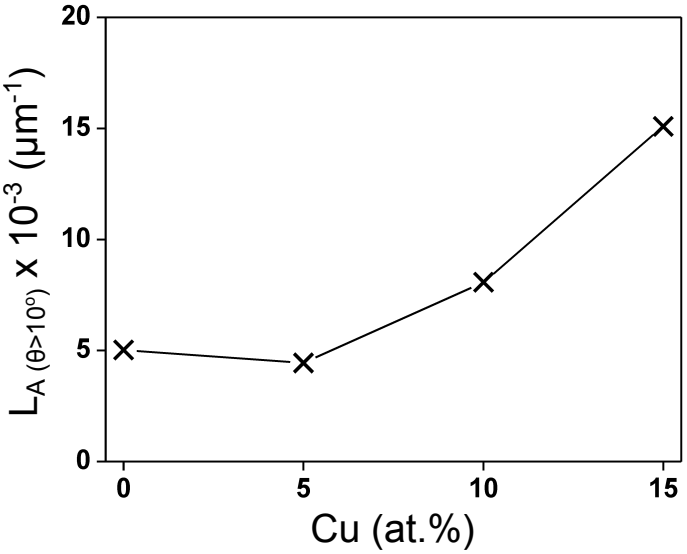

Figure 7.25: Total length of boundary trace, L_A, for boundaries with misorientation angles greater than 10^o, as a function of Cu-content.

The total length of boundary trace (L_A) of GBs with misorientation angles greater than 10^o was evaluated in order to analyse the combined changes of the misorientation angle distribution and the coarsening of the microstructure with increasing Cu-content. L_A values for the different samples are presented in Fig. 7.25.

Fig. 7.24 and Fig. 7.25 clearly demonstrates that the microstructure of sample C5 is very similar to the microstructure of sample C0. Furthermore, the L_A value is in fact slightly lower for sample C5 compared to sample C0. The decrease in the L_A value can be explained by a slightly greater grain size of the ternary alloy with 5 at.% Cu addition compared to the binary Ni-5at.%W alloy. A significant increase in L_A is however observed for both sample C10 and C15 due to the increase in both HAGBs and TBs.

7.3.4 In-plane and out-of-plane texture

The texture of the annealed Ni-Cu-W samples was also characterised by XRD in order to compare these new substrates with FWHM values typically reported for Ni-5at.%W substrates. Both in-plane (ϕ-scan) and out-of-plane (ω-scan) textures were analysed in the annealed substrates and evaluated by their corresponding FWHM values as shown in table 7.2.

Sample	$\Delta\phi$ (^{o})	$\Delta\omega$-TD (^{o})	$\Delta\omega$-RD (^{o})
C0	7.6±0.3	5.4±0.1	8.3±0.1
C5	6.9±0.3	5.4±0.1	7.8±0.1
C10	8.1±0.3	5.3±0.1	8.2±0.1
C15	8.5±0.2	5.7±0.1	10.1±0.2

Table 7.2: FWHM values for the different Ni-Cu-W substrates obtained by XRD.

Interestingly, the FWHM value of both the in-plane and out-of-plane measurements around the RD direction are slightly lower for sample C5 compared to sample C0. Furthermore, the out-of-plane FWHM values of sample C10 is also lower than the values observed for sample C0. However, the in-plane texture is characterised by a lower FWHM value in sample C10 compared to C0. Sample C15 is characterised by the greatest FWHM values for both the in-plane and out-of-plane scans. Conclusively, sample C5 is characterised by a sharper texture compared with the other samples when evaluated by the FWHM values.

However, $\Delta\phi$ in sample C5 is however still slightly larger compared to value (6.5±0.2^o) obtained by Hühne et al.[102] in strongly textured Ni-5at.%W substrates. Note that the $\Delta\omega$ values are smaller for both sample C0, C5 and C10 compared to the FWHM values
, $\Delta\omega_{TD} = 5.5\pm0.5^o$ and $\Delta\omega_{RD} = 8.3\pm0.6^o$, of the Ni-5at.%W substrate reported in [102].

7.3.5 Hardness analysis

The mechanical properties of the new Ni-Cu-W substrates were evaluated by a Vickers micro-hardness measurement and the results are shown in Fig. 7.26.

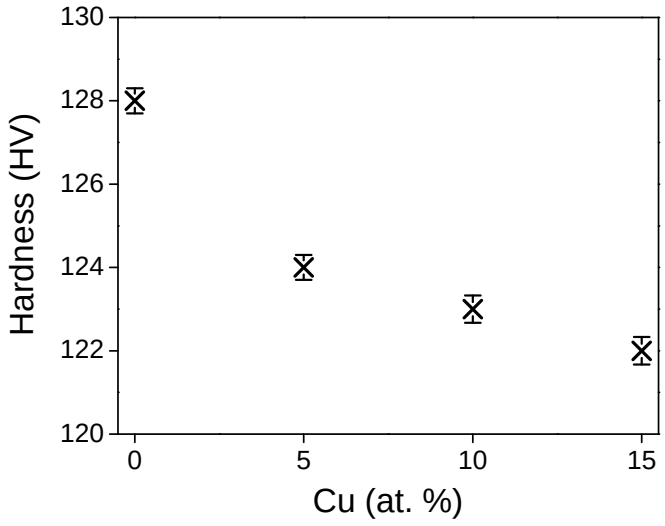

Figure 7.26: Hardness as a function of Cu-content. Error bars correspond to the standard error.

Increasing the Cu-content decreases the hardness of the Ni-Cu-W as expected due to the

addition of a softer metal compared with the hardness of pure Ni and W. However, the change in hardness is relatively small for these Ni-Cu-W alloys and it decreases only from 128 to 124 HV when adding 5 at.% Cu. Importantly, the hardness is still similar to the value obtained for Ni-5at.%W and significantly higher than values reported for Ni-Cu-W alloys with about 50 at.% Cu [77]. The hardness and yield strength of metals are typically linear related and the yield strength of sample C5 to C15 should therefore only be slightly reduced compared with the yield strength of Ni-5at.%W substrates.

7.3.6 Magnetic properties

The magnetic properties are, in contrast to the hardness, more sensitive the additions of Cu. The magnetic moment was measured as a function of temperature for all the Ni-Cu-W samples in order to calculated the Curie temperature. An example of the temperature scan for sample C5 is shown in Fig. 7.27.

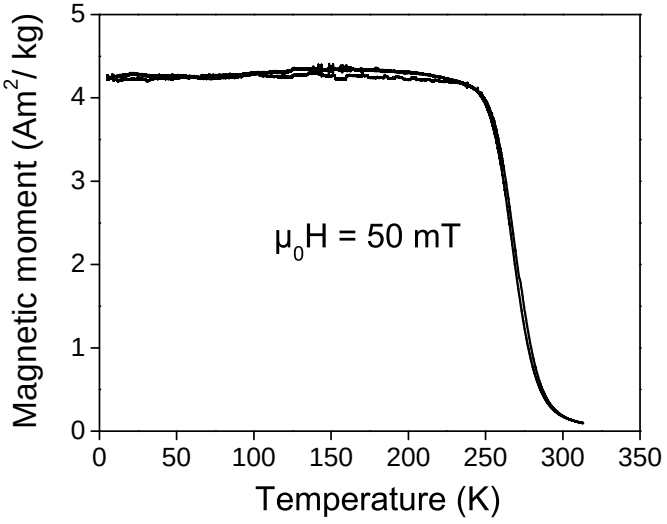

Figure 7.27: Magnetic moment of sample C5 as a function of temperature in a constantly applied magnetic field μ_0H = 50 mT.

A small difference is apparent between the two curves due to hysteresis. A mean curve was calculated from the two curves and the Curie temperature was calculated according to the Heisenberg 3D model as described in chapter 4. The effect of Cu additions on the Curie temperature of the Ni-Cu-W material is shown in Fig. 7.28.

A linear fit of the data in Fig. 7.28 showed that the slope was -12.1±0.6 K/at.%Cu and this value is in good agreement with results on binary Ni-Cu alloys [47]. Note that T_{cu} = 334±8 K for sample C0 and this corresponds well to reported Curie temperatures of Ni-5at.%W [65,73]. Reducing T_{cu} of the Ni-5at.%W below 77 K therefore corresponds to alloying with $\sim$ 22 at.% Cu. Comparing such a Cu-content with the copper concentration in sample C15 it is expected that it will drastically reduce the fraction of cube texture and increase the fraction of HAGBs and TBs, which is not considered beneficial.

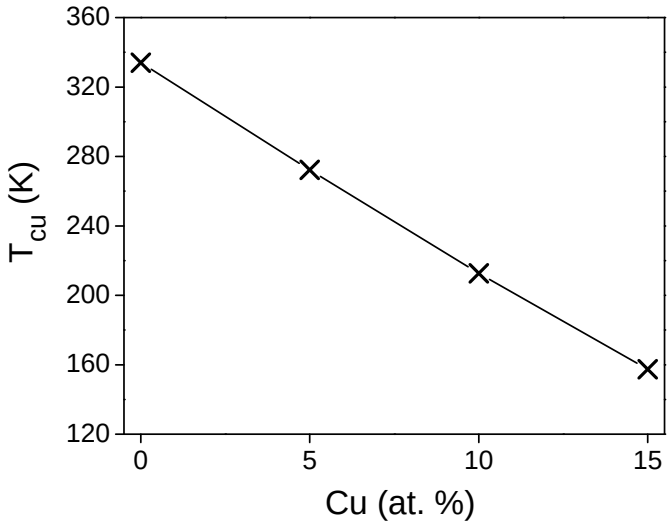

Figure 7.28: Curie temperature as a function of Cu-content.

Magnetic hysteresis was measured in applied magnetic fields between -1 and 1 T and the resulting hysteresis loops are shown in Fig. 7.29.

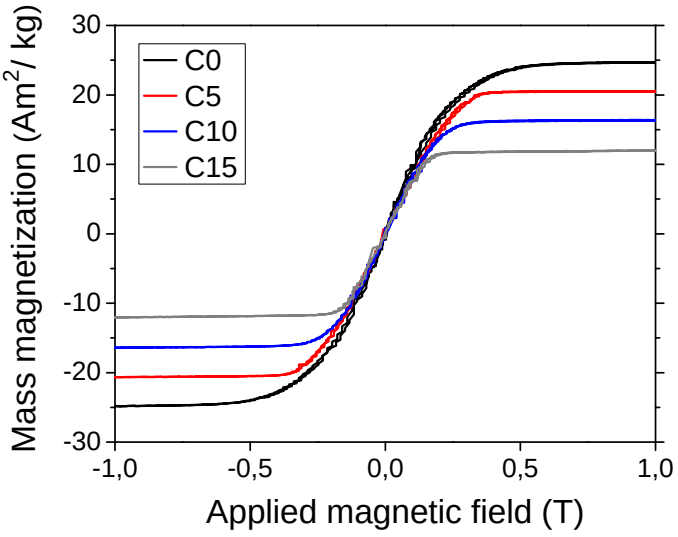

Figure 7.29: Hysteresis loops of sample C0 to C15 performed at 75 K.

Linear horizontal fits were performed on the saturating parts of the hysteresis loops and the saturation mass magnetisation values presented in Fig. 7.30(a) are therefore mean values of the intersections with the magnetisation axis. The addition of copper is effectively reducing the saturation mass magnetisation values compared to Ni-5at.%W. The effective magnetic moment (μ_{eff}) in units of Bohr magnetons for the samples with increasing Cu-content is shown in Fig. 7.30(b).

It is important to note that the μ_{eff} values were calculated from the saturation mass magnetisation values considering only the magnetic moment contribution from the Ni ions. The slope of a linear fit made for the curve in Fig. 7.30(b) shows that the effective magnetic moment of the alloys are reduced by $0.01\mu_B$ for each at.% Cu. Adding 60 at.% Cu to Ni has been

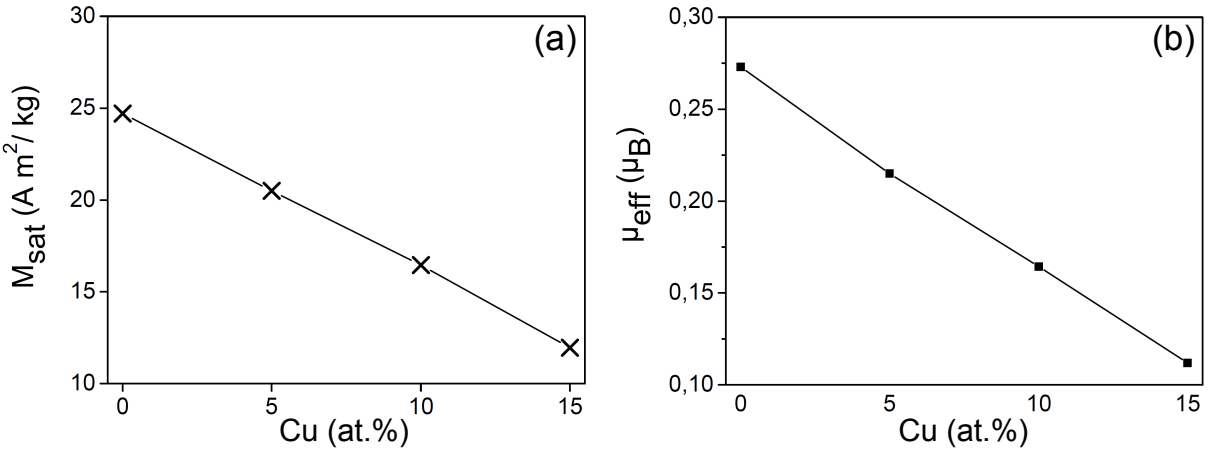

Figure 7.30: Effect of Cu-additions on the saturation mass magnetisation (a) and on the effective magnetic moment (b).

observed to completely suppress ferromagnetism in Ni [47] and the obtained reduction in μ_{eff} as a function Cu-content is therefore in good agreement with the effective magnetic moment of pure Ni (0.6 μ_B).

It is evident from Fig. 7.31 that the saturation mass magnetisation is a linear function of T_{cu} which consistent with the modified Weiss theory of ferromagnetism [63].

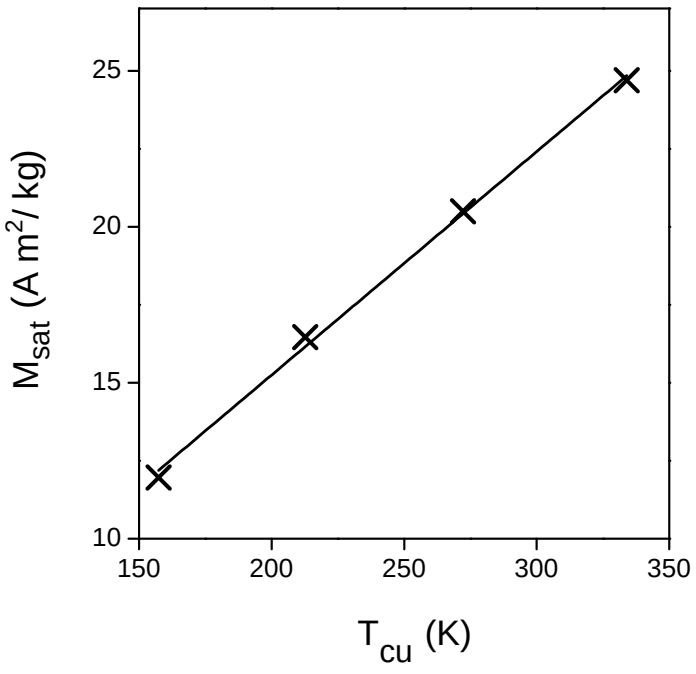

Figure 7.31: Saturation mass magnetisation as a function of the Curie temperature.

Based on the reduction in effective magnetic moment as a function of Cu-content in Fig. 7.30 and the linear relation between M_{sat} and T_{cu} it is suggested that each additional Cu atom adds an electron to the unfilled 3d band of the Ni-W matrix. Accordingly, this will decrease the fraction of uncompensated electron spins and therefore reduce the magnetisation and T_{cu}.

Comparing the fraction of cube texture, fraction of LAGBs and the magnetic properties it is suggested that a Ni-Cu-W composition similar to sample C5, and maybe also C10, would be potential candidates for the use as substrates in CCs with reduced AC losses. A rough estimate of the reduction in AC loss is based on the saturation mass magnetisation values as described in chapter 4. M_{sat} = 20.5 and 16.5 Am^2/kg for sample C5 and C10, respectively, which correspond to an extra loss of about 13 and 8 % for the CC. Consequently, these FM losses are 6 and 11 % lower for sample C5 and C10, respectively, compared with the FM loss due to a Ni-5at.%W substrate for the particular conditions described in chapter 4.

7.3.7 Summary

A series of new Ni-Cu-W substrates with different concentrations of Cu, i.e. 0, 5, 10 and 15 at.%, was investigated. It was demonstrated that an addition of 5 at.% Cu to the Ni-5at.%W alloy significantly reduced the Curie temperature and the saturation mass magnetisation value. The hardness of all the annealed Ni-Cu-W substrates were only slightly affected by Cu-additions compared to the hardness of Ni-5at.%W substrates. The microstructure, fraction of cube texture and the fraction of LAGBs of the sample with 5 at.% Cu were similar to that of the Ni-5at.%W substrate. Further increasing the Cu-content was observed to result in even lower Curie temperatures and saturation mass magnetisation values. However, increasing to 10 at.% Cu resulted in a small reduction in the fraction of cube texture and a lower fraction of LAGBs due to an increased fraction of HAGBs and annealing twins. Further increasing the Cu-content resulted in a significant reduction of the fraction of cube texture and LAGBs.

Comparing the different samples, a Ni-5Cu-5W substrate is suggested as an appropriate candidate material for the use as a substrate in coated conductors with reduced AC losses.

Chapter 8

Conclusions and outlook

8.1 Conclusions of the thesis

There were two aims of this thesis: One; to investigate important aspects of reel-to-reel processing of strongly textured metal substrates for coated conductors, and two; to investigate a new candidate substrate material for use in coated conductors applied under alternating current conditions. The following are conclusions based on the research presented in chapter 7.

The effects on surface roughness and recrystallisation texture after mechanical polishing of a Ni-5at.%W tapes prior to the annealing recrystallisation heat treatment were studied by different experimental techniques. The cold-rolled Ni-5at.%W tapes were mechanically polished, annealed and finally coated with a $Gd_2Zr_2O_7$ buffer layer which was subsequently crystallised. The results obtained have lead to the following conclusions:

- The mean surface roughness was generally observed to decrease after the recrystallisation annealing of the polished Ni-5at.%W tapes compared with the as-polished condition except for very fine polished tapes. Grain boundary surface grooving was observed to impose a lower limit of about 8 nm on the mean surface roughness of the Ni-5at.%W tape after annealing even if the tape was very finely polished. The surface roughness of the buffer layer was found to increase slightly for very fine polished tapes while a small decrease was observed for coarser polished tapes.

- The fraction of cube texture formed in the annealed tapes was very sensitive to the surface roughness before annealing within 5^o from the ideal cube orientation.

Microstructure, texture and topography were studied in a strongly textured Ni-5at.%W tape in the initial condition and after an additional heat treatment simulating a buffer layer crystallisation at 1025 ^{o}C for one hour. Several different techniques were applied to monitor changes in specific positions on the substrate before and after the additional annealing. The following conclusions were drawn from this study:

- A strong correlation between boundary type and average grain boundary depth was observed in the initial condition. Coherent twin boundaries and low angle grain boundaries ($\theta < 10^o$) were characterised by the smallest groove depths while grooves at other boundaries were significantly deeper. A similar correlation was observed between the boundary type and the average inclination angle of the groove wall.

- It is important to distinguish between different types of $\Sigma 3$ boundaries when analysing grain boundary grooves at such boundaries since coherent twins are characterised by much shallower grooves compared with both incoherent twin boundaries and none-twin $\Sigma 3$ boundaries.

- The additional annealing resulted in a slightly increased grain size, a sharper cube texture and a resulting increased fraction of low angle grain boundaries. The total boundary trace of boundaries with misorientation above 10^o was observed to decrease by 25 % after the additional annealing.
- Some grain boundaries remained stationary while other boundaries migrated during the additional annealing. The majority of the stationary boundaries were found to develop deeper grooves while the grooves at migrating boundaries typically became shallower. The migrating boundaries were also observed to leave grooves behind in the grain interior as they moved to a new position. The depth of these abandoned grooves was reduced by 25 % compared to the depth of the groove prior to the additional annealing.
- The mean surface roughness was almost unaffected.

A series of strongly cube-textured Ni-Cu-W tapes were prepared and investigated with respect to microstructure, texture, hardness and magnetic properties. Starting from Ni-5at.%W, alloys with additions of Cu (5, 10 and 15 at.%) were prepared keeping the Ni-W ratio constant. The following conclusions were drawn from this investigation:

- Adding 5 at.% Cu to the Ni-5at.%W was observed to substantially reduce the Curie temperature, the saturation mass magnetisation without significantly modifying the microstructure, texture and hardness of the recrystallised substrate.
- The Curie temperature and saturation mass magnetisation were observed to further decrease with increasing Cu-content. However, a decrease in the fraction of cube texture was also observed when increasing the Cu-content to 10 and 15 at.% as a result of an increased fraction of annealing twins.
- The strongly cube-textured Ni-5 at.%W with 5 at.% Cu addition, appears to be a good candidate material as a substrate material for RABiTS-based coated conductors.

8.2 Experimental outlook

This section presents some recommendations, thoughts and ideas for future experiments.

Based on the topographic changes in the Ni-5at.%W substrate during additional annealing it is recommended that the temperature used for buffer layer crystallisation is as low as possible to avoid extensive grain boundary grooving and boundary migration in the metal substrate material.

The effect of abandoned surface grooves in Ni-5at.%W substrates with a full coated conductor layer stack should be investigated using magneto optical microscopy. Using such a test it may be possible to characterise if such defects contributes to the GB network and acts as a possible percolation path.

Finally, Ni-Cu-W substrates with both 5 and 10 at.% Cu should be coated with buffer layers and a YBCO layer to test finally the suitability of these substrates for coated conductor usage.

Additional tests, with increased amount of W in the Ni-Cu-W substrates should be investigated since W is more effectively reducing the Curie temperature and the saturation mass magnetisation compared to Cu. Adding Cu should ease the cold rolling process while reducing the recrystallisation temperature which may be beneficial for such substrates with a high tungsten content.

Bibliography

[1] O. Edenhofer, R.P. Madruga, Y. Sokona, K. Seyboth, P. Eickemeier, P. Matschoss et al., Renewable Energy Sources and Climate Change Mitigation (2012) Special Report of the Intergovernmental Panel on Climate Change Climate.

[2] M.I. Hoffert, K. Caldeira, A.K. Jain, E.F. Haites, L.D.D. Harveyk, S.D. Potter et al., Nature 395 (1998) 881-4.

[3] Danish Commision on climate change policy, Report (2010) ISBN: 978-87-7844-879-8.

[4] http://www.ens.dk/da-DK/Info/TalOgKort/Statistik_og_noegletal/Oversigt_over_energisektoren/Stamdataregister_vindmoeller/Sider/forside.aspx (accessed August 26, 2012).

[5] A. Westwood, Siemens at full throttle, Renew. Energy Focus 8 (2007) 28.

[6] A.B. Abrahamsen, N. Mijatovic, E. Seiler, T. Zirngibl, C. Træholt, P.B. Nørgård et al., Supercond. Sci. Technol. 23 (2010) 034019 (8pp).

[7] J. Sarrao, Basic Research Needs For Superconductivity, Report of the basic Energy Sciences (2006) Argonne National Laboratory, U.S.A.

[8] S.M. Schoenung, R.L. Bieri, W.R. Meier, W.J. Schafer, T.C. Bickel, IEEE Trans. on App. Supercond., 3 (1993) 200-3.

[9] A.P. Malozemoff, Y. Yamada, Coated Conductors: Second Generation of HTS wires (2012) 100 years of superconductivity, edited by H. Rogalla, P. Kes, CRC Press, LLC New York.

[10] K. Fossheim, A. Sudbø, Superconductivity - Physics and Applications (2004) John Wiley & Sons, Ltd., United Kingdom.

[11] Second-Generation HTS Conductors (2010) edited by A. Goyal, Kluwer Academic Publishers, Massachusetts, USA.

[12] H.K. Onnes, KNAW, Proceedings 13 (1911) 1274-6.

[13] J. Bardeen, L.N. Cooper, J.R. Schrieffer, Phys. rev. 108 (1957) 1175-204.

[14] N. Mitchell, D. Bessette, R. Gallix, C. Jong, J. Knaster, P. Libeyre et al., IEEE Trans. on App. Supercond.,18 (2008) 435-40.

[15] D. Larbalestier, A. Gurevich, D.M. Feldmann, A. Polyanskii, Nature, 414 (2001) 368-77.

[16] J.G. Bednorz, K.A. Miiller, Z. Phys. B, Condensed Matter 64 (1986) 189-93.

[17] M.K. Wu, J.R. Ashburn, C.J. Torng, P.H. Hor, R.L. Meng, L. Gao, Z.J. Huang et al., Phys. Rev. Let. 58 (1987) 908-10.

[18] A. Schilling, M. Cantoni, J.D. Guo, H.R. Ott, Nature 363 (1993) 56-8.

[19] A. Abrahamsen, Superconductor based energy production (2008) 131-50.

[20] A. Abrikosov, Zh. Eksp. Teor. Fiz., 32 (1957) 1442-52.

[21] J.D. Jorgensen, B.W. Veal, A. P. Paulikas, L. J. Nowicki, G. W. Crabtree, Phys. Rev. B 41 (1990) 1863-77.

[22] C.C. Tsuei, J. R. Kirtley, Rev. of Modern Phys.,72 (2000) 969-1016.

[23] M. Suenaga, A.K. Ghosh, Y. Xu, D. O. Welch, Phys. Rev. Letters,66 (1991) 1777-80.

[24] P.W. Anderson, Y.B. Kim, Rev. of Modern Phys. (1964) 39-43.

[25] J.L. MacManus-Driscoll, S.R. Foltyn, Q.X. Jia, H.Wang, A. Serquis, L. Civale et al., Nature Mater. 3 (2004) 439-43.

[26] P. Paturi, T. Kulmala, J. Raittila, J.-C. Grivel, R. Laiho, N.H. Andersen, Phys. C 408-410 (2004) 935-6.

[27] H. Hilgenkamp, J. Mannhart, Rev. Mod. Phys. 74 (2002) 485-549.

[28] J.H. Durrell, N.A. Rutter, Supercond. Sci. Technol. 22 (2009) 013001 (18pp).

[29] D. Dimos, P. Chaudhari, J. Mannhart, Phys. Rev. B 41 (1990) 4038-49.

[30] R. Held, C.W. Schneider, J. Mannhart, L.F. Allard, K.L. More, A. Goyal, Phys. Rev. B 79 (2009) 1-7.

[31] N.F. Heinig, R.D. Redwing, J.E. Nordman, D. C. Larbalestier, Phys. Rev. B 60 (1999) 1409-17.

[32] X.D. Wu, R.C. Dye, R.E. Muenchausen, S.R. Foltyn, M. Maley, A.D. Rollett et al., Appl. Phys. Lett. 58 (1991) 2165-7.

[33] M. Muralidhar, N. Sakai, M. Jirsa, M. Murakami, N. Koshizuka, Supercond. Sci. Technol. 18 (2005) 9-12.

[34] M.W. Rupich, W. Zhang, X. Li, T. Kodenkandath, D.T. Verebelyi, U. Schoop et al., Physica C 412-414 (2004) 877-84.

[35] A. Goyal, M. P. Paranthaman, U. Schoop, MRS Bulletin (2004) 552-61.

[36] X. Obradors, T. Puig, A. Pomar, F. Sandiumenge, S. Pinõl, N. Mestres et al., Supercond. Sci. Technol. 17 (2004) 1055-64.

[37] S. Sathyamurthy, M. Paranthaman, H-Y. Zhai, H.M. Christen, P.M. Martin, A. Goyal, J. Mater. Res. 17 (2002) 2181-4.

[38] A. Goyal, D. P. Norton, D. K. Christen, E. D. Specht, M. Paranthaman, D. M. Kroeger et al., Appl. Supercond. 4 (1996) 403-27.

[39] F.J. Humphreys, M. Hatherly, Recrystallization and related annealing phenomena (2004) Elsevier Ltd., Oxford, U.K.

[40] J. Eickemeyer, D. Selbmann, R. Opitz, H. Wendrock, E. Maher, U. Miller, W. Prusseit, Physica C 372-376 (2002) 814-7.

[41] V. Selvamanickam, Coated Conductors: From R&D to Manufacturing to Commercial Applications, EUCAS, Superconductivity Centennial Conference, September 19-23 (2011), Den Haag, The Netherlands.

[42] A. P. Malozemoff, S. Fleshler, M. Rupich, C. Thieme, X. Li, W. Zhang et al., Supercond. Sci. Technol. 21 (2008) 034005 (7pp).

[43] X. Obradors, T. Puig, A. Pomar, F. Sandiumenge, N. Mestres, M. Coll, Supercond. Sci. Technol. 19 (2006) 13-26.

[44] P. Sachenko, J.H. Schneibel, J.G. Swadener, W. Zhang, Phil. Mag. Lett, 80 (2000) 627-31.

[45] W.W. Mullins, Acta Metal. 6 (1958) 414-27.

[46] W. W. Mullins, P. G. Shewmon, Acta Metall. 7 (1959) 163-70.

[47] B. De Boer, J. Eickemeyer, N. Reger, L. Fernandez, J. Richter, B. Holzapfel, Acta mater. 49 (2001) 1421-8.

[48] T. A. Gladstone, J. C. Moore, A. J. Wilkinson, C. R. M. Grovenor, IEEE Trans. Appl. Supercond. 11 (2001) 2923-6.

[49] T. G. Truchan , F. H. Rountree, M. T. Lanagan, S. M. McClellan, D. J. Miller, IEEE Trans. Appl. Supercond. 10 (2000) 1130-3.

[50] L.E. Murr, Interfacial phenomena in metals and alloys (1975) Addison-Wesley Pub. Co., Reading, MA.

[51] K. Knoth, R. Hühne, S. Oswald, L. Schultz, B. Holzapfel, Supercond. Sci. Technol. 18 (2005) 334-9.

[52] E. Varesi, G. Celentano, T. Petrisor, V. Boffa, L. Ciontea, V. Galluzzi et al., Supercond. Sci. Technol. 16 (2003) 498-505.

[53] S. Zhu, L. Liu, D. Xu, H. Liu, X. Song, D. Hong et al., J. Supercond. Nov. Magn. 24 (2011) 1869-75.

[54] S. Kreiskott, P. N. Arendt, L. E Bronisz, S. R. Foltyn, V. Matias, Supercond. Sci. Technol. 16 (2003) 613-6.

[55] R. Gärtner, R. Hühne, J. Engelmann, J. Hänisch, R. Kaltofen, S. Oswald, L. Schultz, B. Holzapfel, IEEE Trans. Appl.Supercond. 21 (2011) 2920-23.

[56] Y. Zhao, J.-C. Grivel, A. B. Abrahamsen, D. Pavlopoulos, J. Bednarćík, M. von Zimmermann, IEEE Tran. App. Supercond. 21 (2011) 2912-5.

[57] Z. Aslanoglu, Y. Akin, M. I. El-Kawni, W. Sigmund, Y. S. Hascicek, Physica C 384 (2003) 501-6.

[58] M. P. Paranthaman, X. Qiu, F. A. List, K. Kim, Y. Zhang, X. Li, S. Sathyamurthy et al., IEEE Trans. Appl. Supercond. 21 (2011) 3059-61.

[59] V. S. Sarma, J. Eickemeyer, A. Singh, L. Schultz, B. Holzapfel, Acta Materialia 51 (2003) 4919-27.

[60] S. Sathyamurthy, M. Paranthaman, M. S. Bhuiyan, E. A. Payzant, D. F. Lee, A. Goyal et al., IEEE Trans. Appl. Supercond.15 (2005) 2974-6.

[61] V. S. Sarma, J. Eickemeyer, L. Schultz, B. Holzapfel, Scripta Materialia 50 (2004) 953-7.

[62] S. Blundell, Magnetism in Condensed Matter (2001) Oxford University Press Inc., New York.

[63] R. M. Bozorth, Ferromagnetism (2003) John Wiley & Sons Inc., Hoboken.

[64] N. W. Ashcroft, N. D. Mermin, Solid State Physics (1976) Thomson Learning Inc., USA.

[65] A.O. Ijaduola, J.R. Thompson, A. Goyal, C.L.H. Thieme, K. Marken, Physica C 403 (2004) 163-71.

[66] D. C. Mattis, The theory of magnetism made simple (2006) World Scientific Publishing Co. Pte. Ltd., New Jersey, USA.

[67] O. Tsukamoto, M. Liu, S. Odaka, D. Miyagi, K. Ohmatsu, Physica C 463-465 (2007) 766-9.

[68] W.T. Norris, J. Phys. D 3 (1970) 489-507.

[69] J.R. Thompson, A. Goyal, D.K. Christen, D.M. Kroeger, Physica C 370 (2002) 169-76.

[70] T. Aytug, A. Goyal, N. Rutter, M. Paranthaman, J.R. Thompson, H.Y. Zhai, J. Mater. Res. 18 (2003) 872-7.

[71] J. H. Claassen, C. L. H. Thieme, Supercond. Sci. Technol. 21 (2008) 105003 (5pp).

[72] R. Nast, B. Obst, W. Goldacker, Physica C 372-376 (2002) 733-7.

[73] U. Gaitzsch, J. Eickemeyer, C. Rodig, J. Freudenberger, B. Holzapfel, L. Schultz, Scripta Mater. 62 (2010) 512-5.

[74] H. R. Kerchner, D. P. Norton, A. Goyal, J. D. Budai, D. K. Christen, D. M. Kroeger, Appl. Phys. Lett. 71 (1997) 2029-31.

[75] V. M. Schastlivtsev, V. V. Ustinov, D. P. Rodionov, B. K. Sokolov, I. V. Gervaseva, Y. V. Khlebnikova, Doklady Physics 49 (2004) 167-70.

[76] J. Eickemeyer, R. Hühne, A. Güth, C. Rodig, U. Gaitzsch, J. Freudenberger et al., Supercond. Sci. Technol. 23 (2010) 085012 (6pp).

[77] A. Vannozzi, V. Galluzzi, A. Mancini, A. Rufolini, A. Augieri, A. A. Armenio et al., IEEE Trans. Appl. Supercond. 21 (2011) 2908-11.

[78] A. Vannozzi, G. Celentano, A. Angrisani, A. Augieri, L. Ciontea, I. Colantoni, J. Phys. Con. Ser. 97 (2008) 012188.

[79] M. Gao, H. Suo, Y. Zhao, J.-C. Grivel, Y. Cheng, L. Ma, Acta Mater. 58 (2010) 1299-1308.

[80] P. R. Subramanian, D. E. Laughlin, Phase diagrams of binary tungsten alloys (1991) edited by S. V. N. Naidu, P. R. Rao, Indian inst. met., Calcutta.

[81] J. Eickemeyer, D. Selbmann, R. Opitz, H. Wendrock, S. Baunack, V. S. Sarma, B. Holzapfel, L. Schultz, E. Maher, Physica C 418 (2005) 9-15.

[82] J. Eickemeyer, D. Selbmann, H. Wendrock, A. Güth, B. Holzapfel, Supercond. Sci. Technol. 18 (2005) 770-5.

[83] J. Eickemeyer, D. Selbmann, R. Opitz, B. de Boer, B. Holzapfel, L. Schultz, U. Miller, Supercond. Sci. Technol. 14 (2001) 152-9.

[84] P. Villars, A. Prince, Handbook of Ternary Alloy Phase Diagrams (1995) edited by H. Okamoto, ASM Int.

[85] B. Verlinden, J. Driver, I. Samajdar, R. D. Doherty, Thermo-Mechanical Processing of Metallic Materials (2007) Elsevier Ltd., The Netherlands.

[86] M. M. Woolfson, An Introduction to X-ray Crystallography (1997) 2^{nd} ed., Cambridge University Press, U.K.

[87] I. Chasiotis, Atomic Force Microscopy in Solid Mechanics (2008) Springer Handbook of Experimental Solid Mechanics, edited by N.W. Sharpe, Springer Science, LLC New York.

[88] Nanosurf AG: Operating Instructions, EasyScan 2 AFM, v. 1.3 (2005)

[89] O. Engler and V. Randle, Introdcution to texture analysis, 2^{nd} ed. (2010) CRC Press, Taylor & Francis Group, Boca Raton.

[90] F. J. Humphreys, J. Microsc. 195 (1999) 170-85.

[91] W.Q. Cao, A. Godfrey, Q. Liu, Mater. Sci. Eng. A 361 (2003) 9-14.

[92] W. D. Callister, Materials Science and Engineering - An Introduction (2007) 7^{th} ed., John Wiley & Sons, Inc, USA.

[93] W. W. Mullins, J. Appl. Phys. 30 (1959) 77-83.

[94] P. A. Beck, P. R. Sperry, H. Hu, J. Appl. Phys. 21 (1950) 420-5.

[95] S.K. Chen, C.F. Liu, P.X. Zhang, L. Zhou, Mat. Sci. Forum 546-549 (2007) 1997-2002.

[96] O. V. Mishin, X. Huang, Mater. Sci. Forum 294-296 (1999) 401-4.

[97] O. V. Mishin, J. Mater. Sci. 33 (1998) 5137-43.

[98] J. Eickemeyer, R. Hühne, A. Güth, C. Rodig, H. Klauß, B. Holzapfel, Supercond. Sci. Technol. 21 (2008) 105012 (7pp).

[99] Y. Zhao, H. Suo, M. Liu, D. Liu, Y. Zhang, M. Zhou, Phys. C 440 (2006) 10-6.

[100] K. T. Kim, J. H. Lim, J. H. Kim, S. H. Jang, J. Joo, C.-J. Kim et al. IEEE Trans. Appl. Supercond. 15 (2005) 2683-6.

[101] D. C. Brandon, Acta Metall. 14 (1966) 1479-84.

[102] R. Hühne, J. Eickemeyer, V. S. Sarma, A. Güth, T. Thersleff, J. Freudenberger, Supercond. Sci. Technol. 23 (2010) 034015 (7pp).

[103] A. Goyal, D.F. Lee, F.A. List, E.D. Specht, R. Feenstra, M. Paranthaman et al., Physica C 357-360 (2001) 903-13.

[104] V. S. Sarma, J. Eickemeyer, C. Mickel, L. Schultz, B. Holzapfel, Mater. Sci. Eng. A 380 (2004) 30-3.

[105] J. R. Groves, P. N. Arendt, H. Kung, S. R. Foltyn, R. F. DePaula, L. A. Emmert, IEEE Trans. Appl. Supercond. 11 (2001) 2822-5.

[106] U. Balachandran, B. Ma, M. Li, B.L. Fisher, R.E. Koritala, R.A. Erck, S.E. Dorris, Physica C 378-381 (2002) 950-4.

Chapter 9

Abbreviations

AV - Abrikosov vortex, $\Phi_0 = h/2e = 2.0678{\cdot}10^{-15}$ Tm^2
B - Magnetic induction (T)
Bi-2223 - $Bi_2Sr_2Ca_2Cu_3O_{10}$
CC - Coated conductor
C_C - Crystal coordinate system
C_S - Sample coordinate system
CSD - Chemical solution deposition
CTB - Coherent twin boundary
DGS - Diamond Grain Size (μm)
e - The electron charge = $1.6022{\cdot}10^{-19}$ C
F_L - Lorentz force (N)
FCC - Face centered cubic
g - orientation matrix
GB - Grain boundary
g_L - Landé g-factor
H - Magnetic field strength (Am^{-1})
h - Plank's constant = $6.626{\cdot}10^{-34}$ Js
HAGB - High angle grain boundary
H_C - Critical magnetic field (Am^{-1})
HTS - High temperature superconductor
IBAD - Ion beam assisted deposition
I_C - Critical current (A)
ISD - Inclined substrate deposition
I_T - Transport current (A)
ITB - Incoherent twin boundary
J - Total angular momentum (kg·m/s^2)
J_C - Critical current density (A/cm^2)
J_E - Engineering current density (A/cm^2)
J_T - Transport current density (A/cm^2)
L - Orbital angular momentum (kg·m/s^2)
L_A - Stereological length per unit area (μm^{-1})
LAGB - Low angle grain boundary
LTS - Low temperature superconductor
M - Magnetisation (Am^{-1})
MOD - Metal organic deposition
MOCVD - Metal organic chemical vapour deposition
m_s - Spin quantum number

$\mathbf{M}_s$ - Saturation magnetisation (Am^{-1})
$\mathbf{M}_{sat}$ - Saturation mass magnetisation (Am^2/g
N - Number of atoms
N_A - Avogadro's number = $6.022{\cdot}10^{23}$ mol^{-1}
ND - Normal direction
n_s - Density of superconducting electrons
PIT - Powder in tube
PLD - Pulsed laser deposition
PPR - Per pass reduction (%)
PVD - Physical vapor deposition
RABiTS - Rolling assisted bi-axially textured substrate
RD - Rolling direction
RE-BCO - (Rare earth)-$Ba_2Cu_3O_7$
RMS - Root mean square
S - Spin angular momentum ($kg{\cdot}m/s^2$)
S_A - Arithmetic surface roughness (nm)
TB - Twin boundary
T_C - Critical transition temperature (K)
T_{cu} - Curie temperature (K)
TD - Transverse direction
TMP - Thermo-mechanical processing
TTR - Total thickness reduction (%)
V - Volume (m^3)
XRD - X-ray diffraction
XRF - X-ray fluorescence
YBCO - $YBa_2Cu_3O_7$
YSZ - Yttrium stabilised zirconium
θ - Misorientation angle (^{o})
$\Delta\theta$ - Deviation angle (^{o})
μ - Atomic magnetic moment (Am^2)
μ_B - Bohr magneton = $9.274{\cdot}10^{-24}$ Am^2
μ_0 - Magnetic permeability of free space = $4\pi{\cdot}10^{-7}$ Hm^{-1}
μ_{eff} - Effective magnetic moment (μ_B)
χ_m - Magnetic susceptibility

Chapter 10

Appendix - A

The concept of crystallographic texture is essential to coated conductors and a description of relevant aspects of texture is therefore considered a prerequisite. This appendix introduces crystallographic orientation and texture in a polycrystalline material. A brief presentation of methods commonly applied for evaluating texture is also included.

10.1 Crystal structure and orientation

The Ni-based material considered in this thesis has a face-centered cubic (FCC) structure. A crystal plane in a FCC structure is represented by the three Miller indices (hkl) while a direction is represented by a vector [uvw]. A specific crystallographic orientation can thereby be described by (hkl)[uvw].

Cubic crystal systems have a high symmetry and there are 24 equivalent descriptions of the same orientation. Accordingly, these orientations are grouped into families of planes and directions, and then denoted as {hkl} and <uvw>, respectively. An orientation can therefore also be represented as {hkl}<uvw>. The cube {001}<100> orientation is an example of such a representation.

A polycrystalline material, such as nickel, consists of grains separated by grain boundaries (GBs). Each grain has an unique orientation which is different from orientations of adjacent grains.

A reference frame is required when evaluating the orientations of individual grains in the sample. An example of such a reference frame is the sample coordinate system (C_s) of a rolled material defined by the normal, rolling and transverse directions. The corresponding axes are named ND, RD and TD, respectively, and are shown in Fig. 10.1. The grey cube in Fig. 10.1 represents the orientation of a single grain located inside the rolled sample that is shown as the transparent box. The crystal directions of the grain corresponding to the crystal coordinate system (C_c) are drawn for clarity.

Consequently, orientation can also be represented by a 3×3 rotation matrix, g, which is directly related to the Miller indices and describes the rotation of C_c with respect to C_s [89].

$$C_c = g \cdot C_s. \tag{10.1}$$

The so-called Euler angles (ϕ_1, Φ, ϕ_2) defines the three necessary rotations needed to transform C_s onto C_c and is often used for presenting orientations in a specific reference orientation space, the Euler space [89].

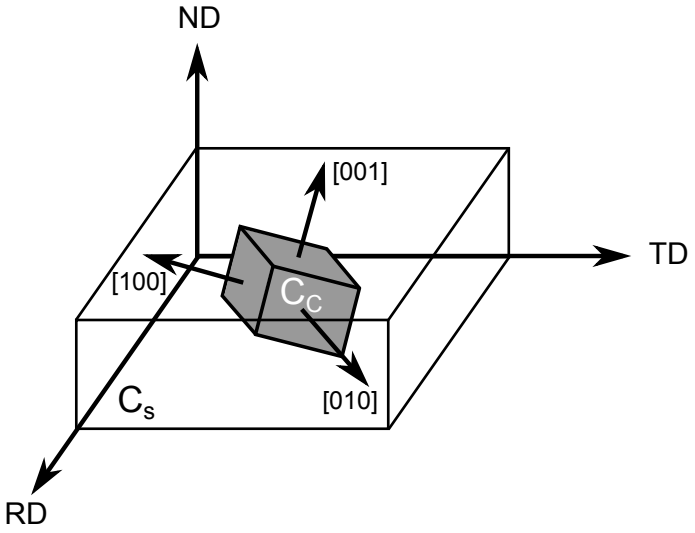

Figure 10.1: Crystal coordinate system, C_c, with the [100], [010] and [001] directions and sample coordinate system, C_s, given by the ND, RD and TD axes.

10.2 Texture and misorientations

Crystallographic texture is defined as a preferred orientation and is a distribution of orientations in a polycrystalline material. A strong texture with a single dominant component develops if the majority of grains in a sample have similar orientations. However, a strong texture can also consist of several different orientation components, such as a rolling texture produced in FCC materials by cold rolling. In contrast, a material with randomly orientated grains has a weak (or random) texture. The strength of texture components can be measured as a frequency of grains with orientations within a certain angle from the ideal orientations describing this component [89].

The orientation distribution does not include information about boundary misorientations which are the orientation differences between adjacent grains in a polycrystalline material. Boundary misorientation, M, is defined by the smallest rotational angle θ, obtained by choosing a common axis for two grains and then performing the smallest possible angular rotation about this axis. In this thesis, low angle grain boundaries (LAGBs) were defined by $\theta<10^o$, while high angle grain boundaries (HAGBs) were defined by $\theta\geq10^o$.

There can also be special grain boundaries in the microstructure which are usually represented by a Σ-value. This value is defined as the reciprocal of the ratio of coincidence lattice sites to the total number of lattice sites [39]. For example, the $\Sigma3$ boundaries are formed between a twin-to-cube {212}<122> orientated grain that is produced in a cube {001}<100> orientated grain during annealing. Twin grains are typically extended throughout the cube orientated grain. The $\Sigma3$ boundary misorientation corresponds to a 60^o rotation about the <111> axis. Fig. 10.2(a) shows a two dimensional sketch of annealing twins (TW and TW') formed in a cube orientated grain (the matrix grain) which is then divided into two grains (W_1 and W_1').

The sketch also illustrates the $\Sigma3$ boundaries: W_1-TW, TW-W_1' and W_1'-TW' that are formed between twin grains and the matrix grain. Such twin boundaries (TBs) have an almost exact 60^o <111> misorientation ($<3^o$) and therefore termed "true" TBs [96]. In contrast, the following boundaries: W_2-TW, W_6-TW, W_4-TW' and W_5-TW' are formed between twin grains and non-matrix grains, that are slightly disoriented from the matrix grain (W_1, W_1'). The misorientation at these $\Sigma3$ boundaries is larger than the misorientation at true TBs though it may still satisfy the allowable deviation $\Delta\theta$=8.66^o for a $\Sigma3$ boundary [101].

A distinction is therefore made between true TBs with deviations $\Delta\theta$ $<3^o$ and "non-twin

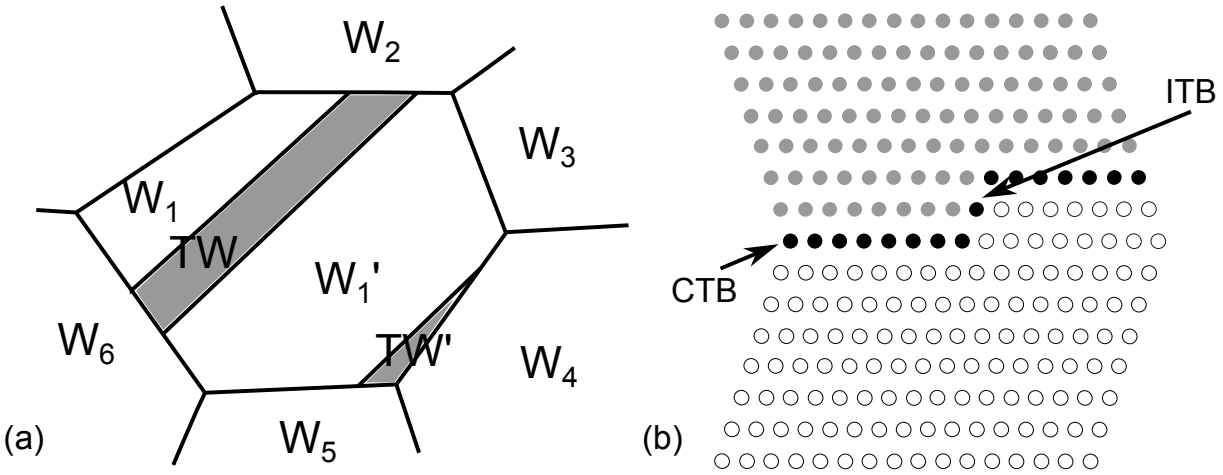

Figure 10.2: (a) Sketch of annealing twins and possible Σ3 boundaries in a strongly cube-textured FCC material. W and TW refer to grains with the cube orientation and its twin component, respectively [97]. (b) Mirror-imaged crystal lattices at a twin boundary indicating the coherent (CTB) and incoherent (ITB) segments [39].

Σ3" boundaries (NTΣ3) with deviations $\Delta\theta$=3-8.66^o in this thesis. It should be noted that TBs may consist of straight coherent and incoherent segments. The coherent TB segments are generally immobile and parallel to the mirror-axis as shown in 10.2(b). In contrast, incoherent TB segments are mobile and inclined to the coherent segments [89].

FCC materials, such as Ni, with a high stacking fault energy (SFE ∼200 mJ m^{-2}), typically forms a recrystallization cube {001}<100> texture after appropriate thermo-mechanical processing [89].

Texture evaluation

Texture is evaluated in the present work by means of pole figures, rocking curve scans and area fractions of cube texture. The following is a brief introduction to pole figures, in-plane and out-of-plane texture.

Pole figures

The normal vector of a plane can be described as a reference point (pole) on a unit sphere as shown in Fig. 10.3(a) for the {001} planes.

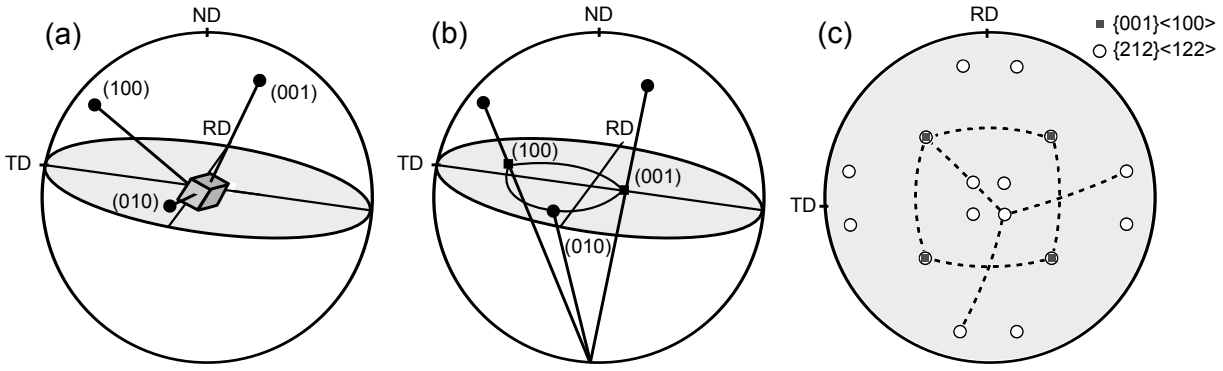

Figure 10.3: (a) Cubic crystal in the unit sphere with the {100} poles, (b) {100} poles of a cubic crystal in the stereographic projection onto the equator plane [89]. Schematic {111} pole figure in (c) showing the positions of the ideal {001}<100> and {212}<122> orientations [97].

A stereographic projection can be made from that reference point onto the equator plane (see Fig. 10.3(b)). This enables a simple two dimensional orientation representation known as a *pole figure*. A schematic {111} pole figure is presented in Fig. 10.3(c) and includes the positions of the ideal {001}<100> and {212}<122> orientations.

In-plane and out-of-plane texture characterization

The in-plane texture can be measured using XRD and detecting the diffraction intensity during an in-plane rotation, ϕ, about a certain pole (e.g. <111> for nickel) as shown in Fig. 10.4(a). The resulting diffraction intensity typically follows a Gaussian distribution at the pole and reflects the variation in alignment between the crystallographic planes of the grains in the sample. The pole figure represents the *in-plane texture*. XRD ϕ-scans of two poles, (111) and (200), are typically used in order to evaluate in-plane cube texture [11].

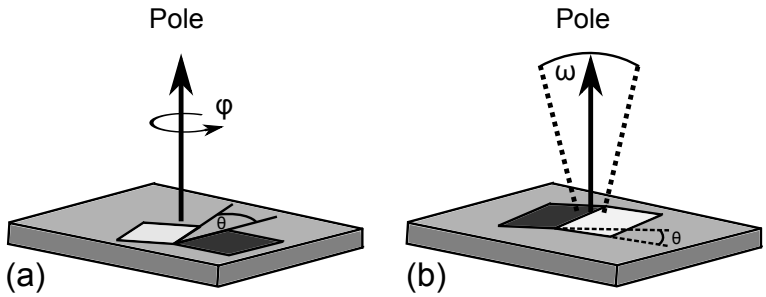

Figure 10.4: (a) In-plane texture measurement using a pole figure scan (b) out-of-plane texture measurement using a rocking curve scan.

Out-of-plane texture is a measure of how well the directions normal to the planes are aligned in a polycrystalline material. This can be measured by rocking the sample along a pole perpendicular to the planes (e.g. <200> for nickel) as shown in Fig. 10.4(b). The strength of both in-plane and out-of-plane textures are evaluated by the full width at half maximum (FWHM) values, $\Delta\phi$ and $\Delta\omega$, respectively. A strong texture is characterized by a small FWHM value [89]. A qualitative evaluation of misorientations cannot be obtained using the XRD technique. Such information may however be obtained using the EBSD technique, which can probe the local microtexture in a material [89,103].

Chapter 11

Appendix - B

This appendix contains additional information on specific topics discussed in the thesis.

11.1 Intermediate and two-step annealing

An intermediate annealing step may be inferred before the material is cold-rolled to the final thickness and typically at a thickness of 3 mm. This annealing step is for example performed on Ni-5at.%W tapes using an annealing temperature of 850 ^{o}C for 45 min [40]. This heat treatment promotes a partial release of the energy stored in the material during rolling which results in a partial recovery and following decrease in strain of the tape. The Ni tape is thus softer and easier to cold-roll to the final thickness while the grain size is refined [104]. Note that the final rolling from 3 mm to 80 μm result in a total thickness reduction, TTR > 97%, which is sufficient in order to obtain a strong recrystallisation cube {001}<100> texture during annealing in Ni-5at.%W [40].

Several authors [61, 99] have reported an increased fraction of cube texture in Ni-based substrates when applying a two-step annealing, e.g. 700 ^{o}C for 30 min and then ramping to 1000 ^{o}C and annealing for 30 min compared with a single heat treatment at 1000 ^{o}C for 2 hours.

11.2 IBAD and ISD textured templates

The main purposes of buffer layers (in the RABiTS approach) are to prevent chemical reactions between the metal substrate and the RE-BCO layer, to transfer or even improve morphology and texture, and to accommodate lattice misfits [11,28]. Buffer layers are generally metal-oxides and many different buffer layer systems have been developed [11,56].

Opposite to the buffer layers formed on textured metal tapes, where texture is transferred, a strong bi-axial texture must be formed in the buffer layer(s) in both the IBAD and ISD technique. Such buffer layers are produced using vacuum chambers and physical vapour deposition (PVD) techniques.

Ion Beam Assisted Deposition

Pulsed laser deposition, ion-beam or magnetron sputtering, is used in the IBAD technique to deposit buffer layer material (e.g. YSZ, MgO or TiN) on a smooth metal tape simultaneously with a heavy ion (Ar^{+}) bombardment of the substrate surface [11,55] as shown in Fig.11.1(a).

During growth of the thin film, molecules arrive at the substrate material and combine into unit cells with various orientations. Simultaneously, the ion beam removes unit cells with undesired orientations and only unit cells with a preferred (e.g. {001}<100>) orientation remain on the substrate material. This selective grain growth mechanism generates a strong bi-axial

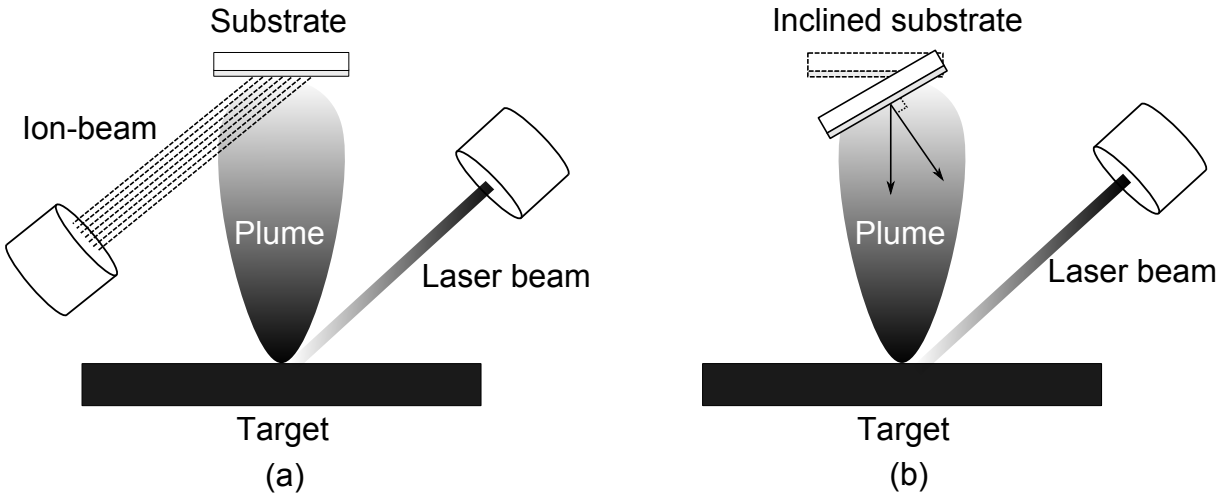

Figure 11.1: Drawing of the IBAD technique (a) and the ISD technique (b).

texture in the buffer layer and is characterised by low FWHM values $\Delta\phi$=5-7^o and $\Delta\omega$=7-15^o, even though the substrate is randomly oriented. Very high J_C values, >1·10^6 A/cm^2, have been achieved in YBCO films deposited by PLD on such IBAD templates [11].

Of course, the process description given hear is very schematic and the IBAD technique is inevitably very sensitive to growth parameters such as ion-to-molecule arrival ratio, the ion beam incident angle and the substrate temperature. Some of the main challenges, in terms of large scale production, are in-situ texture monitoring, metal tape surface roughness and production time/output ratio. However, advantages such as a very strong texture and small grain size (∼50 nm) are unique for the IBAD technique. Furthermore, Groves et al. [105] reported that the time/output ratio could be improved remarkably by utilising MgO instead of standard YSZ, since a significantly thinner layer (few nanometers) is needed in order to form a strong cube texture in MgO compared with micrometers in YSZ thus drastically reducing deposition times.

It is encouraging that IBAD is being employed commercially by Superpower Inc [41] producing kilometer lengths of coated conductors with a minimum I_C = 300 A/cm-width using IBAD and Metal-Organic Chemical Vapour Deposition (MOCVD), for MgO buffer layers and YBCO layer, respectively.

Inclined substrate deposition

An alternative geometry is used in the ISD technique as compared with the deposition geometry of a standard PLD setup, see Fig.11.1(b). Generally, e-beam evaporation is applied for MgO layers while PLD is used to deposit YSZ in the ISD technique. By tilting the substrate at a certain angle with respect to the target, a ∼1μm layer bi-axially textured is readily grown with one axis tending to be parallel to the path of the plasma and one axis tending to be perpendicular to the substrate surface (see arrows in Fig. 11.1(b)). A columnar morphology is apparent in the buffer layer due to this tilting, which may be explained by a self-shadowing effect [11]. The columns in e.g. MgO, are tilted with an angle of 25^o with respect to the substrate normal. High growth rates (∼ 500 nm/min) are a requirement since more than 1 μm thick buffer layers are needed to form a sufficiently strong texture.

Balachandran et al. [106] reported a $J_C \approx 2{\cdot}10^5$A/cm^2 at 77 K and self-field for YBCO layers deposited on an ISD-MgO buffered Hastelloy tape. The buffer layer stack was characterised by an in- and out-of-plane misorientation with $\Delta\phi$=9.2^o and $\Delta\omega$=5.4^o, respectively.

11.3 Demagnetisation

A ferromagnetic material in an applied magnetic field will produce a demagnetisation field (H_d) that is related to the divergence of **M** and it depends on the material geometry. The divergence of **M** is given by $\nabla\cdot\mathbf{H} = -\nabla\cdot\mathbf{M}$ and the magnetisation therefore stops abruptly at the surface as if magnetic monopoles are present [62]. For example, in the case of a flat plane with the magnetisation parallel to the plane, see Fig. 11.2(a), no magnetic monopoles are created as they are supposed to be infinite distance away.

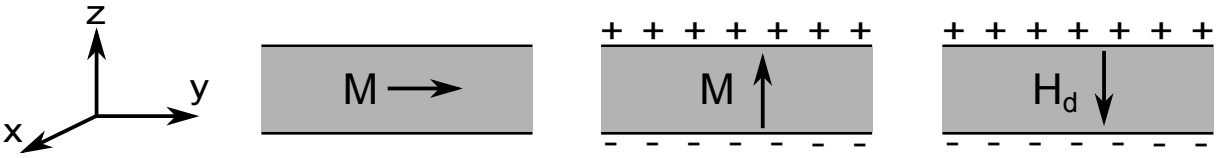

Figure 11.2: (a) Ferromagnetic sample with the magnetisation lying in the plane, (b) the magnetisation perpendicular to the plane which produces positive and negative magnetic poles at the surface and (c) the resulting demagnetisation field, H_d [62].

However, when the magnetic monopoles are closer they due produce an appreciable magnetic field, see Fig. 11.2(b) and (c). The resulting **H**-field is thus given by $\mathbf{H}_i$=$\mathbf{H}_a$-N**M**, where N is the demagnetisation tensor which for a plane is equal to $N_x = N_y = 0$ and $N_z = 1$.

11.4 Reel-to-reel chemical solution deposition

Long strongly textured metal tapes are to be coated on both sides simultaneously in a reel-to-reel system using a cost effective deposition technique in the larger research project as shown in Fig. 11.3.

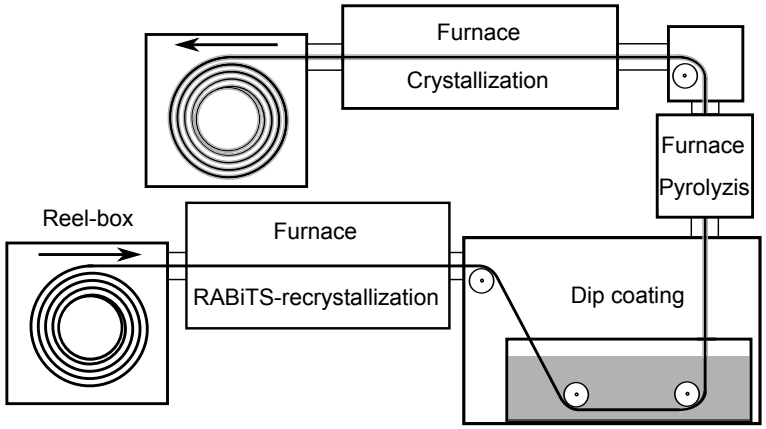

Figure 11.3: A reel-to-reel system for annealing of the RABiTS and deposition of buffer or superconductor layers using dip coating.

Two different CSD techniques are currently being investigated in the larger research project; metal-organic decomposition (MOD) and polymer-based Sol-Gel, which have previously been successfully applied to produce single side coated $>1{\cdot}10^6$ A/cm^2 YBCO films on RABiTS [11]. Simultaneous double-side coating with MOD, or Sol-Gel, can be performed using dip coating. An example of a reel-to-reel buffer layer coating cycle is; The cold rolled metal tape is recrystallised at $\sim$1000^{o}C, dip coated with buffer layer material at room temperature, pyrolysed at $\sim$500^{o}C and the buffer layer is finally crystallised at 1025^{o}C in well controlled atmospheres, such as argon.

Chapter 12

Appendix - C

12.1 Authored papers of the thesis

[**A1**] A.C. Wulff , Y. Zhao, O.V. Mishin , J.-C.Grivel, "Effect of Initial Surface Quality on Final Roughness and Texture of Annealed Ni-5at.%W Tapes Coated with a $Gd_2Zr_2O_7$ Buffer Layer", J. Supercond. Nov. Magn. (2012) 25:475-479.

[**A2**] A.C. Wulff, O.V. Mishin, J.-C. Grivel, "Topographic changes in Ni-5at.%W substrate after annealing under conditions of buffer layer crystallization", Phys. Proc. 36 (2012) 1423-8.

[**A3**] A.C. Wulff, O.V. Mishin, J.-C. Grivel, "Evolution of microstructure, texture and topography during additional annealing of cube-textured Ni-5at.%W substrate for coated conductors", J. Alloy. Comp. 539 (2012) 161-7.

[**A4**] A.C. Wulff, O.V. Mishin, N.H. Andersen, Y. Zhao, J.-C. Grivel, "Microstructure, texture and magnetic properties of new Ni-Cu-W substrates for coated conductors", Mater. Lett. 92 (2013) 386-388.

J Supercond Nov Magn (2012) 25:475–479
DOI 10.1007/s10948-011-1303-5

ORIGINAL PAPER

Effect of Initial Surface Quality on Final Roughness and Texture of Annealed Ni-5at.%W Tapes Coated with a $Gd_2Zr_2O_7$ Buffer Layer

A.C. Wulff · Y. Zhao · O.V. Mishin · J.-C. Grivel

Received: 27 July 2011 / Accepted: 24 August 2011 / Published online: 21 September 2011

Abstract Surface roughness of Ni-5at.%W tapes in cold-rolled and annealed conditions after subsequent deposition of a $Gd_2Zr_2O_7$ buffer layer has been studied as a function of the polishing grade, taking grain boundary grooving into account. It is found that annealing decreases the initial mean surface roughness achieved by mechanical polishing of the cold-rolled material, except after very fine polishing. Furthermore, compared to the surface of the tape annealed after fine polishing, the mean roughness slightly increases after the deposition of the buffer layer. Grain boundary grooving was found to impose a lower limit for the mean surface roughness. In the annealed tapes, the fraction of orientations within 5° from the ideal cube orientation was observed to be very sensitive to the surface roughness before annealing.

Keywords Ni-5at.%W substrates · $Gd_2Zr_2O_7$ buffer layer · Mechanical polishing · Surface roughness · Cube texture

1 Introduction

In the past decade, there have been a lot of efforts to increase production efficiency for the second generation of high-temperature superconducting (HTS) coated conductors [1–4]. The reel-to-reel production of ceramic superconducting layers, e.g., $YBa_2Cu_3O_{7-\delta}$ (YBCO), on top of a buffered textured metal substrate is one of the promising methods for efficient and low-cost production of long HTS tapes [5–8].

A.C. Wulff (✉) · Y. Zhao · O.V. Mishin · J.-C. Grivel
Materials Research Division, Risø National Laboratory for Sustainable Energy, Technical University of Denmark, 4000 Roskilde, Denmark
e-mail: anwu@risoe.dtu.dk

To enable high critical currents, the microstructure of the highly anisotropic superconducting YBCO layer should consist of grains with as small misorientations as possible, i.e., the material should be strongly textured. Therefore, a strong cube {001}<100> texture is initially generated in the Ni-based substrate by a combination of heavy rolling and annealing, and subsequently transferred via a buffer layer to the superconducting YBCO layer. In this architecture, the buffer layer is introduced to prevent the diffusion of metal ions from the substrate into the YBCO layer and to decrease the lattice mismatch between the substrate and the YBCO layer [9]. The resulting quality of coated conductors fabricated using the Ni-alloy substrate technique is highly dependent on the microstructure and surface quality of the buffer layer that, in turn, are affected by the surface quality of the substrate [10–12]. Therefore, it is important to consider how the surface roughness of the substrate tape changes during processing.

Since the processing of very long tapes may involve polishing of the substrate before annealing, we have chosen to monitor changes of the surface roughness of a Ni-5.at%W tape mechanically polished using different polycrystalline diamond suspensions. It is pertinent to mention that although substrate polishing is not necessary when rolls are well polished [13], additional polishing of the cold-rolled tape may be required when rolls become somewhat worn. Furthermore, the roughness of both the annealed tape and a coated $Gd_2Zr_2O_7$ buffer layer is also analyzed in the present work. Thus, surface requirements for the given substrate before annealing and the resulting surface roughness of the coated buffer layer can be established. Such surface requirements are of great importance for the reel-to-reel production of coated conductors. In addition, the effect of differing surface roughness of the cold-rolled tape on the fraction of the cube texture formed during annealing is investigated in

this work using the electron backscatter diffraction (EBSD) technique.

2 Experimental

2.1 Material

2.1.1 Ni-5at.%W Substrate

A Ni-5at.%W ingot was prepared by arc melting of 99.99% pure metals. The obtained ingot was homogenized at 1050 °C for 65 hours and hot forged into a rectangular shape of 10 × 17 × 50 mm, applying 0.5-mm thickness reductions per stroke. At least 1-mm-thick surface layer containing oxides was removed mechanically. The material was then cold rolled using mirror-finished rolls, with reductions of <5% per pass to a final thickness of 140 μm, thus giving a total thickness reduction of 98%. Four 10 × 30 mm specimens cut from the metal tape were mechanically polished using different Struers polycrystalline diamond suspensions with a diamond grain size (DGS) of 15, 9, 3, or 0.25 μm. The tapes were subsequently annealed in a quartz tube furnace with 350 mL/min flow of 5% H_2 in N_2 at 1020 ± 20 °C for 75 min. This annealing treatment resulted in recrystallized microstructures with an average grain size of ∼20 μm (including twins).

2.1.2 $Gd_2Zr_2O_7$ Buffer Layer

Gadolinium (III) 2,4-pentadionate and zirconium (IV) 2,4-pentadionate with stoichiometric proportions, as starting reagents, were dissolved in propionic acid (CH_3CH_2COOH). A fully reacted solution with a transparent light yellow color was obtained after stirring the solution on a hot plate at 60 °C for more than two hours. The total cationic concentration of the precursor solution was 0.6 mol/L. The annealed Ni-5at.%W tapes were coated using the dip coating technique with a withdrawal speed of 20 mm/min. The coated films were crystallized in a quartz tube furnace at 1050 °C with a heating rate of 8 °C/min and with a reducing atmosphere of 5% H_2 in Ar. The thickness of the buffer layer was characterized by ellipsometry to be between 30 and 50 nm.

2.2 Characterization

Crystallographic orientations of the grains were measured using the EBSD technique. In each annealed sample, several different regions with a total area of 4–6 mm^2 were mapped to obtain statistical texture information. Surface topography and roughness were characterized by atomic force microscopy (AFM) in contact mode. At least two regions, each with an area of 30 × 30 μm, were scanned by AFM in the middle of each specimen. Nonlinear artefacts due to the AFM scanner exceeding its linear scanning regime were treated using the standard data correction as described by Bonnell and Huey [14]. The arithmetic surface roughness (R_a) was used in this work to characterize the mean roughness since the former parameter is less susceptible to height variations in the inspection plane compared with the root mean square roughness and thus also reducing effects from residual nonlinear artefacts [14, 15]. For the setup used in the present experiment, the experimental uncertainty of the measurement technique is 1–2 nm [16].

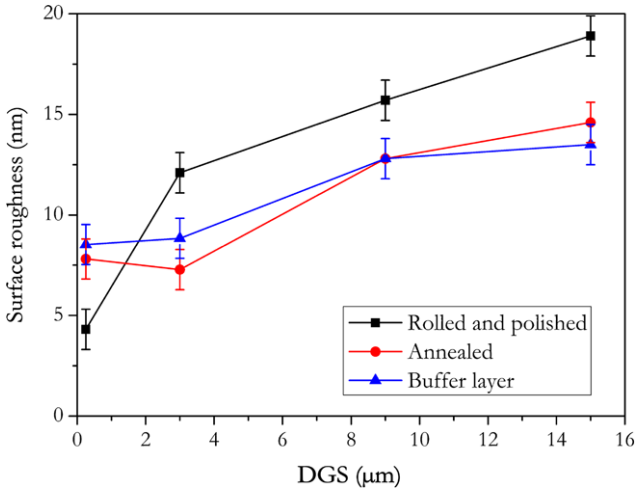

Fig. 1 Arithmetic surface roughness of the tapes as a function of DGS. The error bars correspond to the experimental uncertainty of the measurement technique (see Sect. 2.2)

3 Results and Discussion

3.1 Surface Roughness

Surface roughness of the cold-rolled tapes polished using different polishing suspensions are shown in Fig. 1. The roughness appears to be directly proportional to the DGS in the range 3–15 μm. The roughness is however reduced drastically reaching ∼4 nm for DGS = 0.25 μm.

Annealing made the surface of the DGS = 3–15 μm tapes smoother (see Fig. 1). For example, the surface roughness of the tape polished using the greatest DGS decreased from 19 nm to ∼15 nm after annealing. A similar reduction in roughness caused by surface diffusion [17] is seen for the DGS = 3 and 9 μm tapes. However, for the tape polished using the finest DGS, the roughness increased after annealing. The different effects of annealing can be rationalized considering the microstructure of the annealed samples. SEM images (Fig. 2) show evidence of thermal grain boundary grooving in these samples [17–19]. Apparently, in the samples with significant roughness, smoothening of scratches

due to surface diffusion was more effective than roughening due to boundary grooving. In the sample with the lowest mean roughness, effects of grain boundary grooving were no longer counterbalanced by the smoothening effects, which resulted in increased surface roughness, compared to that in the rolled and polished condition. In fact, the roughness of the annealed DGS = 0.25 μm sample became similar to that in the annealed DGS = 3 μm sample (see Fig. 1). Thus, it is evident that the finest polishing of the cold-rolled substrate tape is not beneficial, with respect to the surface roughness after annealing, because boundary grooving during subsequent annealing degrades the quality of the finely polished surface. To illustrate the detrimental effect of the boundary grooving, several AFM line scans (Fig. 3) were conducted on the annealed DGS = 0.25 μm sample, where grain boundary depths were found to range from 15 to 59 nm. This range is similar to that reported by Zhu et al. [12] for commercial Ni-5at.% substrates.

As follows from the data in Fig. 1, an average roughness of about 8 nm may be the lowest obtainable roughness value for a mechanically polished Ni-5at.%W tape annealed at 1050 °C, as grain boundary grooving imposes a lower limit for the surface roughness.

The roughness of the buffer layer is not significantly different from that of the annealed tapes (see Fig. 1). Some increase in the mean roughness of the buffer layer on the DGS = 0.25 and 3 μm tapes could, for example, be caused by further thermal etching of the substrate grain boundaries in the buffer layer [9].

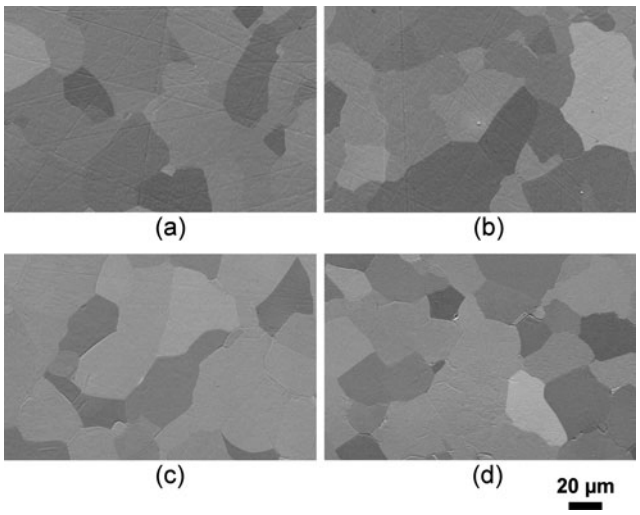

Fig. 2 SEM images showing the surface of the Ni-5at.%W tapes annealed after mechanical polishing using different DGS: (**a**) 15 μm; (**b**) 9 μm; (**c**) 3 μm; and (**d**) 0.25 μm

3.2 Cube Texture in the Annealed Samples

Strong cube {001}<100> textures were obtained in the annealed tape samples. A fragment of a large EBSD map from the annealed DGS = 0.25 μm tape is shown in Fig. 4a, where different colors correspond to orientations with different deviations from the ideal {001}<100> orientation (see Fig. 4b, c). In this sample, almost 60% of all orientations deviate by less than 5°, and 99% are within 15° from the ideal cube orientation. Orientations, represented by blue pixels in Fig. 4a, belong to the {212}<122> component and are thus twin-related to the {001}<100> component [20, 21] (see Fig. 4c).

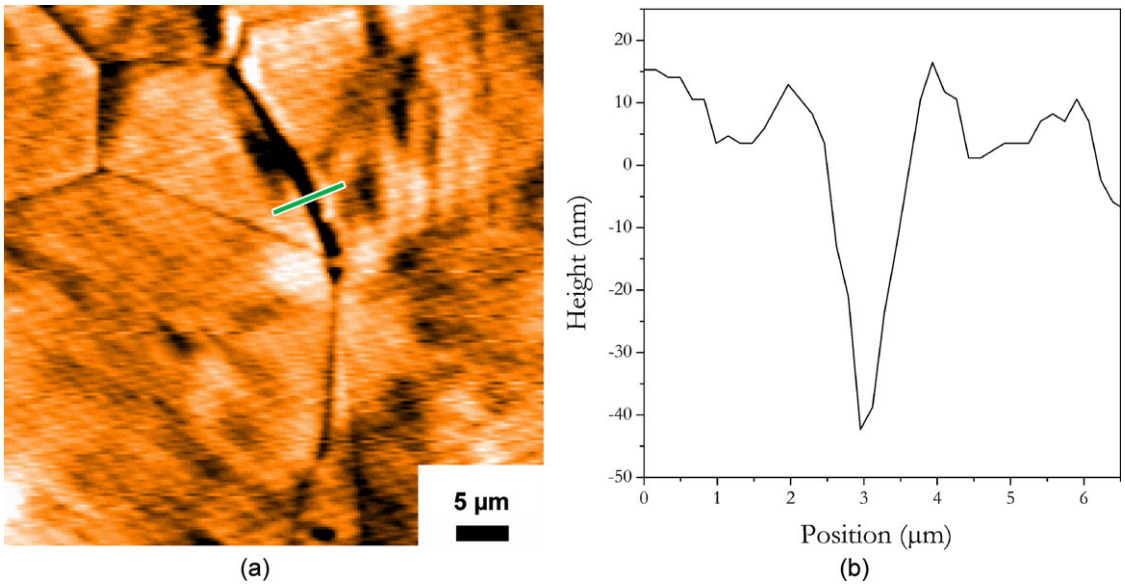

Fig. 3 Example of AFM image and a line scan profile: (**a**) an AFM image of the annealed DGS = 0.25 μm tape. A scan along the *gray line* (*green* in the online version) is made to sample the height profile shown in (**b**). It is seen in (**b**) that the profile changes dramatically at a grain boundary

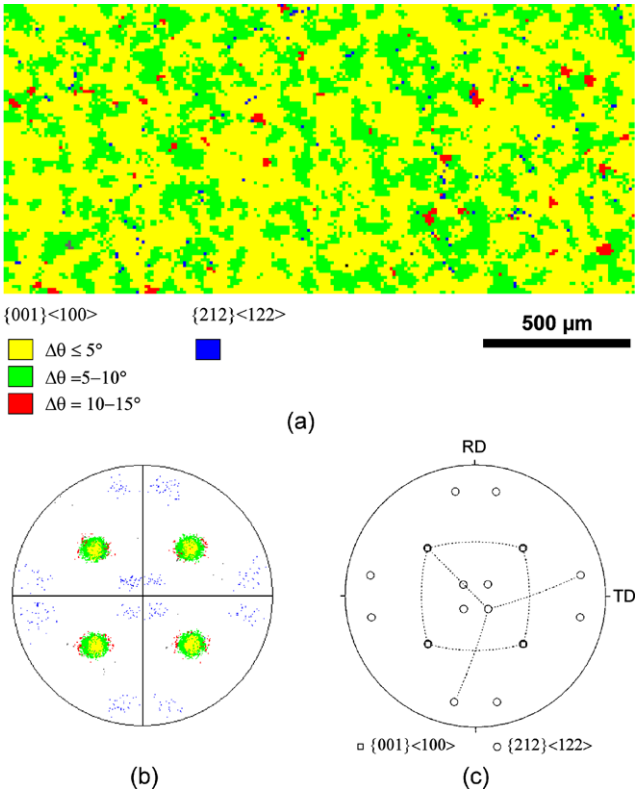

Fig. 4 Example of EBSD data for the annealed DGS = 0.25 μm tape: (**a**); fragment of a big EBSD map used for texture analysis; (**b**) {111} pole figure showing orientations from the region in (**a**); and (**c**) positions of the ideal {001}<100> and {212}<122> orientations in the {111} pole figure [21]

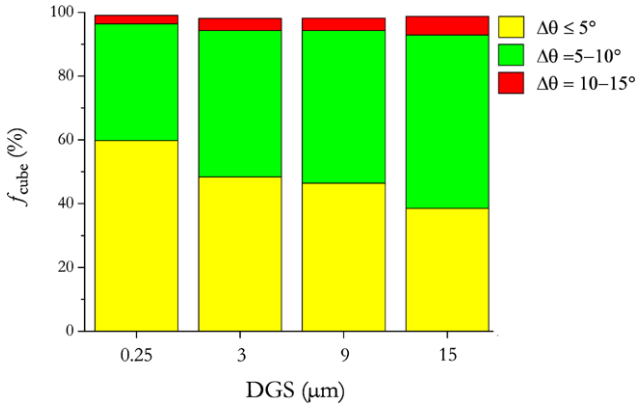

Fig. 5 Area fraction of the cube texture in the annealed Ni-5at.%W tapes as a function of DGS and deviation $\Delta\theta$ from the ideal {001}<100> orientation

Changes in the area fraction of the cube texture component for different deviations $\Delta\theta$ from the ideal {001}<100> orientation are quantified for each sample in Fig. 5. These results show that whereas the fraction of the cube texture component for $\Delta\theta \leq 15°$ does not appear to depend on the surface conditions before annealing, the fraction of orientations very close ($\Delta\theta \leq 5°$) to the ideal cube orientation is remarkably sensitive to the DGS value. The absolute difference in the area fraction of such orientations between the DGS = 0.25 and 15 μm tapes is 21% (see Fig. 5). This result demonstrates the importance of the surface roughness in the cold-rolled condition on the sharpness of the cube texture developed during subsequent annealing. Considering the fact that the decreased fraction of the nearly ideal cube orientations well correlates with the greater surface roughness of the tapes before annealing (Fig. 1), it is reasonable to suggest that deep scratches may have affected the orientation range of successful recrystallization nuclei in the heavily rolled material.

4 Conclusions

1. A series of heavily cold-rolled Ni-5at.%W tapes were polished, annealed and subsequently coated with a $Gd_2Zr_2O_7$ buffer layer. For cold-rolled samples that were polished using suspensions with a diamond grain size of at least 3 μm, annealing considerably reduced the mean roughness of the tapes. Finer polishing using DGS = 0.25 μm was not beneficial, because boundary grooving during annealing deteriorated the quality of the finely polished surface. A lower limit of the mean surface roughness of the given Ni-5at.%W tapes after annealing was found to be ∼8 nm.
2. The sharpness of the cube texture formed in the annealed tapes was sensitive to the surface roughness before annealing. The fraction of orientations within 5° from the ideal cube orientation increased with decreasing DGS and, hence, with decreasing surface roughness obtained by mechanical polishing of the cold-rolled substrate.

Acknowledgements The authors gratefully acknowledge Mr. J.S. Bang for technical assistance with mechanical polishing and Mr. O. Trinhammer for valuable discussions of AFM measurements. This work was supported by the Danish Ministry of Science, Technology and Innovation under contract number 09-065234.

References

1. Goyal, A., Norton, D.P., Budai, J.D., Paranthaman, M., Specht, E.D., Kroeger, D.M., Christen, D.K., He, Q., Saffian, B., List, F.A., Lee, D.F., Martin, P.M., Klabunde, C.E., Hatfield, E., Sikka, V.K.: Appl. Phys. Lett. **69**, 1795 (1996)
2. Sathyamurthy, S., Paranthaman, M., Bhuiyan, M.S., Payzant, E.A., Lee, D.F., Goyal, A., Li, X., Kodenkandath, T., Schoop, U., Rupich, M.: IEEE Trans. Appl. Supercond. **15**, 2974 (2005)
3. Paranthaman, M., Chirayil, T.G., Sathyamurthy, S., Beach, D.B., Goyal, A., List, F.A., Lee, D.F., Cui, X., Lu, S.W., Kang, B., Specht, E.D., Martin, P.M., Kroeger, D.M., Feenstra, R., Cantoni, C., Christen, D.K.: IEEE Trans. Appl. Supercond. **11**, 3146 (2001)
4. Yamada, Y., Ibi, A., Fukushima, H., Takahashi, K., Miyata, S., Kuriki, R., Kobayashi, H., Konishi, M., Kato, T., Hirayama, T., Shiohara, Y.: IEEE Trans. Appl. Supercond. **17**, 3371 (2007)
5. Malozemoff, A.P., Fleshler, S., Rupich, M., Thieme, C., Li, X., Zhang, W., Otto, A., Maguire, J., Folts, D., Yuan, J., Kraemer,

H.P., Schmidt, W., Wohlfart, M., Neumueller, H.W.: Supercond. Sci. Technol. **21**, 7 (2008)
6. Li, Y., Zhao, Z., Liu, L., Ye, Q., Zheng, H.: IEEE Trans. Appl. Supercond. **19**, 3295 (2009)
7. Hanyu, S., Tashita, C., Hanada, Y., Hayashida, T., Morita, K., Sutoh, Y., Igarashi, M., Kakimoto, K., Kutami, H., Iijima, Y., Saitoh, T.: Supercond. Sci. Technol. **23**, 4 (2010)
8. Miura, M., Yoshizumi, M., Izumi, T., Shiohara, Y.: Supercond. Sci. Technol. **23**, 8 (2010)
9. Je, J.H., You, H., Cullen, W.G., Maroni, V.A., Ma, B., Koritala, R.E., Rupich, M.W., Thieme, C.L.H.: Physica C **384**, 54 (2003)
10. Steffens, M., Falter, M., Bäcker, M., Oligschleger, C.: J. Phys. Conf. Ser. **97**, 012165 (2008)
11. Varesi, E., Celentano, G., Petrisor, T., Boffa, V., Ciontea, L., Galluzzi, V., Gambardella, U., Mancini, A., Rufoloni, A., Vannozzi, A.: Supercond. Sci. Technol. **16**, 498 (2003)
12. Zhu, S., Liu, L., Xu, D., Liu, H., Song, X., Hong, D., Ying, W., Li, Y.: J. Supercond. Nov. Magn. **24**, 1869 (2011)
13. He, Q., Christen, D.K., Budai, J.D., Specht, E.D., Lee, D.F., Goyal, A., Norton, D.P., Paranthaman, M., List, F.A., Kroeger, D.M.: Physica C **275**, 155 (1997)
14. Bonnell, D.A., Huey, B.D.: In: Bonnell, D.A. (ed.) Scanning Probe Microscopy and Spectroscopy, 2nd edn. Wiley, New York (2001)
15. Gadelmawla, E.S., Koura, M.M., Maksoud, T.M.A., Elewa, I.M., Soliman, H.H.: J. Mater. Process. Technol. **123**, 133 (2002)
16. Nanosurf AG: Operating Instructions, EasyScan 2 AFM, v. 1.3 (2005)
17. Truchan, T.G., Rountree, F.H., Lanagan, M.T., McClelian, S.M., Miller, D.J., Goretta, K.C., Tamsic, M., Foley, R.: IEEE Trans. Appl. Supercond. **10**, 1130 (2000)
18. Zhao, Y., Suo, H., Liu, M., Liu, D., Zhang, Y., Zhou, M.: Physica C **440**, 10 (2006)
19. de Boer, B., Eickemeyer, J., Reger, N., Fernandez, L., Richter, G.-R.J., Holzapfel, B., Schultz, L., Prusseit, W., Berberich, P.: Acta Mater. **49**, 1421 (2001)
20. Mishin, O.V.: Scr. Mater. **38**, 423 (1998)
21. Mishin, O.V.: J. Mater. Sci. **33**, 5137 (1998)

Available online at www.sciencedirect.com

SciVerse ScienceDirect

Physics Procedia 36 (2012) 1423 – 1428

Physics Procedia

Superconductivity Centennial Conference

Topographic changes in Ni-5at.%W substrate after annealing under conditions of buffer layer crystallization

A.C. Wulff *, O.V. Mishin, J.-C. Grivel

Materials Research Division, Risø National Laboratory for Sustainable Energy, Technical University of Denmark, DK-4000 Roskilde, Denmark

Abstract

Topographic changes have been studied in an annealed Ni-5at.%W substrate with a strong cube texture before and after additional annealing reproducing conditions of buffer layer crystallization. It was found that during this additional annealing the microstructure slightly coarsened and that the average depth of grain boundary grooves increased considerably for certain boundary types. Grooves at general high angle boundaries and Σ3 boundaries with large deviations from the ideal twin relationship were found to be more sensitive to the additional heat-treatment than grooves at low angle and true twin boundaries. Average groove widths increased for all boundary types. Despite the observed changes in the extent of grain boundary grooving, the mean surface roughness was almost identical before and after the additional annealing.

Keywords: Ni-5at.%W; annealing; topography; grain boundary grooving; grain boundary misorientation

1. Introduction

Over the past decade, significant efforts have been made to increase the efficiency and quality of the coated conductors, also known as the second generation of high temperature superconductors. These conductors are fabricated using strongly textured Ni-based substrates coated with a number of ceramic buffer layers (e.g. Y_2O_3/ YSZ/CeO_2) and a superconducting $YBa_2Cu_3O_{7-\delta}$ layer. The surface roughness of

* Corresponding author
E-mail address: anwu@risoe.dtu.dk

1875-3892
doi:10.1016/j.phpro.2012.06.147

the substrate is an important parameter that should be controlled to enable good surface quality of the final superconducting tape. The mean surface roughness of the annealed substrate does not only depend on the surface roughness of the tape in the cold-rolled condition [1], but is also affected by thermal grain boundary (GB) grooving [2]. Whereas the roughness of the substrate is measured in the delivery condition, topographic changes may occur during further processing used to fabricate superconducting tapes. For example, crystallization of the buffer layers [3,4] usually involves temperatures higher than those applied for recrystallization annealing of the heavily rolled material, which can modify the surface conditions of the substrate. The aim of this work is to characterize topographic changes during annealing that reproduces the heat-treatment used for buffer layer crystallization. In the present experiment, atomic force microscopy (AFM) is combined with the electron backscatter diffraction (EBSD) technique to relate grain boundary grooving to crystallographic characteristics of grain boundaries.

2. Experimental

2.1. Material and processing

A Ni-5at.%W ingot was prepared by arc melting of 99.99% pure metals. The obtained ingot was homogenized at 1025°C for 87 hours and hot forged into a rectangular shape of 8×12×97 mm, using 0.5 mm thickness reductions per stroke. The resulting oxide formed on the surface was removed mechanically. The material was then cold-rolled using mirror-finished rolls, applying < 5% reductions per pass. The final thickness of the rolled tape was 120 μm, which corresponds to a total thickness reduction of 98 %. The tape was then recrystallized during annealing in a protective atmosphere of 5% H_2 in N_2 at 1000°C for 2 hours. Several samples were further annealed in the protective atmosphere at 1025°C for 1 hour, i.e. under conditions that are frequently used for crystallization of a ceramic buffer layer [3,4].

2.2. AFM characterization

The surface topography was investigated using both AFM and scanning electron microscopy (SEM). AFM characterization was conducted in contact mode scanning over ~17,000 μm^2 in several regions, where scans were made after annealing at 1000°C and again after annealing at 1025°C in the same regions. Non-linear artifacts due to the AFM scanner exceeding its linear scanning regime were treated using the standard data correction [5]. The arithmetic surface roughness was used in this work to characterize the mean roughness taking grain boundary grooving into account. When considering the geometry of GB grooves, the groove depth was defined as the distance from the groove root to the maxima and the groove width was measured between the maxima on either side of the groove root [6]. The depth and width of GB grooves were compared before and after the additional annealing at boundaries that did not migrate during this additional heat treatment. Analysis of GB grooves at other (migrating) boundaries that did not only create new GB grooves, but also left grooves behind in the interior of coarsened grains, will be presented elsewhere.

2.3. EBSD analysis

The EBSD technique was used for analyzing misorientations across grain boundaries and for measuring the average grain size. High angle grain boundaries (HAGBs) were defined as boundaries between grains with misorientations greater than 15°. Low angle grain boundaries (LAGBs) were defined as boundaries between grains with misorientations 1.5 – 15°. Based on a previous work on copper [7], twin boundaries were classified as Σ3 boundaries with a deviation from the ideal 60°<111>

misorientation, $\Delta\theta < 3°$. These twin boundaries could also be clearly identified in the microstructure based on their morphological features. Boundaries formed between twins and non-matrix cube-oriented neighbors [8], and satisfying Brandon's criterion [9] for the Σ3 misorientation with large ($\Delta\theta = 3 - 8.66°$) deviations from the ideal twin relationship are termed "*other* Σ3 boundaries" in this work.

3. Results

The microstructure obtained after annealing at 1000°C is characterized by a small average grain size, 25 μm (including annealing twins), and a very strong cube {001}<100> texture. Narrow annealing twins within cube-oriented grains belong to the {212}<122> component. The fraction of LAGBs identified by EBSD in this microstructure was above 80%.

An SEM image and a corresponding EBSD map from a small region are shown in Fig 1. In the EBSD map (Fig 1b), LAGBs and HAGBs are shown by gray and black lines, respectively. Red lines correspond to twin boundaries, and blue lines show *other* Σ3 boundaries with large deviations from the ideal twin relationship. The latter boundaries are formed between twins and neighboring grains slightly disoriented from the matrix grain. This situation is typically observed when grain growth occurs in a strongly textured material containing annealing twins [8,10]. Inspection of Fig 1 reveals that grooves at coherent twin boundaries (CTBs) are less prominent than grooves at any other boundary type. Whereas very little grooving was also seen at boundaries with misorientations less than 5°, grooving at other LAGBs was more significant. Deep grooves typically developed at general HAGBs, incoherent twin boundary (ITB) segments and *other* Σ3 boundaries (see Fig 1a).

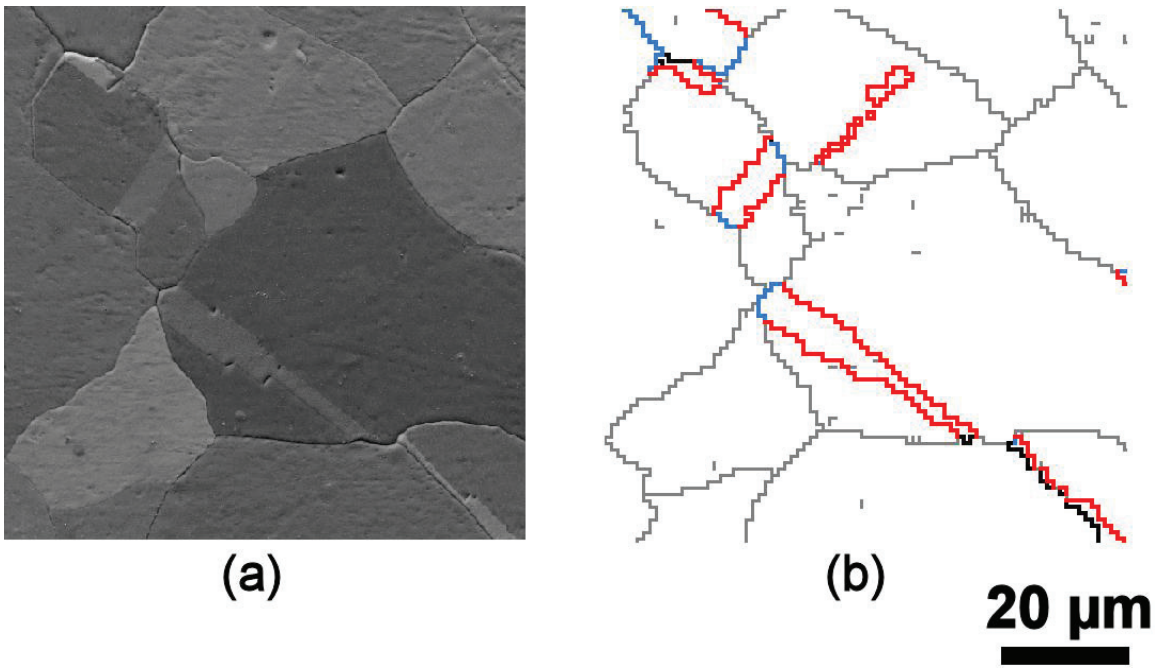

Fig. 1. Different boundary types in the microstructure annealed at 1000°C for 2 h: (a) SEM image and (b) EBSD map from the same region. In (b) low angle (1.5–15°) misorientations and general HAGBs are shown by gray and black lines, respectively. Red lines correspond to twin Σ3 boundaries ($\Delta\theta < 3°$) and blue lines show *other* Σ3 boundaries with larger deviations $\Delta\theta = 3 – 8.66°$ from the ideal twin relationship.

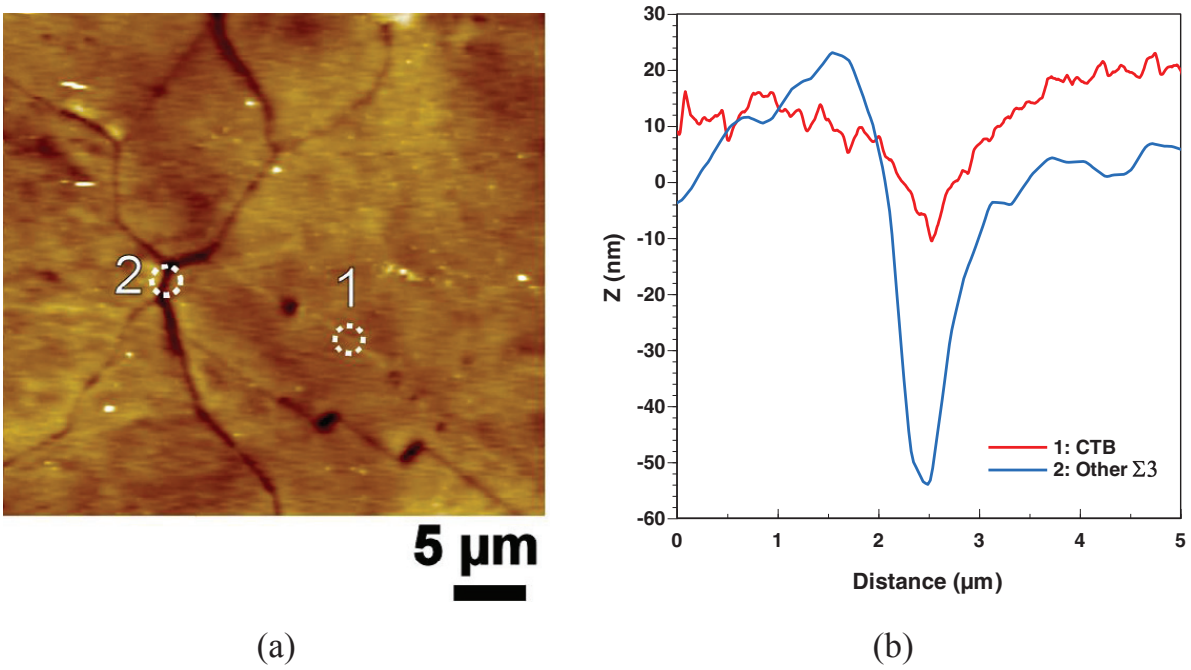

Fig. 2. AFM data for the region in Fig 1: (a) AFM micrograph where the marks "1" and "2" correspond to CTB and *other* Σ3 boundaries, respectively. (b) Profiles along line scans for these two boundaries.

An AFM micrograph from the region sampled in Fig 1 is presented in Fig 2a. To illustrate the difference between two different Σ3 boundary types, GB profiles were analyzed across boundaries marked "1" and "2" in Fig 2a. These two boundaries are classified in our work as either coherent twin or *other* Σ3 boundaries. From Fig 2b it is apparent that GB grooves at these two boundaries are very different, i.e. that the groove at the CTB is shallower than the groove at the *other* Σ3 boundary.

Average depths of grooves at 34 stationary boundaries in several regions are given in Fig 3a. It is seen that the smallest average groove depth was recorded for CTBs, followed by LAGBs. *Other* Σ3 boundaries and ITB segments demonstrated deeper grooves than the former two boundary types. Note that since ITB segments were very short, it was difficult to unambiguously determine, based on the available micrographs, whether short ITB segments were truly stationary, i.e. whether they stayed exactly in the same positions before and after the additional annealing. Therefore, parameters of grooves at ITB segments are not included in Fig 3. Considering all measured boundaries, general HAGBs were characterized by the greatest average groove depth.

Additional annealing at 1025°C resulted in a slightly larger average grain size, 29 µm, compared to that in the initial recrystallized substrate. AFM analysis of GB grooving at the same boundaries before and after the additional heat treatment indicated that the average groove depth did not significantly change for LAGBs and CTBs. However, for *other* Σ3 boundaries and especially for HAGBs the average groove depths increased considerably (see Fig 3a). The additional annealing also resulted in increased groove widths for all boundary types (Fig 3b).

The mean surface roughness of the substrate before and after additional annealing was found to be 10.7 and 10.3 nm, respectively.

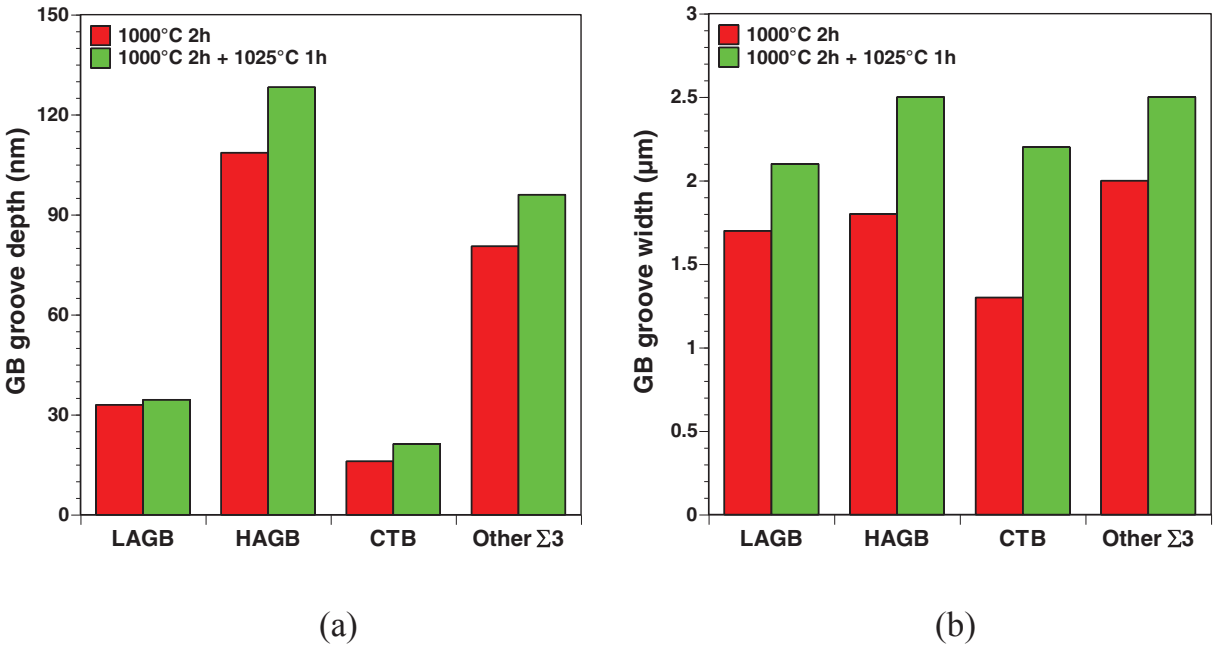

Fig. 3. Average parameters of GB groove depths (a) and widths (b) recorded from AFM data for 34 stationary boundaries before and after additional annealing.

4. Discussion

The results obtained in the present experiment demonstrate that additional heat treatment at 1025°C for 1 h alters the microstructure of the annealed Ni-5at.%W substrate. Although the additional annealing treatment was comparatively short and the temperature was only slightly higher than the temperature used for preparing the initial condition, the mean grain size has increased. Also, average depths of GB grooves at general HAGBs and *other* Σ3 boundaries increased considerably compared to those in the initial substrate (see Fig 3a). It is expected that such a substantial increase in GB grooving at these boundaries during additional annealing can be diminished either by reducing the annealing temperature below 1025°C or by decreasing the duration of annealing to < 1 h.

It is significant that in both annealed conditions HAGBs and Σ3 boundaries with large deviations for the ideal twin relationship, on average, developed deeper grooves than CTBs and LAGBs, which reflects differences in structural parameters of the different boundary types. It is therefore not surprising that a large scatter in the depth of groves at Σ3 boundaries has been obtained in several studies, where correlations between the extent of thermal grooving and GB misorientation (Σ-value) were studied [11,12]. Since boundary planes for coherent and incoherent twin boundaries are different and since other non-twin boundaries can also satisfy the generous Brandon criterion for the Σ3 misorientation, it is reasonable to distinguish between different kinds of Σ3 boundaries when linking the extent of various annealing phenomena to the boundary type.

Interestingly, despite the fact that GB grooves at general HAGBs and *other* Σ3 boundaries became much deeper after the additional annealing, no significant increase was observed for the mean surface roughness. It should be noted that the summed fraction of boundaries within the two groups that demonstrated substantially increased groove depths after annealing at 1025°C for 1 h was only 7% and, therefore, deeper grooves at these boundaries could not appreciably increase the mean surface roughness

compared to that in the initial substrate. It can be suggested that for the given heat-treatment the roughening effects due to increased grooving at certain boundaries could effectively be counterbalanced by diffusional smoothening of the surface [2].

5. Conclusions

1. Different boundary types in the annealed Ni-5at.%W substrate were grooved to a different extent. The smallest average depth was recorded for coherent twin boundaries, followed by low angle grain boundaries. Incoherent twin boundary segments and Σ3 boundaries with large deviations from the ideal 60°<111> relationship demonstrated deeper grooves than the former two boundary types. General high angle boundaries were characterized by the greatest average groove depth.

2. Additional annealing at 1025°C for 1 h slightly coarsened the microstructure. Comparison of groove parameters before and after this additional annealing at 34 stationary boundaries revealed that the average depth increased substantially for grooves at high angle boundaries and Σ3 boundaries with large deviations from the ideal twin misorientation. Changes in the average groove depth recorded for the other boundary types were less significant. Average groove widths increased for all boundary types. Despite the observed changes in the extent of grain boundary grooving, the mean surface roughness was almost identical before and after the additional annealing.

Acknowledgements

This work was supported by the Danish Ministry of Science, Technology and Innovation under contract number 09-065234. The authors gratefully acknowledge Dr. Y. Zhao and Mr. O. Trinhammer for valuable discussions of AFM measurements.

References

[1] Wulff AC, Mishin OV, Grivel J-C. *J Supercond Nov Magn* 2012; DOI: 10.1007/s10948-011-1303-5.

[2] Truchan TG, Rountree FH, Lanagan MT, McClellan SM, Miller DJ et al. *IEEE Trans Appl Supercond* 2000;**10**:1130–3.

[3] Aslanoglu Z, Akin Y, El-Kawni MI, Sigmund W, Hascicek YS. *Physica C* 2003;**384**:501–6.

[4] Zhao Y, Grivel J-C, Abrahamsen AB, Pavlopoulos D, Bednarcik J, von Zimmermann M. *IEEE Trans Appl Supercond* 2011;**21**:2912–5.

[5] Bonnell DA, Huey BD. In: Bonnell DA, editor. *Scanning Probe Microscopy and Spectroscopy*, 2nd edn, New York: Wiley; 2001, p.32–42.

[6] Mullins WW, Shewmon PG. *Acta Metall* 1959;**7**:163–70.

[7] Mishin OV, Huang X. *Mater Sci Forum* 1999;**294**–**296**:401–4.

[8] Mishin OV, *J Mater Sci* 1998;**33**:5137–43.

[9] Brandon DC, *Acta Metall* 1966;**14**:1479–84.

[10] Mishin OV, Gottstein G, *Mater Sci Eng* 1998;**A249:**71–8.

[11] Gladstone TA, Moore JC, Wilkinson AJ, Grovenor CRM. *IEEE Trans Appl Supercond* 2001;**11**:2923–6.

[12] Skidmore T, Buchert RG, Juhas MC, *Scripta mater* 2004;**50**:873–7.

Journal of Alloys and Compounds 539 (2012) 161–167

Contents lists available at SciVerse ScienceDirect

Journal of Alloys and Compounds

journal homepage: www.elsevier.com/locate/jalcom

Evolution of microstructure, texture and topography during additional annealing of cube-textured Ni–5at.%W substrate for coated conductors

A.C. Wulff [a,*], O.V. Mishin [b], J.-C. Grivel [a]

[a] Department of Energy Conversion, Technical University of Denmark, DK-4000 Roskilde, Denmark
[b] Section for Materials Science and Advanced Characterization, Department of Wind Energy, Technical University of Denmark, DK-4000 Roskilde, Denmark

ARTICLE INFO

Article history:
Received 14 March 2012
Received in revised form 4 June 2012
Accepted 6 June 2012
Available online 15 June 2012

Keywords:
Ni–W alloys
RABiTS
Annealing
Cube texture
Thermal grooving
Boundary migration

ABSTRACT

Microstructure, texture and topography have been studied in a recrystallized Ni–5at.%W substrate before and after additional annealing at 1025°C for 1 h. The initial recrystallized material contained a strong cube texture and a high fraction of low angle grain boundaries. Σ3 boundaries were also frequent in this substrate, including both coherent and incoherent twin boundary segments as well as non-twin Σ3 boundaries formed between twins and non-matrix neighbors of the cube texture component. A strong correlation between the boundary type and the average depth of grain boundary grooves was observed in this material. The smallest average groove depth was obtained for coherent twin boundaries, followed by low angle boundaries. Significantly greater average groove depths were found for the other boundary types. A similar correlation was also observed between the boundary type and the average inclination angle of groove walls. The additional annealing resulted in grain growth, texture strengthening and an increase in the fraction of low angle boundaries. Also, changes were observed in the extent of thermal grooving studied in the same regions before and after the additional annealing. Groove depths increased for a large number of stationary boundaries, whilst the majority of migrating boundaries developed shallower grooves compared to those before the additional annealing.

1. Introduction

Significant efforts have been made in the past two decades to increase the quality and efficiency of coated conductors, i.e. the second generation of high temperature superconducting tapes [1–8]. One method for manufacturing coated conductors utilizes a rolling assisted biaxially textured substrate (RABiTS) process to produce a strongly textured tape that is subsequently coated with a series of ceramic buffer layers and, finally, with a superconducting layer. In particular, this method has been applied for producing strongly textured Ni–W substrates coated with appropriate buffer layers and a superconducting $YBa_2Cu_3O_{7-\delta}$ (YBCO) layer [2–11]. The quality of such superconducting tapes greatly depends on the sharpness of the crystallographic texture, grain boundary (GB) misorientation distribution and surface conditions of the substrate material [2–13]. Since grain boundaries with misorientations greater than 10° dramatically decrease the critical current density of the epitaxially grown YBCO layer [7], the fraction of such boundaries in the substrate must be as low as possible. In the RABiTS process, the latter is achieved by annealing of a heavily rolled material to obtain a microstructure where most grains have orientations of the cube {001}⟨100⟩ texture. Surface roughness can be minimized either through the use of well polished rolls or by polishing of the substrate [12]. Excessive thermal grooving [14] should also be avoided by selecting appropriate heat-treatments.

It should be noted that the structural parameters and surface conditions of the annealed substrate may change during further processing. For example, crystallization of buffer layers [13,15] may be performed at higher temperatures than those used to anneal the substrate, which will likely increase the extent of GB grooving and may also modify the microstructure and texture of the substrate. These changes will inevitably affect characteristics of the buffer layer and, eventually, of the YBCO superconducting layer [8,13]. It is apparent that further optimization of the processing parameters for coated conductors requires an improved understanding of these changes.

In a previous communication we reported our preliminary results describing topographic changes in a recrystallized Ni–5at.%W substrate during additional annealing simulating conditions of a buffer layer crystallization process [16]. In the present work, these changes are considered in more detail, including analysis of groove depths for stationary and migrating boundaries. Also, the effect of the additional annealing on the boundary population and texture of the Ni–5at.%W substrate is characterized. A number of different techniques including atomic force microscopy

* Corresponding author.
E-mail address: anwu@dtu.dk (A.C. Wulff).

0925-8388/$ - see front matter © 2012 Elsevier B.V. All rights reserved.
http://dx.doi.org/10.1016/j.jallcom.2012.06.033

Fig. 1. Schematics defining the depth d and inclination angles β of the groove.

(AFM), scanning electron microscopy (SEM) and electron backscatter diffraction (EBSD) are applied to monitor changes in the same regions before and after additional annealing.

2. Experimental

2.1. Material

A Ni–5at.%W ingot was prepared by arc melting of 99.99% pure metals. The ingot was homogenized at 1025 °C for 87 h and hot forged into a rectangular shape with dimensions $8 \times 12 \times 97\ mm^3$, applying 0.5 mm thickness reduction per stroke. Following this hot deformation, the surface was polished mechanically to remove the oxide layer. The material was then cold rolled using mirror-finished rolls and applying less than 5% reduction per pass to a final thickness of 120 μm (98% total reduction). The sample was annealed in a protective atmosphere of 5% H_2 in N_2 at 1000 °C for 2 h. This annealed condition is referred in the present work to as condition A1. The sample was then additionally annealed in the protective atmosphere at 1025 °C for 1 h (condition A2). This temperature is within the range of that frequently used for buffer layer crystallization [13,15–18]. It is pertinent to mention that no evidence of secondary recrystallization was found in the given sample even when additional annealing was conducted at 1100 °C for 1 h. Vickers microhardness was measured in the annealed samples using a load of 200 g with a 15 s dwell time.

2.2. SEM/EBSD analysis

A field emission gun scanning electron microscope Zeiss Supra 35 was used for taking SEM images and for EBSD measurements (HKL Technology, Channel 5). Crystallographic texture was measured using the EBSD technique with a step size of 10 μm and covering an area of at least 5 mm^2 in the rolling plane. The fraction of the cube texture component was determined considering orientations within 10° from the ideal {001}⟨100⟩ orientation. A step size of 1–2 μm was applied for collecting smaller maps used for measuring grain size and GB misorientations. Because of the limited angular resolution of the EBSD technique, misorientations less than 1.5° were ignored in the EBSD maps. A misorientation threshold of 10° was used in the present work to distinguish between low angle grain boundaries (LAGBs) that do not dramatically affect the critical current density in the YBCO layer and high angle boundaries that substantially decrease it [7].

2.3. AFM analysis

Based on the features observed in the EBSD maps and corresponding SEM images, several regions containing different boundary types were selected for AFM analysis. The surface topography was characterized in these regions in contact mode using a Nanosurf easyScan 2 system, scanning over more than 17,000 μm^2 with a step size of 0.2 μm. Artifacts resulting from the AFM scanner exceeding its linear regime were treated using the standard data correction [19]. GB grooves were included in the roughness analysis and the arithmetic surface roughness was used to characterize the mean roughness. Following the approach described in Ref. [20], the groove depth d was measured as the distance from the groove root to the top of the groove wall (see Fig. 1). For asymmetric grooves, for which the heights of two walls were different, d was measured at the higher wall. To obtain a value characterizing the depth of an individual groove, the data were averaged over several AFM line scans across each groove. In addition, inclination angles β at the groove root (see Fig. 1) were determined from the AFM data and it was typically found that β_1 and β_2 were not identical.

3. Results

3.1. Annealed condition A1

The A1 condition contained a strong cube texture (see Fig. 2), where the area fraction of the cube component f_{cube} within 10° from the ideal {001}⟨100⟩ orientation was 96% (see Table 1). Most of the remaining area was occupied by grains with slightly greater deviations from the ideal cube orientation and by {212}⟨122⟩ twins in the cube-oriented matrix (Fig. 2). The microstructure was fully recrystallized with an average grain size of 25 μm (including annealing twins) and contained a high fraction of LAGBs, see Fig. 3. The fraction of boundaries with misorientations $\theta < 10°$ in the EBSD maps was 68%.z

The total fraction of Σ3 boundaries was measured to be 14%. This figure comprises true twin boundaries and non-twin Σ3 boundaries formed between annealing twins and non-matrix neighbors with orientations similar to that of the matrix grain (Fig. 4). Previous misorientation measurements in copper have shown that true twin boundaries are always characterized by small ($\Delta\theta < 3°$) deviations from the exact 60° ⟨111⟩ misorientation [21,22], whereas a wide range of deviations allowable by Brandon's criterion [23] are obtained for Σ3 boundaries between {212}⟨122⟩ twins and non-matrix cube-oriented neighbors [22]. Therefore, in

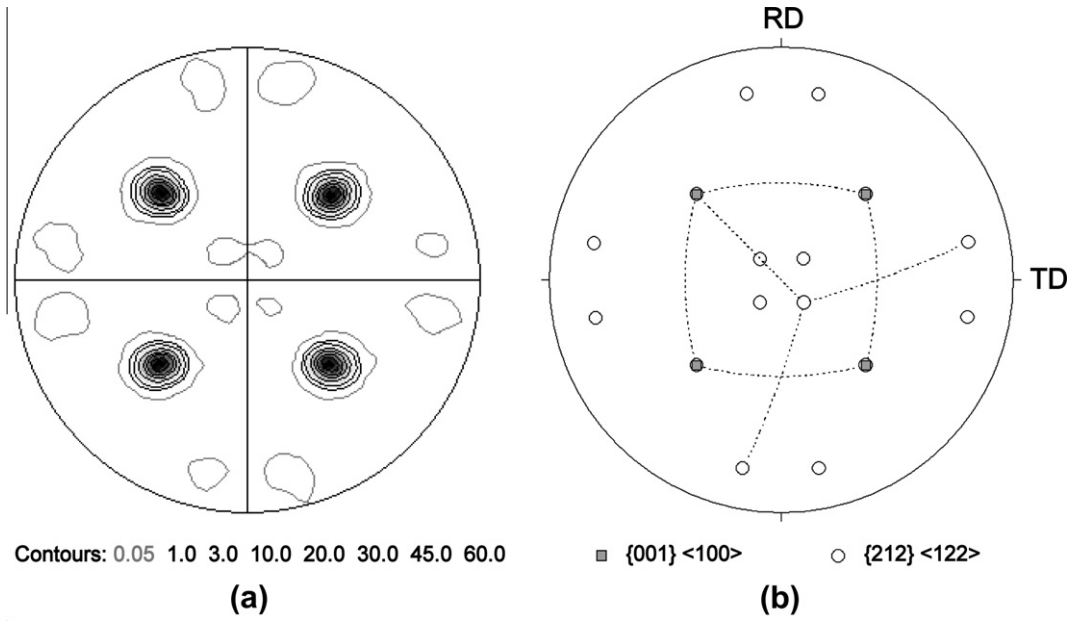

Fig. 2. Texture in the A1 condition: (a) {111} pole figure, (b) positions of the ideal {001}⟨100⟩ and {212}⟨122⟩ orientations [22]. Note the low intensity (gray contour) of the {212}⟨122⟩ orientations in (a).

Table 1
Parameters describing the microstructure, texture, surface roughness (S_A) and hardness (HV) of the Ni–5at.%W substrate in conditions A1 and A2.

Condition	Grain size (μm)	f_{cube} (%)	Fraction of boundaries (%)				$L_{A\ (\theta > 10°)}$ (μm^{-1})	S_A (nm)	HV
			$\theta < 10°$	$\theta > 10°$ except Σ3	Σ3 $\Delta\theta < 3°$	Σ3 $\Delta\theta = 3 - 8.66°$			
A1	25	96	68	18	10	4	2.0×10^{-2}	10.7	142
A2	28	97	72	17	7	4	1.5×10^{-2}	10.3	142

the EBSD maps analyzed in our work a distinction was made between Σ3 boundaries characterized by either $\Delta\theta < 3°$ or $\Delta\theta = 3 - 8.66°$ (see Fig. 4). The former included predominantly true twin boundaries and a small number of non-twin Σ3 boundaries with misorientations close to the exact 60° ⟨1 1 1⟩ relationship.

Inspection of the surface revealed grooves at grain boundaries (see Fig. 5a). The smallest average values of the groove depth were recorded for coherent twin boundaries (CTBs), followed by low angle ($\theta < 10°$) boundaries (see Fig. 6a). Boundaries with misorientations greater than 10°, incoherent twin boundary (ITB) segments and non-twin (NT) Σ3 boundaries had deeper grooves than the former two boundary types. A similar correlation was observed between the boundary type and angles characterizing inclinations of groove walls (Fig. 6b). The mean surface roughness S_A in the A1 condition was 10.7 nm (Table 1).

3.2. Additionally annealed condition A2

During additional annealing at 1025 °C for 1 h the average grain size increased from 25 to 28 μm, without affecting the hardness of the material (see Table 1). Grain growth was accompanied by a slight increase both in the area fraction of the cube texture and in the fraction of LAGBs (Fig. 3 and Table 1). To evaluate the overall change in the boundary network due to both the increased average grain size and reduced fraction of low angle boundaries, we considered the length of boundary traces per unit area L_A [24,25], taking into account all boundary types with misorientations above 10°. The $L_{A(\theta>10°)}$ values derived from the EBSD data were corrected for a stepped nature of inclined boundary traces in the EBSD maps [24]. It was found that $L_{A(\theta>10°)}$ decreased after the additional annealing from 2.0×10^{-2} to 1.5×10^{-2} μm^{-1} (see Table 1).

By inspecting the same regions in the A1 and A2 conditions it was possible to identify which boundaries migrated during the additional annealing and which boundaries did not change their surface positions (see Fig. 5). In the current study, these two groups of boundaries are referred to as migrating and stationary boundaries, respectively. No distinction between stationary and migrating boundaries was made for ITB segments because these segments were typically too short to determine unambiguously whether their positions had changed during the annealing.

GB grooves were analyzed at 48 stationary boundaries and 24 migrating boundaries before and after the additional annealing (see Fig. 7). Comparing the depths of individual grooves in the two conditions, it is evident that for the majority of stationary boundaries the groove depth increased during the additional annealing (see Figs. 7 and 8), where the greatest changes were seen for NT Σ3 boundaries (Fig. 8a). In contrast to the stationary boundaries, the migrating boundaries typically developed shallower grooves in the new positions (see Figs. 7 and 8). These changes are also reflected in the average values for the different boundary types (Fig. 9).

The migrating boundaries not only formed new GB grooves, but also left grooves in their previous positions (Fig. 5). On average, the depth of these abandoned grooves was ~25% less than the depth of the corresponding GB grooves in the A1 condition. The mean surface roughness was measured to be 10.3 nm in the A2 condition (Table 1).

4. Discussion

The present experiment demonstrates that annealing of a recrystallized Ni–5at.%W sample at 1025 °C for 1 h changes the

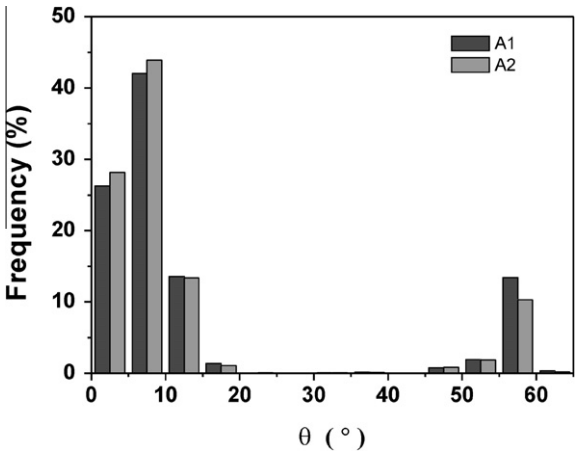

Fig. 3. Distribution of misorientation angles in the A1 and A2 conditions.

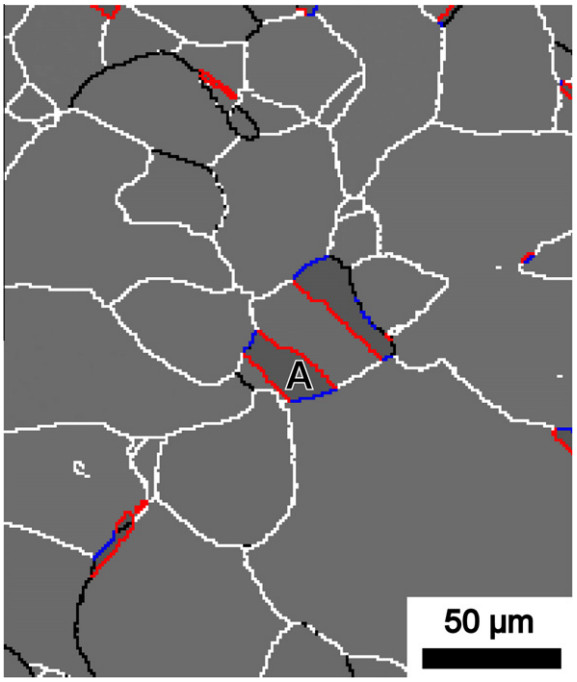

Fig. 4. A boundary map representing the microstructure in the A1 condition. In this map, 1.5–10° misorientations are shown by white lines. Boundaries with misorientations $\theta > 10°$ (except Σ3) are depicted by black lines. Σ3 boundaries characterized by small ($\Delta\theta < 3°$) and large ($\Delta\theta = 3 - 8.66°$) deviations from the exact twin relationship are shown in red and blue, respectively. The letter A is a reference label (see also Fig. 5). (For interpretation of the references to color in this figure legend, the reader is referred to the web version of this article.)

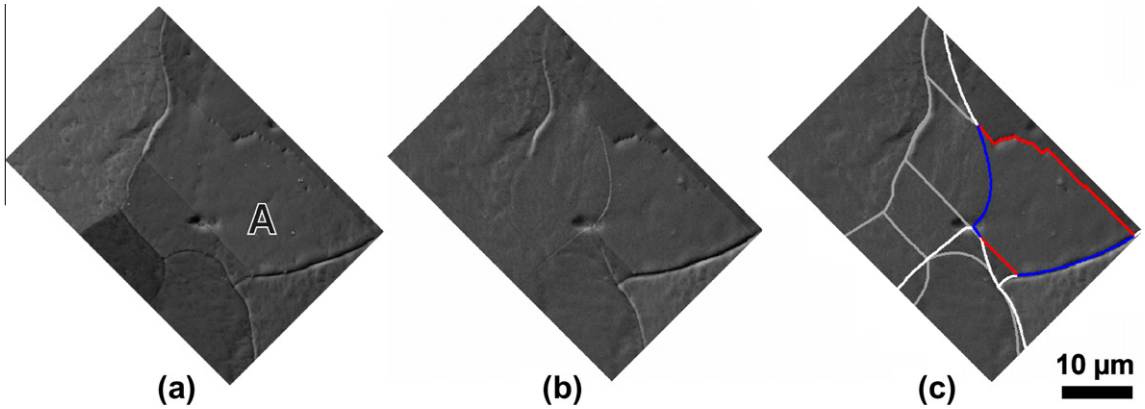

Fig. 5. SEM micrographs and a sketch illustrating different boundary types from a region in the center of Fig. 4, where the microstructure was analyzed before and after the additional annealing: (a) condition A1; (b,c) condition A2. In (c) superimposed lines indicate different boundary types. Low angle ($\theta < 10^{\circ}$) boundaries, true twin boundaries and non-twin Σ3 boundaries are shown by white, red and blue lines, respectively. Gray lines indicate positions of grain boundaries before the additional annealing. The abandoned grooves in these positions can be distinguished in (b). The letter A is a reference label (see also Fig. 4). (For interpretation of the references to color in this figure legend, the reader is referred to the web version of this article.)

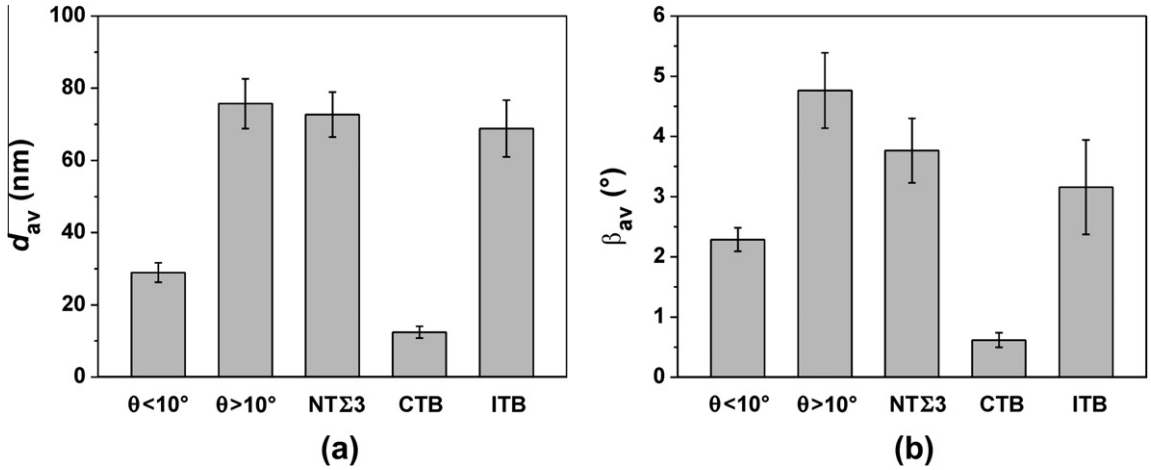

Fig. 6. Average parameters of GB grooves at different boundary types in the A1 condition: (a) depths d_{av}; (b) inclination angles β_{av} (see Fig. 1). Note that the group "$\theta > 10^{\circ}$" does not include any Σ3 boundaries. The error bars correspond to the standard error.

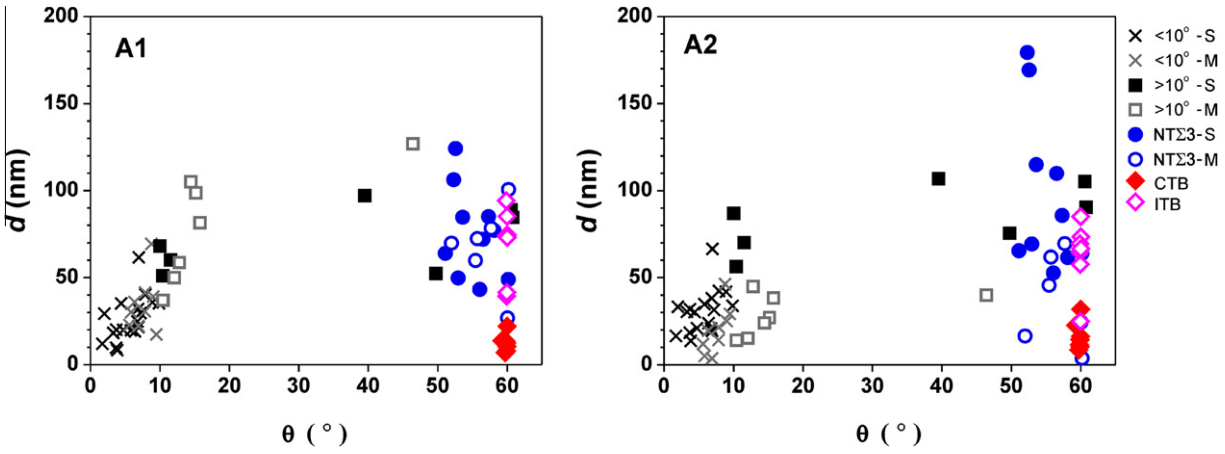

Fig. 7. Groove depths for different boundaries analyzed in the same regions of the A1 and A2 conditions. Letters "S" and "M" correspond to stationary and migrating boundaries, respectively. No distinction between stationary and migrating boundaries is made for ITBs.

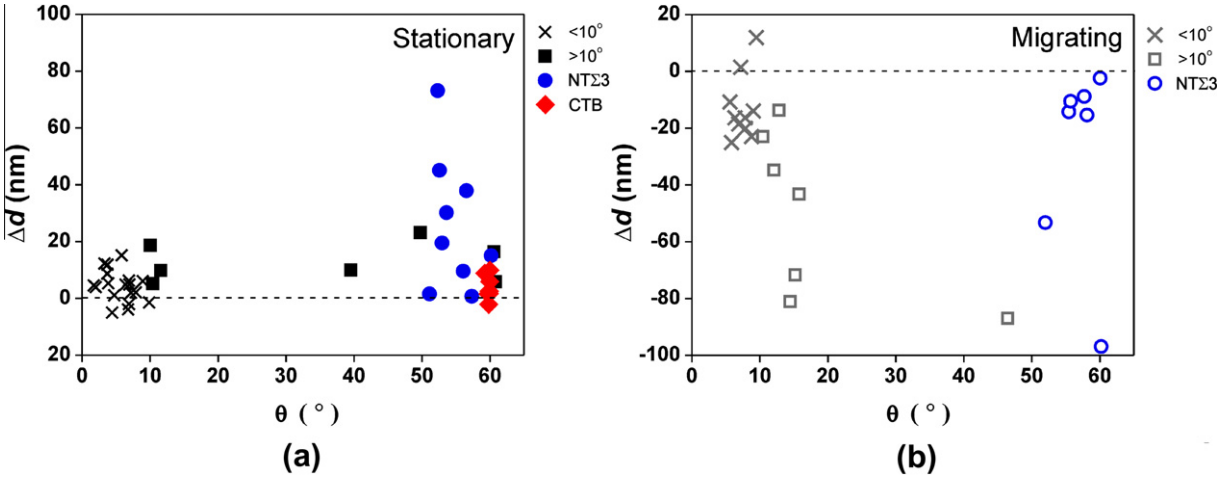

Fig. 8. The difference between depths of individual grooves at stationary (a) and migrating (b) boundaries in the A1 and A2 conditions ($\Delta d = d_{A2} - d_{A1}$).

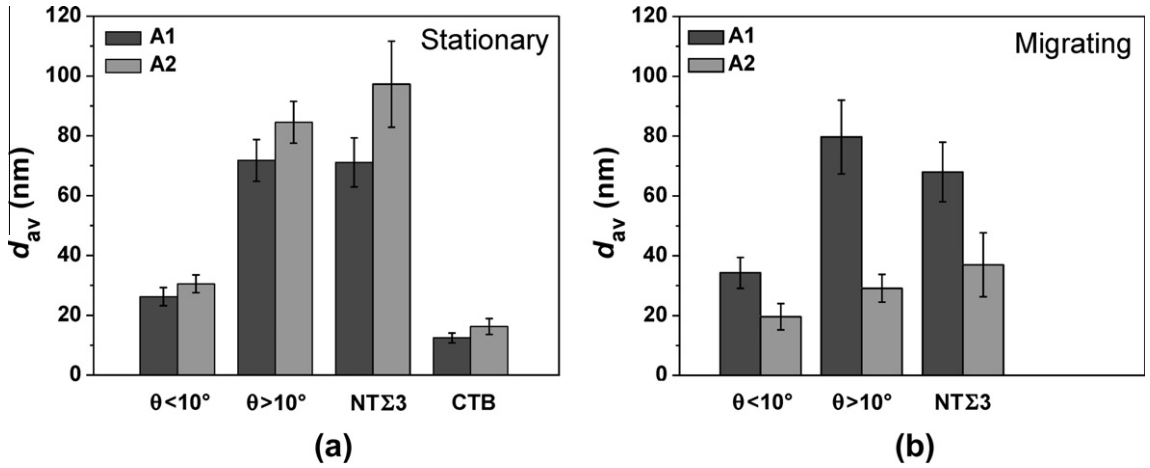

Fig. 9. Mean values of GB groove depths for stationary (a) and migrating (b) boundaries of different types. The group "$\theta > 10°$" does not include any Σ3 boundaries. The error bars correspond to the standard error.

microstructure, texture and topography of the sample. These changes are considered in the following.

4.1. Evolution of texture and grain boundary network

A strong cube texture is frequently formed during recrystallization of heavily rolled face centered cubic materials such as, for example, copper, nickel and aluminum. In the present work, the cube texture occupied approximately 96% of the total area of the Ni–5at.%W sample in the A1 condition. This is slightly lower than the fractions reported for the same alloy by Eickemeyer et al. [3,6], but similar to the values obtained by Chen et al. [26]. It should be noted that, in contrast to the substrates developed by Eickemeyer et al. [3,6], who applied either an extremely large (99.6%) total reduction or an intermediate annealing treatment in their processing schedule, the very strong texture was produced in the present work after a smaller total reduction and with no intermediate annealing.

In agreement with many previous reports, most boundary misorientations in our strongly textured material were very low. A significant fraction of boundaries with misorientations greater than 10° was however still present in the A1 condition. Interestingly, despite a very low intensity of the {2 1 2}⟨1 2 2⟩ component in this material (Fig. 2), Σ3 boundaries comprised a substantial fraction of the boundary network (Table 1). Apparently, this is due to the morphology of annealing twins seen in the microstructure. The twins are usually very narrow, but extended and contain multiple steps (facets) along twin boundaries, resulting in a significant total fraction of Σ3 boundaries in the EBSD maps.

While migration of boundaries with very low misorientations is restricted, boundaries with sufficiently large misorientations (except for coherent twin boundaries) can migrate over significant distances (see Fig. 5b), thus increasing the average grain size during further annealing at 1025 °C. During this process, grains oriented differently from the cube texture tend to shrink, increasing the fraction of the cube texture component, and new low angle boundaries are formed. The process of grain growth in the presence of the strong texture reduces the initial $L_{A(\theta>10°)}$ value by 25% (see Table 1). This suggests that an additional heat-treatment at 1025 °C of the investigated Ni–5at.%W substrate would not have a detrimental effect on the texture and boundary network in the final superconducting tape. On the contrary, as the microstructure coarsens and the fraction of low angle boundaries increases, the surface area of boundaries able to reduce the critical current density in the superconducting layer is expected to decrease compared to that in the initial condition.

4.2. Topographic changes

It is known that GB grooving may increase the overall surface roughness of Ni-based substrates [27]. Since the extent of GB grooving is sensitive to the boundary structure, special attention in this work was paid to the analysis of grooves at different boundary types. As expected, very shallow grooves were observed at low-energy LAGBs, in agreement with the data for cube-textured Ni and Ni–Cr substrates [28]. For these materials, Gladstone et al. [28] also reported a wide range of groove depths for Σ3 boundaries, which was attributed to mixing coherent and incoherent segments in their data set. This bias is avoided in the present experiment, where grooves at coherent and incoherent twin segments are analyzed separately along with a separate analysis of non-twin Σ3 boundaries. It is shown that grooves at both incoherent twin and non-twin Σ3 boundaries are typically much deeper than those at coherent interfaces, which reflects their different energies [29]. In fact, the d_{av} and β_{av} values for grooves at the former two boundary types approached the corresponding values for grooves at general boundaries with misorientation angles greater than 10° (see Fig. 6). It is therefore evident that for establishing a correlation between the boundary type and the extent of grooving, it is not sufficient to identify the boundary type solely based upon Brandon's criterion. The boundary plane and the presence of non-twin Σ3 boundaries should be taken into account to obtain an appropriate description of such correlations.

Furthermore, by separating stationary and migrating boundaries we were able to describe the changes in groove depth for these two groups of boundaries. We observed that for the majority of stationary boundaries the depth of grooves increased due to the higher temperature of the additional annealing. For a small number of boundaries in this group, the groove depth was found to decrease slightly (by 1–5 nm, see Fig. 8a). The reason for this unexpected reduction is not very clear at present. One possible explanation is that this reduction is due to the fact that locations, where groove profiles were analyzed across individual boundaries, were not absolutely identical.

Most of the migrating boundaries did not have enough time to develop deep grooves in their new positions and therefore became shallower after the additional annealing (see Fig. 8(b)). The average groove depths for the migrating boundaries were therefore much less compared to those before the additional annealing (Fig. 9b). The abandoned grooves observed behind the migrating boundaries (Fig. 5) also become shallower due to a healing process described by Mullins [14]. In our experiment, this process resulted in a 25% reduction in the average depth of the abandoned grooves.

Despite the changes observed in the extent of grooving, the mean surface roughness was almost unchanged (Table 1). This suggests that for the given heat-treatment the roughening effects due to increased grooving at some boundaries and due to appearance of new GB grooves were effectively counterbalanced by diffusional smoothing of the intragranular surface [27].

5. Conclusions

Microstructure, texture and topography have been studied in a strongly textured Ni–5at.%W substrate in the initial recrystallized condition and after additional annealing at 1025 °C for 1 h. The following conclusions were drawn.

1. A strong correlation between the average depth of grain boundary grooves and boundary type was observed in the initial condition. The smallest average groove depth was recorded for coherent twin boundaries, followed by low angle (<10°) grain boundaries. Significantly greater average GB groove depths were found for other boundary types. A similar correlation was also observed between the boundary type and the average inclination angle of groove walls.
2. The additional annealing resulted in a slight increase in the average grain size, texture strengthening and, as a result of this, an increased fraction of low angle grain boundaries. The total length of boundary traces with misorientations greater than 10° decreased by 25% as evaluated from the EBSD data.
3. During the additional annealing some boundaries did not move from their original positions, while other boundaries migrated. For the majority of stationary boundaries the groove depth increased compared to the values recorded before the additional annealing. In contrast, the migrating boundaries typically developed shallower GB grooves than those in the initial condition. The migrating boundaries also left grooves behind in the interior of the coarsened grains. The average depth of these abandoned grooves was ~25% less than the depth of the same grooves at grain boundaries before migration. The mean surface roughness was however almost unchanged.

Acknowledgements

This work was supported by the Danish Ministry of Science, Technology and Innovation under contract number 09-065234. The authors gratefully acknowledge Dr. Y. Zhao and Mr. O. Trinhammer for valuable discussions of AFM measurements.

References

[1] A. Goyal, D.P. Norton, J.D. Budai, M. Paranthaman, E.D. Specht, D.M. Kroeger, D.K. Christen, Q. He, B. Saffian, F.A. List, D.F. Lee, P.M. Martin, C.E. Klabunde, E. Hatfield, V.K. Sikka, Appl. Phys. Lett. 69 (1795) (1996) 1795–1797.
[2] J. Eickemeyer, D. Selbmann, R. Opitz, B. De Boer, B. Holzapfel, L. Schultz, U. Miller, Supercond. Sci. Technol. 14 (2001) 152–159.
[3] J. Eickemeyer, D. Selbmann, R. Opitz, H. Wendrock, E. Maher, U. Miller, W. Prusseit, Phys. C 372–376 (2002) 814–817.
[4] B. de Boer, J. Eickemeyer, N. Reger, L. Fernandez, J. Richter, B. Holzapfel, L. Schultz, W. Prusseit, P. Berberich, Acta Mater. 49 (2001) 1421–1428.
[5] S. Engel, K. Knoth, R. Hühne, L. Schultz, B. Holzapfel, Supercond. Sci. Technol. 18 (2005) 1385–1390.
[6] J. Eickemeyer, R. Hühne, A. Güth, C. Rodig, H. Klauß, B. Holzapfel, Supercond. Sci. Technol. 21 (2008) 105012.
[7] J.H. Durrell, N.A. Rutter, Supercond. Sci. Technol. 22 (2009) 013001.
[8] E. Varesi, G. Celentano, T. Petrisor, V. Boffa, L. Ciontea, V. Galluzzi, U. Gambardella, A. Mancini, A. Rufoloni, A. Vannozzi, Supercond. Sci. Technol. 16 (2003) 498–505.
[9] U. Schoop, M.W. Rupich, C. Thieme, D.T. Verebelyi, W. Zhang, X. Li, T. Kodenkandath, N. Nguyen, E. Siegal, L. Civale, T. Holesinger, B. Maiorov, A. Goyal, M. Paranthaman, IEEE Trans. Appl. Supercond. 15 (2005) 2611–2616.
[10] M.P. Paranthaman, X. Qiu, F.A. List, K. Kim, Y. Zhang, X. Li, S. Sathyamurthy, C. Thieme, M.W. Rupich, IEEE Trans. Appl. Supercond. 21 (2011) 3059–3061.
[11] R.I. Tomov, A. Kursumovic, M. Majoros, B.A. Glowacki, J.E. Evetts, A. Tuissi, E. Villa, M. Zamboni, Y. Sun, S. Tönies, H.W. Weber, Phys. C 383 (2003) 323–336.
[12] A.C. Wulff, Y. Zhao, O.V. Mishin, J.-C. Grivel, J. Supercond. Nov. Magn. 25 (2012) 475–479.
[13] K. Knoth, R. Hühne, S. Oswald, L. Schultz, B. Holzapfel, Acta Mater. 55 (2007) 517–529.
[14] W.W. Mullins, Acta Metal. 6 (1958) 414–427.
[15] Y. Zhao, J.-C. Grivel, A.B. Abrahamsen, D. Pavlopoulos, J. Bednarcik, M. von Zimmermann, IEEE Trans. Appl. Supercond. 21 (2011) 2912–2915.
[16] A.C. Wulff, O.V. Mishin, J.-C. Grivel, Phys. Procedia (2012), http://dx.doi.org/10.1016/j.phpro.2012.06.147.
[17] S. Sathyamurthy, M. Paranthaman, T. Aytug, B.W. Kang, P.M. Martin, A. Goyal, D.M. Kroeger, D.K. Christen, J. Mater. Res. 17 (2002) 1543–1549.
[18] M.S. Bhuiyan, M. Paranthaman, S. Sathyamurthy, T. Aytug, S. Kang, D.F. Lee, A. Goyal, E.A. Payzant, K. Salama, Supercond. Sci. Technol. 16 (2003) 1305–1309.
[19] D.A. Bonnell, B.D. Huey, in: D.A. Bonnell (Ed.), Scanning Probe Microscopy and Spectroscopy, 2nd edn., Wiley, New York, 2001, pp. 32–42.
[20] D.M. Saylor, G.S. Rohrer, J. Am. Ceram. 82 (1999) 1529–1536.
[21] O.V. Mishin, X. Huang, Mater. Sci. Forum 294–296 (1999) 401–404.
[22] O.V. Mishin, J. Mater. Sci. 33 (1998) 5137–5143.
[23] D.C. Brandon, Acta Metall. 14 (1966) 1479–1484.
[24] W.Q. Cao, A. Godfrey, Q. Liu, Mater. Sci. Eng., A 361 (2003) 9–14.
[25] O.V. Mishin, V.M. Segal, S. Ferrasse, Metal. Mater. Trans. A (2012), http://dx.doi.org/10.1007/s11661-012-1287-1.

[26] S.K. Chen, C.F. Liu, P.X. Zhang, L. Zhou, Mat. Sci. Forum 546–549 (2007) 1997–2002.
[27] T.G. Truchan, F.H. Rountree, M.T. Lanagan, S.M. McClelian, D.J. Miller, K.C. Goretta, M. Tamsic, R. Foley, IEEE Trans. Appl. Supercond. 10 (2000) 1130–1133.
[28] T.A. Gladstone, J.C. Moore, A.J. Wilkinson, C.R.M. Grovenor, IEEE Trans. Appl. Supercond. 11 (2001) 2923–2926.
[29] L.E. Murr, Interfacial phenomena in metals and alloys, Addison-Wesley Pub. Co., Reading, MA, 1975.

Materials Letters 92 (2013) 386–388

Contents lists available at SciVerse ScienceDirect

Materials Letters

journal homepage: www.elsevier.com/locate/matlet

Microstructure, texture and magnetic properties of Ni–Cu–W substrates for coated conductors

A.C. Wulff [a,*], O.V. Mishin [b], N.H. Andersen [c], Y. Zhao [a], J.-C. Grivel [a]

[a] Department of Energy Conversion and Storage, Technical University of Denmark, 4000 Roskilde, Denmark
[b] Section for Materials Science and Advanced Characterization, Department of Wind Energy, Technical University of Denmark, 4000 Roskilde, Denmark
[c] Department of Physics, Technical University of Denmark, 2800 Kgs. Lyngby, Denmark

ARTICLE INFO

Article history:
Received 10 August 2012
Accepted 2 November 2012
Available online 10 November 2012

Keywords:
Metal and alloys
Superconductors
Electron microscopy
Grain boundaries
Texture

ABSTRACT

The microstructure, texture, hardness and magnetization have been investigated in a series of strongly cube-textured $(Ni_{95}W_5)_{100-x}Cu_x$ samples with $x=0$, 5, 10 and 15 at% Cu. It is found that the addition of 5 at% Cu to the Ni–5 at% W alloy results in a substantial decrease of the Curie temperature and in a reduction of the saturation magnetization without significant modification of the microstructure and the texture. This additionally alloyed material is only slightly softer than the Ni–5 at% W substrate. Although the Curie temperature and saturation magnetization decrease in the samples with higher concentrations of copper, increasing the Cu-content to 10 at% and 15 at% leads to increased frequencies of annealing twins in the cube-textured matrix. It is suggested that the $(Ni_{95}W_5)_{100-x}Cu_x$ alloy with $x=5$ at% Cu may be a good candidate material for using as a substrate for coated conductors.

1. Introduction

Ni-based alloys are widely used as substrates for coated conductors, i.e. the second generation of high-temperature superconducting tapes. To provide high critical current densities in the superconducting layer, the microstructure of a substrate should consist of grains with predominantly low-angle grain boundaries (LAGBs). In the so-called rolling assisted bi-axially textured substrate (RABiTS) process [1], such a microstructure is obtained by annealing of a heavily cold-rolled material, which results in the formation of a strong cube texture and thus in a high fraction of LAGBs. One of the commonly used substrate materials for the coated conductors is Ni–5 at% W. After appropriate processing, Ni–5 at% W substrates contain a very strong cube texture and have a sufficient level of strength [2]. However, due to a high Curie temperature (T_c=330–340 K [3,4]) this material imposes significant energy losses in the superconductor when utilized in alternating current (AC) applications at temperatures below 77 K [5].

Binary Cu–Ni alloys with lower T_c and Cu–Ni alloys with small additions of other metals have been considered as possible alternatives to the Ni–W system aiming at reducing AC losses [6–12]. However, large concentrations of copper in such materials are detrimental to the mechanical strength [10], which can complicate further reel-to-reel processing of annealed superconducting tapes. In the present work, the reduction of the Curie temperature of the substrate material is achieved by adding small amounts of copper to the Ni–5 at% W alloy. Several RABiTS-processed Ni–Cu–W samples with different concentrations of copper are investigated using the electron backscatter diffraction (EBSD) technique, hardness and magnetization measurements. Their microstructure, texture and properties are compared with those in the Ni–5 at% W substrate.

2. Experimental

Four alloys with nominal compositions defined as $(Ni_{95}W_5)_{100-x}Cu_x$, where $x=0$, 5, 10 and 15 (samples C0, C5, C10 and C15, respectively), were prepared by melting 99.99% pure metals. The ingots obtained were homogenized and hot-forged into $9\times15\times80$ mm^3 bars. The samples were cold-rolled using mirror-finished rolls with no lubrication, applying $<5\%$ thickness reduction per pass to a final thickness of 80 μm (a total reduction of 99%). The cold-rolled material was first annealed at 700 °C for 30 min, followed by subsequent heating to 1050 °C and annealing at this temperature for 2 h. The heat-treatments were conducted in a $N_2-5\%$ H_2 atmosphere.

The microstructure of the finally annealed samples was characterized in the rolling plane by the EBSD technique applying a step size of 1 μm. A coarser step size, 10 μm, was used for texture studies covering a total area of at least 4 mm^2 in each sample. Since conventional EBSD analysis cannot reliably detect very low misorientations, only misorientations $>1.5°$ were considered when calculating fractions of different grain boundary (GB) types.

* Corresponding author.
E-mail address: anwu@dtu.dk (A.C. Wulff).

0167-577X/$ - see front matter © 2012 Elsevier B.V. All rights reserved.
http://dx.doi.org/10.1016/j.matlet.2012.11.007

Vickers microhardness was measured using a load of 200 g with a 15 s dwell time.

The magnetization of the annealed substrates was investigated using a vibrating sample magnetometer in a cryogenic-free measurement system. The temperature dependence of the magnetic moment of the vibrating substrate (20.4 Hz) was measured in a constant magnetic field of $\mu_o H = 50$ mT applied perpendicular to the rolling plane of the substrate by ramping the temperature from 5 to 325 K at a rate of 2 K/min. The Curie temperature was determined from temperature-dependent measurements of the magnetic moment, as described in [4]. The saturation magnetization M_s values were recorded from magnetic hysteresis loops produced at 75 K by ramping the field at a rate of 0.5 T/min between [−1;1] T.

3. Results and discussion

Microstructure and texture: Microstructures of the annealed samples with different concentrations of Cu, where sample C0 corresponds to the Ni–5 at% W alloy, are shown in Fig. 1. In every sample, most grains are separated by LAGBs. In samples C0 and C5, where the area fraction of grains within 10° of the ideal cube orientation was ~99%, the fraction of boundary misorientations below 10° was 93%. Due to an increased frequency of annealing twins, a weaker cube texture and greater fractions of GB misorientations >10° were obtained in samples C10 and C15 (Figs. 2 and 3a). Such high angle boundaries are likely to cause dramatic reductions in the critical current density in the superconducting tape [13].

Comparing the EBSD maps from the different samples (Fig. 1), it is apparent that matrix grains are slightly coarser in sample C15. The grain size, calculated excluding twin boundaries, increases from 23 μm in sample C0 to 27 μm in sample C15. The change in the average spacing between all boundaries, d_{all}, is however less appreciable (see Fig. 2) due to the presence of many Σ3 boundaries in the microstructure of sample C15 (Fig. 1).

To analyze combined changes in the average grain size and the boundary population, we determined the total length of GB traces per unit area L_A [16] for boundaries with misorientations >10°. The $L_{A(\theta>10^\circ)}$ values calculated as described in [17] are plotted in Fig. 3b, where it is seen that a small increase in the copper content does not lead to an increased length of boundary traces between grains with strongly undesirable misorientations. In fact, the $L_{A(\theta>10^\circ)}$ value for sample C5 is even slightly smaller than that for sample C0 due to a greater d_{all} (Fig. 2). However, as the concentration of copper increases from 5 to 15 at%, $L_{A(\theta>10^\circ)}$ becomes significantly larger (see Fig. 3b). It is therefore evident that a microstructure most closely resembling the microstructure of the Ni–5 at% W substrate can be obtained if the maximum concentration of copper in the $(Ni_{95}W_5)_{100-x}Cu_x$ system is restricted to 5 at%.

Hardness and magnetic properties: The influence of the Cu-content on mechanical properties of the substrate was evaluated in this work using Vickers microhardness measurements. As expected, the addition of copper softened the Ni-based substrate. The difference in hardness between the samples was however small; with increasing copper content from 0 to 5 at%, the hardness decreased from 128 HV to 124 HV. It is significant that the minimum hardness of 122 HV recorded in sample C15 was still considerably greater than the hardness of annealed Ni–Cu, Ni–Cu–Co and Ni–Cu–W substrates containing ~50% Cu [11,12].

Compared to the hardness, magnetic properties were found to be much more sensitive to the Cu-content. As seen in Fig. 4, the addition of Cu strongly reduces both the saturation magnetization and the Curie temperature of the ferromagnetic Ni–5 at% W alloy. The M_s and T_c values for the alloys investigated in our experiments are also substantially smaller than the corresponding values reported in a previous work on $(Ni_{97}W_3)_{100-x}Cu_x$ substrates [18]. The low saturation magnetization values for the $(Ni_{95}W_5)_{100-x}Cu_x$ substrates analyzed in the present study suggest

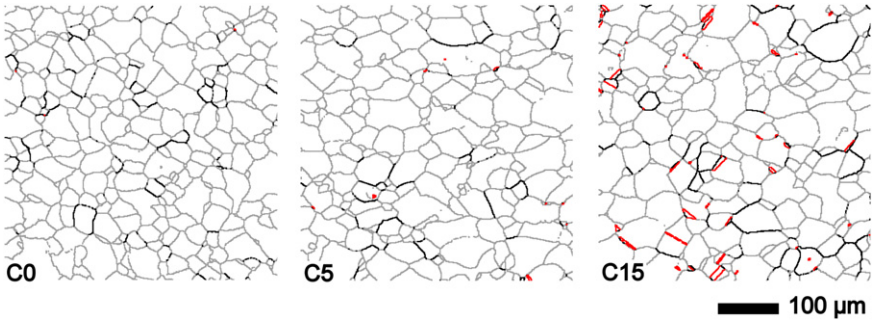

Fig. 1. EBSD maps showing the microstructure of the annealed samples C0, C5 and C15. The thin gray and bold black lines correspond to misorientations $\theta = 1.5$–10° and $\theta > 10°$, respectively. Σ3 boundaries with deviations <3° from the ideal twin misorientation [14,15] are shown as bold gray lines (red in the online version). (For interpretation of the references to color in this figure legend, the reader is referred to the web version of this article.)

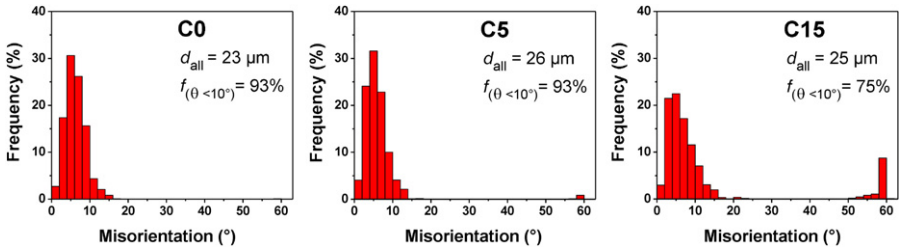

Fig. 2. Distributions of misorientation angles. The numbers indicate the average spacing between all boundary types (including twin boundaries), d_{all}, and fractions of boundary misorientations below 10°, $f_{(\theta<10^\circ)}$. Note an increased frequency of ~60° misorientations in sample C15 caused by a large number of annealing twins.

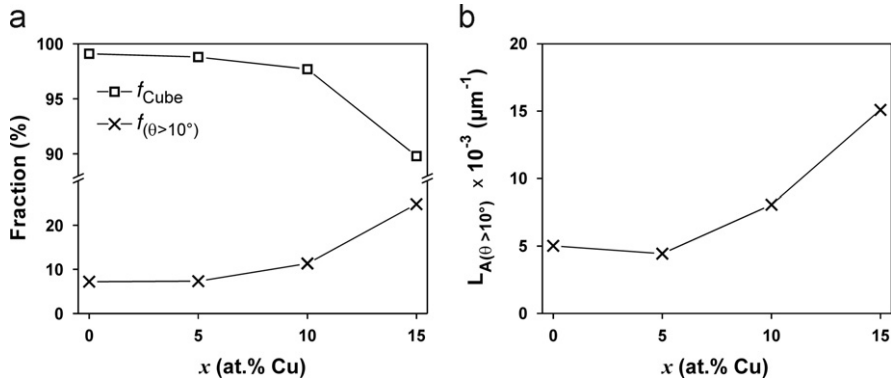

Fig. 3. Variation of parameters describing the microstructure and texture as a function of Cu-content in $(Ni_{95}W_5)_{100-x}Cu_x$ alloys: (a) fractions of the cube texture and boundary misorientations $>10^\circ$ (f_{Cube} and $f_{(\theta>10^\circ)}$, respectively); (b) total lengths of GB traces per unit area for boundaries with misorientations $>10^\circ$.

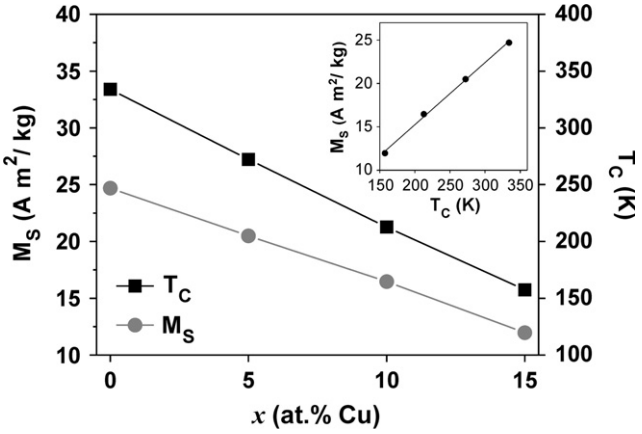

Fig. 4. Effect of the Cu-content on the saturation magnetization M_s and Curie temperature T_c for $(Ni_{95}W_5)_{100-x}Cu_x$ alloys. The inset shows that for the alloys studied T_c and M_s are linearly related.

that coated conductors produced using these substrates will benefit from reduced AC losses in the superconductor.

4. Summary

Strongly cube-textured Ni–Cu–W samples having different concentrations of copper (0, 5, 10 and 15 at%) have been investigated in the present work. It is found that the addition of 5 at% Cu to the Ni–5 at% W alloy substantially decreases the Curie temperature and saturation magnetization without significant modification of the microstructure and texture in the substrate material and with only a small decrease in hardness. Although the Curie temperature and the saturation magnetization decrease with increasing Cu-content, increased frequencies of annealing twins in the samples with 10 and 15 at% Cu may negatively affect superconducting properties of the coated conductor. Comparing the different samples studied in this work, the $(Ni_{95}W_5)_{100-x}Cu_x$ alloy with $x=5$ at% Cu appears to be the most appropriate candidate material for the use as a substrate for coated conductors.

Acknowledgments

This work was supported by the Danish Ministry of Science, Innovation and Higher Education under Contract no. 09-065234.

References

[1] Goyal A, Norton DP, Christen DK, Specht ED, Paranthaman M, Kroeger DM, et al. App Supercond 1996;4:403–27.
[2] Eickemeyer J, Selbmann D, Opitz R, Wendrock H, Maher E, Miller U, et al. Phys C 2002;372:814–7.
[3] Sarma VS, Eickemeyer J, Schultz L, Holzapfel B. Scripta Mater 2004;50:953–7.
[4] Ijaduola AO, Thompson JR, Goyal A, Thieme CLH, Marken K. Phys C 2004;403:163–71.
[5] Thompson JR, Goyal A, Christen DK, Kroeger DM. Phys C 2002;370:169–76.
[6] Shi K, Zhou Y, Meng J, Yang J, Hu GY, Gu HW, et al. Phys C 2003;386:353–7.
[7] Girard A, Bruzek CE, Jorda JL, Ortega L, Soubeyroux JL. J Phys: Conf Ser 2006;43:341–4.
[8] Rutter NA, Goyal A, Vallet CE, List FA, Lee DF, Heatherly L, et al. Supercond Sci Technol 2004;17:527–31.
[9] Zhou YX, Sun L, Chen X, Fang H, Putman PT, Salama K. Supercond Sci Technol 2005;18:107–11.
[10] Varanasi CV, Brunke L, Burke J, Maartense I, Padmaja N, Efstathiadis H, et al. Supercond Sci Technol 2006;19:896–901.
[11] Vannozzi A, Thalmaier G, Armenio AA, Augieri A, Galluzzi V, Mancini A, et al. Acta Mater 2010;58:910–8.
[12] Vannozzi A, Galluzzi V, Mancini A, Rufolini A, Augieri A, Armenio AA, et al. IEEE Trans Appl Supercond 2011;21:2908–11.
[13] Durrell JH, Rutter NA. Supercond Sci Technol 2009;22:1–18.
[14] Mishin OV. J Mater Sci 1998;33:5137–43.
[15] Mishin OV, Huang X. Mater Sci Forum 1999;294–296:401–4.
[16] Cao WQ, Godfrey A, Liu Q. Mater Sci Eng A 2003;361:9–14.
[17] Wulff AC, Mishin OV, Grivel J-C. J Alloys Compd 2012;539:161–7.
[18] Song KJ, Ko RK, Kim HS, Ha HS, Ha DW, Oh SS, et al. IEEE Trans Appl Supercond 2007;17:3432–5.